Alma Mater Studiorum – Università di Bologna

Scuola di Scienze

Dipartimento di Fisica e Astronomia

Corso di Laurea Magistrale in Astrofisica e Cosmologia

Gas rotation in massive galaxy clusters with axisymmetric potential: models and perspectives for X-ray observations

Tesi di Laurea Magistrale

Candidato:
Alberto Acuto

Relatore:
Chiar.mo Prof.

Carlo Nipoti

Co-relatore:
Dott. Stefano Ettori

Sessione I

Anno accademico 2016/2017

A mio Nonno
e alla mia famiglia.

Contents

List of Figures

List of Tables

Abstract

Il principale obiettivo di questa Tesi è lo studio del moto dell'intracluster medium (ICM) in rotazione in ammassi di galassie e fare dei test osservativi per la futura generazione di telescopi ad alte energie, come il progetto `ATHENA` (che sarà operativo dal 2028). Nel lavoro realizzato da Bianconi et al. (2013) studiarono la rotazione del gas in ammassi con un potenziale sferico di Navarro, Frenk e White utilizzando semplici profili di velocità, valutando i principali effetti della rotazione sull'ellitticità delle isofote X; nella seconda parte il lavoro si focalizzò nello studio di spettri simulati utilizzando le specifiche tecniche del calorimetro a bordo del satellite Giapponese Astro-H.
Utilizzando il metodo presentato nel lavoro di Ciotti and Bertin (2005) abbiamo espanso il potenziale gravitazionale in forma ellissoidale. Quindi abbiamo assunto uno schiacciamento del potenziale di ~ 0.4 corrispondente ad una distribuzione di densità sempre positiva. Abbiamo ricreato potenziali oblati e prolati per verificare come le diverse geometrie avessero effetti sulle quantità osservabili dell'ICM. In particolare abbiamo considerato aloni di dark matter assialsimmetrici con una distribuzione di NFW e con un rapporto assiale di ~ 0.6 e abbiamo confrontato l'evidenza osservativa dello schiacciamento delle isofote con le misure ottenute da Lau et al. (2012) con osservazioni su un campione di ammassi con i satelliti CHANDRA e ROSAT. Abbiamo misurato uno schiacciamento medio di circa 0.13 per quanto riguarda i modelli non rotanti e di circa 0.16 per quanto concerne i modelli rotanti, sia nel caso oblato che prolato. Questi risultati sono anche in accordo con quanto trovato da Vikhlinin et al. (2009), dove misurarono una ellitticità media di ~ 0.18.
L'ultima parte del lavoro presenta uno studio degli spettri simulati in banda X a diversi raggi dal centro degli ammassi dopo che si è convoluta la brillanza superficiale dell'ammasso con la risposta strumentale dello spettrometro ad alta risoluzione (X-IFU - X-ray Integral Field Unit) che sarà a bordo di ATHENA per misurare il moto coerente del gas. Abbiamo misurato uno spostamento Doppler della riga del ferro a 6.7 keV dell'ordine di ~ 5 eV, che corrisponde ad una velocità di circa 1000 km/s, per i modelli oblati. Nei modelli prolati invece abbiamo trovato uno spostamento del centroide di circa ~ 15 eV, consistente con una velocità di rotazione di oltre 2400 km/s. Dopo aver valutato lo spostamento della riga dovuto al moto abbiamo analizzato l'allargamento della suddetta riga dovuto alla dispersione di velocità lungo la linea di vista. Abbiamo quindi trovato che nelle regioni più interne si raggiunge un allargamento dell'ordine di 1000 km/s per i modelli prolati mentre per i modelli oblati si raggiunge circa 300 km/s.

Abstract

The main scope of this Thesis is to study models of rotating intracluster medium (hereafter ICM) in galaxy clusters and to make observational test for the next generation X-ray telescopes, like ATHENA (scheduled to be launched in 2028). Bianconi et al. (2013) studied the gas rotation in clusters with spherical Navarro, Frenk, White gravitational potential using simple velocity profiles and evaluating the effect of rotation on the ellipticity of X-ray isophotes; the second part of that work was based on the study of simulated X-ray spectra using the specifics of the calorimeter on board of the Japanese Satellite Astro-H.
Using the method provided by Ciotti and Bertin (2005) we expanded the potential in an ellipsoidal form. Thus, the adopted flattened gravitational potential corresponds to everywhere-positive density distribution with a maximum flattening of ~ 0.4. We created both oblate and prolate gravitational potential in order to explore how different geometries influence the observational properties of the ICM. In particular, we considered axisymmetric NFW halos with axial ratio of ~ 0.6 and we compared the observational quantity, like the isophotal ellipticity, with the measurements from the paper Lau et al. (2012) made with CHANDRA and ROSAT for a sample of clusters. We measured a mean ellipticity of about ~ 0.13 for the non-rotanting models and a ~ 0.16 for the rotating models, both oblate and prolate. This result is comparable with what was found in Vikhlinin et al. (2009) where they found a mean ellipticity of ~ 0.18.

The last part of the work presents the analysis of simulated X-ray spectra at different distances from the center of massive clusters after convolving the surface brightness with the instrument response of the calorimeter spectrometer (X-IFU - X-ray Integral Field Unit) on board of ATHENA to measure the ICM bulk motion.
We measured a Doppler shift of the iron line at 6.7 keV in the order of ~ 5 eV that corresponds to a velocity peak of the profile below the 1000 km/s for the oblate models. In the prolate models we found a centroid shift of ~ 15 eV, consistent with velocity rotation higher than 2400 km/s. After the evaluation of the centroid shift of the 6.7 keV line we studied the broadening of the line due to dispersion velocity in the line of sight. In the innermost regions of the prolate models we measured a broadening of ~ 1000 km/s while for the oblate models about 300 km/s.

Chapter 1

Introduction

In this Thesis we will present a study of gas rotation in galaxy clusters and the study of spectroscopic features in X-ray emission through high resolution instruments on ATHENA[1], the next big European project in the field of X-ray observatory satellite.

The gas is in equilibrium with flattened axisymmetric dark matter potential obtained from the Navarro, Frenk, White profile, hereafter NFW, and the effect of the rotation contributes in the flattening of the isophotes. The flattening of the isophotes is one the most interesting terms of comparison for the goodness of our models with observational data from the papers of Lau et al. (2012) and Fang et al. (2009).

The last section of the work aimed to measure gas velocity from mock observations using X-IFU (X-ray Integral Field Unit) proposed for ATHENA.

We explored both the line centroid shift due to the gas motion and the line broadening due to the dispersion of velocity in the line of sight to verify the power of reconstructing the velocity profile of the gas thanks to high resolution spectroscopy.

1.1 Scientific Purpose

Dark matter halos are not spherical but tend to be triaxial and elongated in the direction of the collapse flow (e.g. Kazantzidis et al. 2004, Bryan et al. 2013, Despali et al. 2017). We decided to create a flattened dark matter potential starting from a spherical NFW potential in order to model the gas rotation and verify photometric and spectroscopic features in X-rays.

The mass estimated under the assumption of hydrostatic equilibrium tends to differ from gravitational weak lensing measurement, this effect is known as hydrostatic bias (see section (1.5) for further details). This gap between these two measurements may be reduced adding the term of bulk motion of gas in the equilibrium because the rotation changes the effect of the gravitational potential on the gas distribution (e.g. Bianconi et al. 2013, Rasia et al. 2014, Nipoti et al. 2015).

---

[1] ESA for futher information and see chapter 5 for the technical specifics.

One of the efforts needed before the start of a big mission is to foresee the improvements that this particular instrument, such as ATHENA, could give to the scientific community. Testing the possibilities of what ATHENA can achieve in the next decades of work is basically the theoretical starting point of what we could expect from observations when this satellite will be operative.
The high resolution spectrometers will allow us to achieve direct detection of the motion of the intracluster medium, hereafter ICM, with great accuracy. In fact, X–ray high–precision spectroscopy potentially offers one of the most promising ways to directly measure such gas motions, detectable from the detailed study of the shape and centroid of resolved spectral emission lines (Biffi et al. 2013a). The expectations for heavy–ion emission lines in the X–ray spectra diagnostics are related in particular to the most prominent emission line in X–ray spectra, namely the 6.7 keV line from helium–like iron. In fact, the large atomic mass of the FeXXV ion significantly reduces the thermal line broadening and the line width turns out to be definitely more sensitive to turbulent gas motions (e.g. Inogamov and Sunyaev 2003).

1.2 Cosmological background and formation of structures

We present a brief overview of the cosmological background that is involved in this work. Under the assumption of a large-scale homogeneous and isotropic[2] Universe we can describe the space-time with the *Robertson - Walker Metric*[3] that is a general formulation of the geometry of the space-time obtained from the main equations of the General Relativity[4] :

$$ds^2 = (cdt)^2 - a(t)^2 \left[\frac{dr^2}{1 - Kr^2} + r^2 (d\theta^2 + sin^2\theta d\varphi^2) \right], \tag{1.1}$$

where ds^2 is the distance in the space-time. They used polar coordinates r, θ and φ, t the proper time, $a(t)$ is the function that describes the evolution of the Universe (called *scale factor* or *expansion parameter*) and it is correlated with the redshift ($1 + z = a_0/a(t)$). K is the *curvature parameter* that is constant and it could assume the values -1, 0 and 1 respectively closed, flat and open Universe (Coles and Lucchin 2002).

From this point using the equation (1.1) to resolve the Einstein equations[5] we can obtain the functional form for $a(t)$:

$$\ddot{a} = -\frac{4}{3}\pi G \left(\rho + 3\frac{P}{c^2} \right) a, \tag{1.3}$$

---

[2] The assumption of an homogeneous and isotropic Universe beyond the large scale sctructure of the galaxies is called Cosmological Principle.

[3] Some authors refer to a Friedmann - Lemaître - Robertson - Walker Metric.

[4] All the sign convention are taken from Coles and Lucchin.

[5] The Einstein equation is the field equation of General Relativity:

$$G_{\mu\nu} = R_{\mu\nu} - \frac{1}{2} g_{\mu\nu} R - \Lambda g_{\mu\nu} = \frac{8\pi G}{c^4} T_{\mu\nu}, \tag{1.2}$$

where $G_{\mu\nu}$ is the *Einstein Tensor*, $R_{\mu\nu}$ is the *Ricci Tensor*, R is the trace of $R_{\mu\nu}$ called *Ricci Scalar*, Λ is the *Cosmological Constant*, $g_{\mu\nu}$ is the metric tensor and $T_{\mu\nu}$ is the stress-tensor.

and

$$\dot{a}^2 + Kc^2 = -\frac{8}{3}\pi G \rho a^2, \tag{1.4}$$

these equations (1.3), (1.4) are known as *Friedmann Cosmological equations* and from equation (1.4) we can derive the curvature parameter K:

$$\frac{K}{a^2} = \frac{1}{c^2}\left(\frac{\dot{a}}{a}\right)^2 \left(\frac{\rho(z)}{\rho_{crit}(z)} - 1\right), \tag{1.5}$$

where:

$$\rho_{crit}(z) = \frac{3}{8\pi G}\left(\frac{\dot{a}}{a}\right)^2, \tag{1.6}$$

that is the density of the universe. The *density parameter*, as it is known Ω, is the main parameter that defines the geometry of the Universe and it is defined as:

$$\Omega(z) = \frac{\rho(z)}{\rho_{crit}(z)}. \tag{1.7}$$

We live in a "flat universe" $\Omega = 1.00 \pm 0.02$ (Planck Collaboration et al. 2016) that is obtained by adding the three main components of the universe: dark matter and baryons under the name of mass component, relativistic component (also called radiation) and cosmological constant Λ:

$$\Omega = \Omega_m + \Omega_{Rad} + \Omega_\Lambda = 0.315^{+0.018}_{-0.018} + 9.24 \times 10^{-5} + 0.6817^{+0.0018}_{-0.0018} = 1.00^{+0.02}_{-0.02}. \tag{1.8}$$

The most reliable cosmological paradigm is the ΛCDM cosmology where Λ is related to the cosmological constant, that is dominant, and CDM is for Cold Dark Matter. We know that the largest virialized structures are the youngest, in the sense that they were assembled recently. In fact galaxy clusters are the youngest components of the Universe in a hierarchical paradigm where the assembly of mass start to gather together from little halos to form the biggest. This is known as bottom-up or hierarchical model of formation.

Before going in details in the formation of clusters we explore the formation of the first fluctuations that are the triggers of the collapse for the formation of objects like galaxies and clusters. The technique of the clustering[6] is a wide-used method to study the spatial correlation between the initial fluctuations because they trace the objects distribution in the cosmic web[7] in the redshift space. Analyzing the redshift distribution one can reconstruct the motion of the initial fluctuations and reconstruct how was the Universe after the inflationary epoch.

Galaxy clusters are particularly interesting topic in astrophysics and cosmology because in spite of the numerous mergers that experienced in the formation, sufficiently relaxed clusters (that can be considered clusters that do not have experienced a recent major merger) can be considered systems close to

---

[6] The clustering is a statistical method used to study the correlation between the same type of objects.

[7] The cosmic web is the spatial distribution of the structures of the Universe: galaxies, clusters and super-clusters are distribuited not uniformly in the space but they tend to be concentrated in big structures (known as nodes) and in big voids through them and they are connected by filaments made of dark-matter and baryonic matter like diffuse gas and "field" galaxies.

equilibrium. Clusters close to equilibrium and without evident signs of dynamical phenomena can be studied under the assumption of the conservation of the total mass.

1.2.1 Structure Formation

The conventional paradigm for the formation of structures in the Universe is based on the growth of small perturbations due to gravitational instabilities. In the currently standard hierarchical structure formation scenario, objects are thought to form via gravitational collapse of peaks in the initial primordial density field characterized by the density contrast:

$$\delta(t, \mathbf{x}) = \frac{\rho(t, \mathbf{x}) - \rho_{bk}(t)}{\rho_{bk}(t)}, \tag{1.9}$$

where ρ_{bk} is the mean mass density of the Universe and $\mathbf{x}$ is a position in the space.
For simplicty we assume that the $\delta(t, \mathbf{x})$ is a homogeneous and isotropic Gaussian random fluctuation, more about the characterization and the way are studied the initial overdensities can be found in Guth and Pi 1982, Peebles 1982, Bardeen et al. 1983 and Padmanabhan 2003. The initial fluctuations are distributed like a power-law:

$$P_{in}(t, k) =< |\delta_k(t)|^2 >= Ak^s \tag{1.10}$$

where δ_k is the Fourier transform of $\delta(t, \mathbf{x})$ and it is mediated in the ensemble. k is Fourier transform of the characteristic scale of the perturbations, A is the normalization of the spectrum and s is the spectral index of the power-law.
When $\delta \ll 1$ the gravitational collapse is in a linear regime, but observations tell us that many objects in the Universe are in a non-linear regime (for instance galaxy clusters). The collapse of the dark matter halos can be described using the Press-Schecter formalism (Press and Schechter 1974) that predicts a number of objects in a certain mass range.
Sufficiently high overdensity are able to collapse. The collapse is studied under the assumption of spherical symmetry with spherically-symmetric density fluctuation of initial radius R_i, that is the radius of the perturbation in a ρ_{bk} mean density field. The growth of such perturbation stops at a maximum value R_{ta}, the radius of the *turn around* at a certain epoch and then $R(t)$ starts decreasing until the perturbation collapses. The ratio between the density at the end of the collapse, ρ_{coll}, with the mean density ρ_{bk} is $\Delta_{vir} = \rho_{coll}/\rho_{bk} \approx 200$. In an overdense region we are in a non-linear regime and the perturbations can not be studied in the linear assumption. The evolution of a perturbation in a overdense region under the assumption of a spherical approximation is shown in figure (1.1) where a_{nl} is the moment of the beginning of the non-linear regime of the collapse, a_{max} is the moment of the turn around when the perturbed region detaches from the expansion flow and a_{coll} when there is the formed collapsed region. Simple analytical models, such as the spherical collapse model, can not make predictions about the internal structure of the dark matter halos which instead has been widely studied in cosmological N-body simulations. In the next section we will briefly describe the structural properties of dark matter halos.

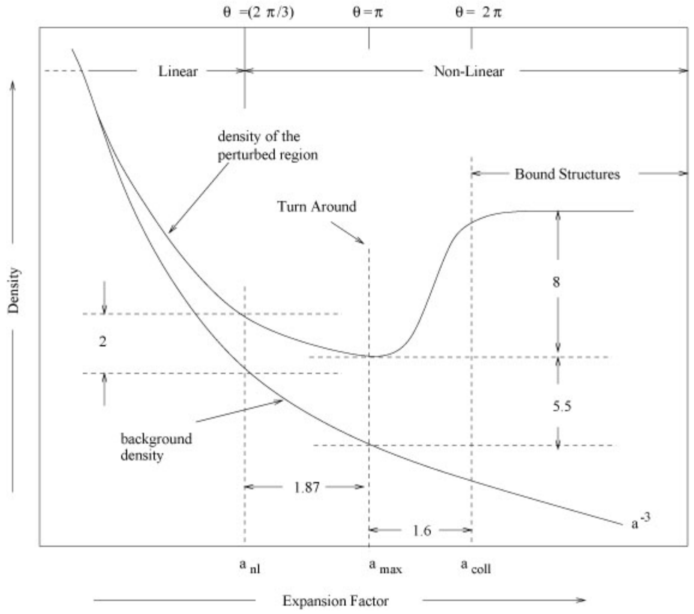

Figure 1.1: Evolution of a perturbation in an overdense region in a spherical approximation. It is evident the moment of the turn around, when the perturbed region differs from the Hubble flow (a^{-3}) and starts to gain matter creating a collapsed region (Padmanabhan 2003).

1.2.2 Dark-Matter profiles and halo shapes

In the cold dark matter scenario we know that collisionless particles of dark matter in the early phases of the universe gathered in halos of small mass. The theory of the hierarchical formation claims that the small halos experienced many mergers creating bigger halos where the baryons, after decoupling with the radiation, are free to collapse in dense structures creating the first stars[8] and the first galaxies. Galaxy clusters are the latest bound structures created and they have experienced many mergers and many are still undergoing.

The first astronomer that proposed and tested the presence of a bigger amount of mass was Fritz Zwicky (1937) in the work "On The masses of nebulae and of cluster of nebulae", where the mass estimated from observations of galaxy clusters (especially the data from the Coma cluster) were much higher, about an order of magnitude, than what was predicted before using only luminous matter.

Starting from this evidence in the following years there were strong proofs supporting this theory (e.g. Smith 1936, Babcock 1939, Oort 1940) for instance the rotation curve of galaxies (that was expecting a rotation decreasing on the radius increasing, as expected from Kepler's law, but it keeps on constant).

The dark matter halos that were formed in simulations are not well represented

---

[8] The first stars are called "third" population stars composed only by hydrogen and helium, no extra metals.

as isothermal sphere (Burkert 1995):

$$\rho(r) \propto \frac{1}{r^2}, \tag{1.11}$$

but have gently changing logarithmic slopes like:

$$\rho(r) = \frac{\rho_{ref,z}}{\frac{r}{r_s}(1+\frac{r}{r_s})^2}, \tag{1.12}$$

which is known as the NFW density profile. This profile is one of the most used for its simplicity and thanks to its ability in reproducing a wide range of masses.

So far we have focused on the angle-averaged density profiles of halos. Another interesting property of halos is their shape, that is whether are close to spherical, axisymmetric or triaxial (e.g. Buote and Tsai 1995, Jing and Suto 2000, Kazantzidis et al. 2004, Lee et al. 2008, Schneider et al. 2012, Bryan et al. 2013). The fact that dark matter halos are not spherical lead us to use a flattened potential for our models.

1.3 Properties of galaxy clusters

Galaxy clusters can be studied in many observational windows from optical, where can be studied the peculiarities of the galaxies inside the cluster and gravitational effects from lensing, in the radio band, where non-thermal emission can be studied, and X-ray astronomy where the hot gas emission can be analyzed. X-ray emission of the ICM is a tracer for dark matter distribution because studying the isophotes, that are regions with the same surface brightness, we can reconstruct the gas and dark matter distribution.

Typical cluster masses are about $10^{13\sim15} M_\odot$, smaller structures with lower mass are typically called *groups*. Recently bigger structures are found, they are called super-clusters and the first identified is the *Laniakea*, where the Milky Way, our galaxy, resides. However these super-clusters are not virialized (Tully et al. 2014).

The *richness* is a measure of the number of galaxies that are associated with the cluster and it derives from the catalogation of Abell et al. (1989); cluster can be classified based on the presence of spiral galaxies, in fact, clusters can be *spiral rich* or *spiral poor* if there is a massive presence of that type of galaxy or there is the dominance of elliptical galaxies. If there is a bigger central galaxy a cluster can be defined as *cD Cluster*, where they refer to that galaxy as Central dominant or core dominant.

Dark matter is the main component of clusters (approximately 80%), the second main component is diffuse gas ($\sim 13\%$) while stars are about the $\sim 7\%$ of the total mass (Bykov et al. 2015).

Typical dimensions of the virial radius of a cluster are about $1 \sim 2$ Mpc, the virial radius is defined in section (2.1).

The ICM mean density, under the assumption of a gas fraction $f_{gas} = 0.13$ is

$$< \rho_{ICM} > \equiv \frac{f_{gas} M_{tot}}{r_{vir}^3} \sim 10^{-27} g/cm^3. \tag{1.13}$$

Assuming a fully ionized gas with $\mu = 0.59$, mean molecular weight, mean temperature of $\sim 10^7 K$, virial radius of 2 Mpc and a total mass of $10^{15} M_\odot$ so equation (1.13) corresponds to a number density $< n_{ICM} >\sim 10^{-3\sim-5}\ cm^{-3}$. The ICM has a high temperature and it is observable in X-ray, in fact we can measure the X-ray luminosity:

$$L_x = \epsilon \times Volume = n_i n_e \Lambda(T, Z) \times \frac{4\pi}{3} r^3_{vir}, \tag{1.14}$$

where ϵ is the emissivity of the gas and depends on the n_i the number density of ions, n_e the electrons number density and on Λ that is the cooling function (see equation 2.58). Z is the metallicity of the gas, galaxy clusters present a mean metallicity of $1/3$ the solar abundance. So we assume in our models $Z = 0.3 Z_\odot$.
In table (1.1) we summarize the main characteristics of the clusters and groups.

Cluster	Mass	L_X	r_{vir}	n_e	n_i	T	f_{gas}
	$[M_\odot]$	[erg/s]	[Mpc]	$[cm^{-3}]$	$[cm^{-3}]$	[keV]	
Massive	10^{15}	10^{44}	$1-2$	10^{-3}	10^{-3}	~ 7.5	0.13
Poor Groups	10^{13}	10^{42}	$0.1-1$	10^{-3}	10^{-3}	≤ 2	0.10

Table 1.1: Main physical parameters of galaxy clusters and groups (from Bahcall 1996).

1.3.1 Galaxy Clusters X-ray classification: Cool Cores and Non-Cool Cores

It is known that there is a bimodality in the X-ray emission from the intracluster medium that characterizes galaxy clusters between Cool Core and Non-Cool Core. This difference is connected with the temperature profiles: cool cores show a sudden drop toward the center while the second type has not a drop in the center. The cooling time[9]of the cluster center in non-cool core clusters, due to the low density in the core, is an order of magnitude higher than the Hubble time [10] (e.g. Fabian and Nulsen 1977, Cowie and Binney 1977, Hudson et al. 2010). The trend of the cooling time on radius is presented in figure (1.2), we can see that the innermost regions had the lower cooling time and it is associated with the high density in the core of this type of clusters.

Henning et al. (2009) show the different behaviour of surface brightness and temperature in cool core and non-cool core simulated clusters (figure 1.3). As

---

[9] The radiative cooling time is the time necessary for the gas to emit photons and get a lower energy, so a lower temperature,

$$t_{cool} = \frac{3nk_BT}{2n_in_e\Lambda(T,Z)}, \tag{1.15}$$

where Λ is the cooling function, $n = n_i + n_e$ where n_i is the ions density and n_e is the electrons density and k_B is the Boltzmann's constant.

[10] The Hubble time is defined as:

$$\tau_H = 1/H_0; \tag{1.16}$$

where H_0 is the Hubble constant. This is the time between the Big Bang and approximately the age of the universe (Coles and Lucchin 2002).

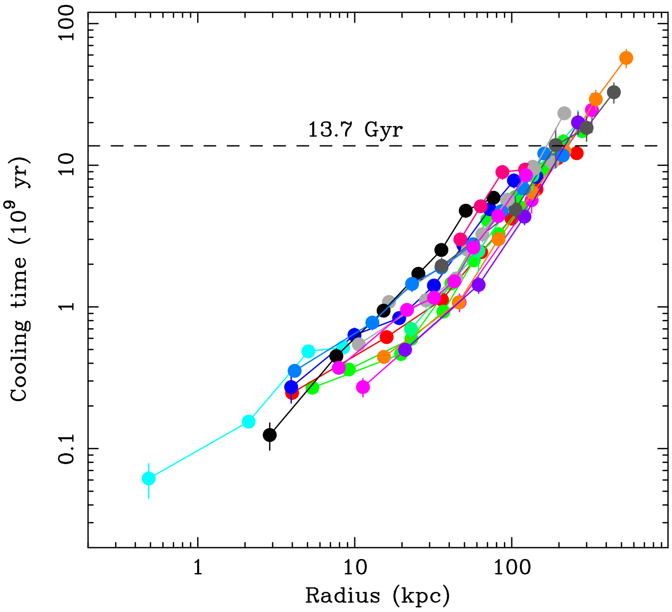

Figure 1.2: Cooling time of clusters in base of radius, the Hubble time is highlighted with a line at 13.7 Gyr (Peterson and Fabian 2006).

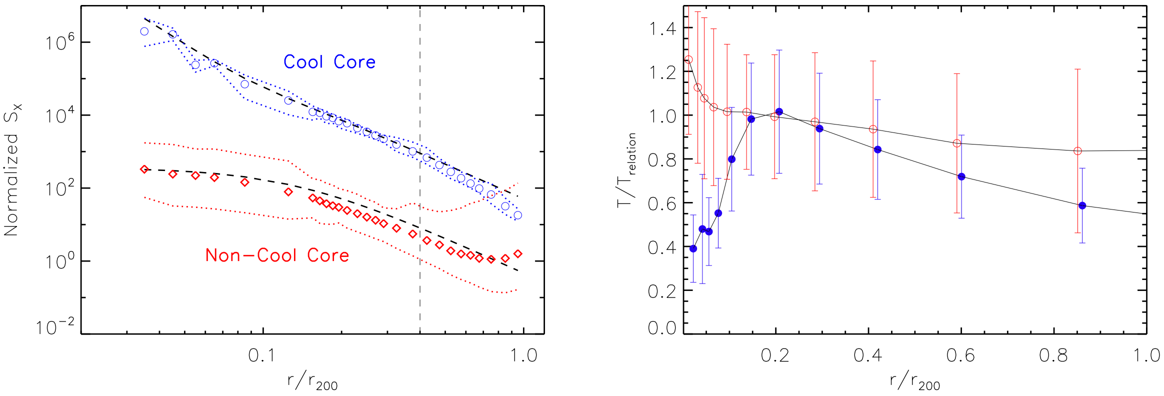

Figure 1.3: Averaged surface brightness for cool core and non cool core (left) and averaged temperature profile for cool core (blue) and non cool core (red) (right) of simulated clusters from Henning et al. (2009). The temperature profiles are normalized by the $M - T$ relation temperature and the errorbars are the 1 σ standard deviation from the radial point. The averaged surface brightness profiles for simulated galaxy clusters cool core (10) are the blue dots and red are for the non cool core (78). The non cool core sample are lowered in a factor of 10 for a better understanding.

already said, in the inner region of the cool core clusters there is a major amount of gas and, in fact, the surface brightness is higher than in the non-cool core case so the temperature profile is lower in the innermost part of these type because higher density tends to cool faster.

1.4 Cluster mass estimating methods

The total mass of a cluster is one the most important quantity to obtain in the study of this type of objects. In this paragraph, we present the most used methods to measure the mass in different windows of observation, from optical band to X-rays.
We start with the X-ray emission where, assuming hydrostatic equilibrium and spherical symmetry, we can obtain a measure of the mass:

$$M(<r) = -\frac{k_B T_{gas}(r)}{G\mu m_p}\left[\frac{d\log\rho_{gas}(r)}{d\log r} + \frac{d\log T_{gas}(r)}{d\log r}\right], \tag{1.17}$$

where $T_{gas}(r)$ and $\rho_{gas}(r)$ are the temperature and density profiles, k_B is the *Boltzmann's constant*, μm_p is the mean molecular weight of the gas. The density and temperature profiles can be obtained from observations (Böhringer and Werner 2010, Biffi et al. 2013b, Amodeo et al. 2017).
The *virial theorem* may be used to measure the mass of the cluster using the velocity dispersion of the galaxies in the cluster. Starting from the Virial theorem:

$$2T + U = 0, \tag{1.18}$$

where T is the kinetic energy and U is the potential energy. Substituting in the equation (1.18) the value of kinetic energy and potential energy assuming for simplicity that the cluster mass distribution is a uniform sphere of radius r_{vir}

$$M_{cluster}\,\sigma_v^2 - \frac{3}{5}\frac{GM_{cluster}^2}{r_{vir}} = 0, \tag{1.19}$$

we obtain:

$$M_{cluster} \approx \frac{5}{3}\frac{r_{vir}\sigma_v^2}{G}, \tag{1.20}$$

where $M_{cluster}$ is the total mass inside r_{vir}, G is the gravitational constant and σ_v is the velocity dispersion of the galaxy inside the cluster and it is typically about $\sim$ 1000 km/s (Sadat 1997 and Saro et al. 2013).
Obviously, this method takes many strong assumptions and some biases may affect the value of the mass measured. For instance, a strong assumption is considering that a cluster is not in dynamical interaction. Another bias that affects the measurement is related to σ_v of the galaxies because the velocity dispersion is a composite effect of the coherent motion of the galaxy in the cluster and the proper inner motion and it is not simple to distinguish the contributes (e.g. Sadat 1997, Saro et al. 2013). Another useful method to obtain the global mass is using the kinematic of galaxies, under spherical assumption and in the isotropic case where $\sigma_r = \sigma_\theta$:

$$M(r) = -\frac{r^2}{Gn_{gal}}\frac{dn_{gal}\sigma_r^2}{dr}. \tag{1.21}$$

The equation (1.21) is obtained from stellar hydrodynamics equations and it uses the number of galaxies (n_{gal}) and the dispersion velocity in the radial direction σ_r. This method suffers from the poor knowledge of the orbits of galaxies in clusters (Sadat 1997).
Concluding this excursus on methods for evaluating the total mass of the cluster we must cite *gravitational lensing*: strong lensing for the inner region of the cluster and weak lensing for the outskirts. Thanks to this method we can obtain a measure of the total mass of the cluster. The lensing mass evaluation can be described as:

$$M(\theta_t) = \pi D_l^2 r_t^2 \Sigma_{crit} \approx 4.4 \times 10^{14} M_\odot \left(\frac{r_t}{[30\, arcsec]} \right)^2 \left(\frac{D_l D_s}{D_{ls}\, [Gpc]} \right), \quad (1.22)$$

under the assumption of strong lensing and this is the cluster mass enclosed by a tangential critical curve[11] at radius r_t or the correspondent angular value θ_t (Hoekstra et al. 2013).
Here D_s, D_l, and D_{ls} are the angular diameter distances between the observer and the source, observer and the lens and lens and the source. Hence, the lensing signal depends on the redshifts of both the lenses and the sources. Multiplying with $\pi\Sigma_{crit}D_l^2$ converts the adimensional mass inside r_t to the projected mass inside of the physical radius $D_l r_t$. The value of Σ_{crit} strongly depends on the relative distances of observer and source, lens and observer and their relative distance:

$$\Sigma_{crit} = \frac{c^2}{4\pi G} \frac{D_s}{D_l D_{ls}}. \quad (1.24)$$

In weak lensing measurement we obtain the values of $k(\theta; M_\Delta, c_\Delta)$ (convergence profile) and $\gamma(\theta; M_\Delta, c_\Delta)$ (shear profile) that are needed to determine the tangential distortion profile defined as:

$$g_+(\theta) = \frac{\gamma(\theta)}{1 - k(\theta)}, \quad (1.25)$$

under the assumption of a spherical lens. The mass distribution is supposed spherical and comparing k and γ we can obtain a measurement of the inner mass (Okabe et al. 2010, Umetsu et al. 2011, Okabe and Smith 2016).
The Sunyaev-Zeldovich effect[12] can also be used to constrain the mass in the cluster.
The equation (1.28) shows the relation between the integrated comptonization

---

[11] The critical curves in gravitational lensing are lines where a source have an "ideal" infinite amplification. That are the eigenvalues of the Jacobian matrix A that defines the mapping of the lens:

$$A = \delta_{ij} - \frac{\partial^2 \Psi}{\partial x_i \partial x_j} = (1-k) \begin{bmatrix} 1-g_1 & -g_2 \\ g_2 & 1+g_1 \end{bmatrix} \quad (1.23)$$

where Ψ is the deflection potential, $g_i = \gamma_i/(1-k)$ is the reduced shear (γ, connected with the deflection potential) and k is the converge. For more details see Hoekstra et al. (2013).

[12] The Sunyaev-Zeldovich is a scattering phenomenon where the CMB photons (cosmic microwave background) scatter with the high temperature free electrons of the astrophysical plasma in clusters and lead a distortion of the millimeter emission peak of the CMB due to Inverse Compton.

parameter Y_X[13] that can be used as a proxy for total mass.

$$\frac{M_X^{500}}{10^{14}M_\odot h^{-1}} = \left(A_X h^{3/2}\right)\left(\frac{Y_X}{3\times10^{14}M_\odot\, keV}\right)^{B_X} E(z)^{C_X}; \tag{1.28}$$

where multiplying for an h will give the value of the cluster mass in units of $M_\odot\, h$ (Vikhlinin et al. 2009). M_X^{500} is the total mass obtained from X-ray measurement at r_{500}, the value of the normalization A_X in the best fit from Vikhlinin et al. (2009) is 5.77 ± 0.2, the slope B_X best fit is about 0.57 ± 0.03. The parameter $E(z) = H(z)/H_0$ is derived from the cosmology (see section 1.2 for the definition and the defition of $H(z)$, equation 2.3) and C_X is the term of redshift evolution (mean value -0.40 ± 0.20). The Y_x is the comptonization parameter (e.g. Saliwanchik et al. 2015, Grainge et al. 2015).

Also X-ray scaling relations can be used to determine the mass using observables like temperature, luminosity and velocity dispersion (e.g. Zhang et al. 2011, Giodini et al. 2013). The scaling relations can be obtained using the assumption of equilibrium, via virial theorem, and:

$$M_{\Delta_z} = \frac{4\pi}{3}\Delta_z \rho_{crit,0} E_z^2 R_{\Delta_z}^3. \tag{1.29}$$

Chosen a value for Δ we can obtain

$$T_{gas} \propto \frac{GM}{R} \propto R_{vir}^2, \tag{1.30}$$

substituting the equation (1.30) in equation (1.29) we obtain:

$$M_{\Delta_z} \propto T_{gas}^{3/2}. \tag{1.31}$$

(Stanek et al. 2006). The X-ray bolometric luminosity, L_X, can be related the total mass:

$$L_X \propto \epsilon R_{\Delta_z}^3 \propto T_{gas}^{1/2}\rho_{gas}^2 R_{\Delta_z}^3 \propto T_{gas}^{1/2} f_{gas}^2 M_{tot} \sim f_{gas}^2 T_{gas}^2, \tag{1.32}$$

assuming gas fraction constant we get that:

$$L_X \propto T_{gas}^2 \propto M_{tot}^{4/3}. \tag{1.33}$$

1.5 Hydrostatic mass bias

The mass determination that we analyzed in section (1.4), especially using X-ray and Sunyaev-Zel'dovich data, are combined under the assumptions of hydrostatic equilibrium in gravitational potential with spherical symmetry.

---

[13] The SZ effect of a cluster in a solid angle:

$$Y_c = \int y_c d\Omega = D_A^{-2}(z)\int y_c dA = \frac{\sigma_T}{mc^2}D_A^{-2}\int_V P_e dV; \tag{1.26}$$

where D_A is angular diameter distance, $d\Omega$ is the projected area in the sky, σ_T is the Thomson cross section, $dV = dldA$ is the volume and the P_e is the pressure profile. The other parameter in that equation is y_c that is the comptonization parameter of the thermal Sunyaev-Zeldovich:

$$y_c = \frac{k_B\sigma_T}{m_e c^2}\int_l T_X n_e dl. \tag{1.27}$$

(De Martino and Atrio-Barandela 2016)

Generally is found that mass estimated with weak lensing method, that characterize the all cluster's mass on the line of sight is about $9 \sim 10$ % higher than what is estimated in X-rays under the assumption of hydrostatic equilibrium (Zhang et al. 2010). To obtain these mass measurements many works adopted some approximations that bias low the value of about $5 \sim 10$ % with a scatter of $10 \sim 25$ % (Meneghetti et al. 2010, Rasia et al. 2012).
Some approximations come from the deprojection of the weak lensing mass due to the triaxiality of the potential and the possible presence of substructures (Sereno and Ettori 2015). Regarding the assumptions and approximations of the hydrostatic equilibrium of the X-ray mass measurements these are correlated to the presence of temperature inhomogeneities, presence of clumps of matter in the outskirts and mainly from non-thermal terms of pressure. The bias is estimated to be of the order of $25 \sim 35$ % (Piffaretti and Valdarnini 2008). Many authors proposed and tested the difference between the observational results and measurements of simulations with non-thermal components from AGN feedback, gas sloshing, contribution of turbulence and bulk motion of the gas (e.g. Vazza et al. 2012, Biffi et al. 2016, Martizzi and Agrusa 2016). In other papers authors explored the contribution to the resolution of this problem adding a bulk motion of the gas in numerical simulations (Ettori et al. 2013; Rasia et al. 2014). In order to recover some of these problems the combined information from the different data sets in different wavelengths enables us to recover the triaxial structure and the orientation of the cluster and to quantify the non-thermal contributions to the pressure. In this framework a characterization of a flattened gravitational potential and the study, in this potential, the gas rotation may be useful to set some constraints for cosmological simulations.

Chapter 2

Models of clusters with rotating intracluster medium

2.1 Flattened NFW Density-Potential Pairs

The spherically averaged dark-matter halos found in cosmological dark-matter-only N-body simulations are well described by the Navarro et al. (1996) (hereafter NFW) profile

$$\rho(r) = \frac{\rho_0}{\frac{r}{r_s}(1+\frac{r}{r_s})^2}, \tag{2.1}$$

where r_s is the scale radius and ρ_0 is a reference value of dark-matter density. At a given redshift z the density of the universe is

$$\rho_{crit}(z) = \frac{3H(z)^2}{8\pi G}, \tag{2.2}$$

where G is the gravitational constant and

$$H(z) = H_0 \times \left[\Omega_\Lambda + \Omega_{\rm m}(1+z)^3\right]^{1/2}, \tag{2.3}$$

is the Hubble parameter at redshift z for an assumed flat Universe ($\Omega_{tot} = 1$). The cosmological assumptions are $\Omega_\Lambda = 0.7$ and $\Omega_m = 0.3$ and $\rho_{crit}(0)$ is $1.9 \times 10^{-29}\, h^2\, g/cm^3$ where h^2 is the dimensionless Hubble constant [1].

The NFW profile is singular (although the potential and mass converge near the center), and possess a characteristic scale where the profile changes shape. Near the scale radius r_s, the profiles are almost isothermal ($\rho \propto r^{-2}$).
The NFW profile is considered as a "universal" profile: it depicts well dark-matter halos over a wide range of masses as is it probed by cosmological N-body simulations (e.g. Navarro et al. 1996, Solanes et al. 1997 , Ghigna et al. 1998, Jing and Suto 2000, Klypin et al. 2002, Navarro 2004 and much more).

---

[1] The Hubble Law found by Edwin Hubble in 1929 describes that the Doppler shift of the galaxies increases linearly with the distance:

$$v_r = H_0 D \tag{2.4}$$

where v_r is the recession velocity and D is the distance of the object studied.

In this work we consider high-mass halos with virial mass of $M_{200} = 10^{15} M_{\odot}$ such that ρ_{crit} is:

$$\rho_{crit} = \frac{1}{200} \frac{3 M_{200}}{4 \pi r_{200}^3}, \tag{2.5}$$

where the virial radius is r_{200} is such that the average density within r_{200} is $200\,\rho_{crit}$. N-body simulations and galaxy clusters observations (e.g. Ettori et al. 2010) indicate that there is an anticorrelation between the masses of dark-matter halos and their concentration (c_{200}), more massive halos tend to be less concentrated than smaller ones.

Concentration is defined as the ratio of the virial radius, r_{200}, and the scale radius r_s:

$$c_{200} = \frac{r_{200}}{r_s}. \tag{2.6}$$

For instance Dolag et al. (2004) find

$$\log_{10}[c_{200}(1+z)] = A + B \log_{10}\left(\frac{M_{200}}{10^{15} M_{\odot}}\right), \tag{2.7}$$

with A= 0.6 and B =-0.4. For a fixed halo mass $M_{200} = 10^{15} M_{\odot}$ we obtain a concentration value of 3.98 (equation 2.7), while the virial radius is about 2 Mpc and resolving equation (2.6) we obtain a value for the scale radius of 519 kpc.

Concentration, scale radius and M_{200} fully determine a spherical NFW halo. From the Poisson equation

$$\nabla^2 \Phi = 4 \pi G \rho, \tag{2.8}$$

using the density distribution (2.1), we obtain the gravitational potential of the NFW model

$$\Phi = -4 \pi G \rho_0\, r_s^2 \,\frac{\ln(1 + r/r_s)}{r/r_s}. \tag{2.9}$$

Dark-matter halos are not spherically symmetric (e.g. Despali et al. 2017) so we build axisymmetric models with the profile similar to the NFW one. Other authors have studied gas and dark matter distribution in non-spherical potential: Salvador-Solé et al. (2012) studied the dark matter halos in triaxial potential, Rojas-Niño et al. 2016 showed how can be created a 3D positive density-potential of discs and Panou and Delikaraoglou 2012 presented how a gravitational potential could be expanded in triaxial ellipsoidal harmonics.

Here we construct axisymmetric NFW model following Ciotti and Bertin (2005) that presented a method to expand homeoidal potential from an ellipsoidal density distribution.

We start presenting the 3D radius of the ellipsoid m given by

$$m^2 = \frac{x^2}{a^2} + \frac{y^2}{b^2} + \frac{z^2}{c^2} \tag{2.10}$$

using Cartesian x, y, z. The parameters a, b and c are the semi-axes defined as $a > b > c$. This equation can be rewritten as

$$m^2 = \frac{x^2}{a^2} + \frac{y^2}{a^2(1-\epsilon)^2} + \frac{z^2}{a^2(1-\eta)^2}, \tag{2.11}$$

where we defined the two parameters $\epsilon \equiv 1 - b/a$ and $\eta \equiv 1 - c/a$.
This expansion is a general form of a triaxial ellipsoid. Axisymmetric distribution are obtained for $\epsilon = 0$ or $\eta = 0$ or $\eta = \epsilon$. The prolate case is when $\epsilon = \eta < 1$ and the oblate is when $\epsilon = 0$ and $0 < \eta < 1$. The homeoidal inner potential can be defined as (Chandrasekhar 1969):

$$\Phi(\mathbf{x}) = -\pi abc\rho_0 G \int_0^\infty \frac{\widetilde{\Delta\varphi}(\mathbf{x}, \epsilon, \eta)}{\Delta(\tau)}\, d\tau, \tag{2.12}$$

where $\mathbf{x}$ is the position vector,

$$\Delta(\tau) = \sqrt{(a^2 + \tau)(b^2 + \tau)(c^2 + \tau)}, \tag{2.13}$$

$$\widetilde{\Delta\varphi} = 2 \int_{m(\mathbf{x},\tau)}^\infty \tilde{\rho}(m) m\, dm, \tag{2.14}$$

and

$$m(\mathbf{x}, \tau)^2 = \frac{x^2}{(a^2 + \tau)} + \frac{y^2}{(b^2 + \tau)} + \frac{z^2}{(c^2 + \tau)}. \tag{2.15}$$

$\Delta(\tau)$ that is a ellipsoid radius such that $\Delta = \sqrt{a^2 + b^2 + c^2}$ for $\tau = 0$ and $\Delta \to \infty$ for $\tau \to \infty$. $\widetilde{\Delta\varphi}$ is the integral of the density on the three dimensional ellipsoidal radius to infinite.
To expand the potential we made it adimensional by rescaling for the density (ρ_0) and for the Poisson equation ($4\pi\rho_0 G a^2$), and subsituing $\epsilon = 1 - b/a$ and $\eta = 1 - c/a$. Thus the potential is

$$\tilde{\Phi} = -(1 - \epsilon)(1 - \eta)\frac{a}{4} \int_0^\infty \frac{\widetilde{\Delta\varphi}(\mathbf{x}, \epsilon, \eta)}{\Delta(\tau)}\, d\tau. \tag{2.16}$$

Now equations of $\tilde{\rho}(m)$ and $\tilde{\Phi}(m)$ can be expanded in Taylor series in order to show how the flattening will affect the spherical distribution and this will be the starting point to reproduce the expansion

$$\tilde{\rho}(m) = \tilde{\rho}(\tilde{r}) + \frac{\epsilon\tilde{y}^2 + \eta\tilde{z}^2}{\tilde{r}}\tilde{\rho}'(\tilde{r}) + \mathcal{O}(\epsilon^2 + \eta^2); \tag{2.17}$$

where

$$\tilde{\rho}' = \frac{d\rho}{dm} \qquad when \quad \epsilon = \eta = 0. \tag{2.18}$$

From equation (2.17) we can obtain the maximum flattening of our models (the maximum value of η and ϵ for which ρ is everywhere positive). The negative density is related to ρ' because it is the only term in the equation that, under particular values of η and ϵ, could become negative. If this occurs $\tilde{\rho}$ becomes negative and this is unphysical.
The Taylor expansion of equation (2.16) for $\eta \ll 1$ and $\epsilon \ll 1$

$$\tilde{\Phi} = \tilde{\Phi}_0(\tilde{r}) + (\epsilon + \eta)[\tilde{\Phi}_1(\tilde{r}) - \tilde{\Phi}_0(\tilde{r})] + (\epsilon\tilde{y}^2 + \eta\tilde{z}^2)\tilde{\Phi}_2(\tilde{r}) + \mathcal{O}(\epsilon^2 + \eta^2), \tag{2.19}$$

where:

$$\tilde{\Phi}_i(\tilde{r}) = \begin{cases} -\frac{1}{\tilde{r}}\int_0^{\tilde{r}} \tilde{\rho}(m)m^2\, dm - \int_{\tilde{r}}^{\infty} \tilde{\rho}(m)m\, dm, & (i=0); \\ -\frac{1}{3\tilde{r}^3}\int_0^{\tilde{r}} \tilde{\rho}(m)m^4\, dm - \frac{1}{3}\int_{\tilde{r}}^{\infty} \tilde{\rho}(m)m\, dm, & (i=1); \\ \frac{1}{\tilde{r}^5}\int_0^{\tilde{r}} \tilde{\rho}(m)m^4\, dm. & (i=2). \end{cases} \tag{2.20}$$

Substituting in the equation (2.20) the values of ρ from equation (2.1) and m from equation (2.11) we get:

$$\tilde{\Phi}_0(r) = -\frac{1}{s}\left[\frac{\ln(s+1)}{(s+1)} - 1\right] - \frac{1}{(s+1)}, \tag{2.21}$$

where $s = r/r_s$.
The second term of the expansions is

$$\tilde{\Phi}_1(r) = -\frac{1}{3s^3}\left[\frac{3s\ln(s+1)}{s+1} + \frac{3\ln(s+1)}{s+1} + \frac{s^3}{2s^2+2} - \frac{3s^2}{2s+2} - \frac{2s}{s+1} + \frac{1}{s+1} - 1\right] - \frac{1}{3(s+1)}, \tag{2.22}$$

the third one is

$$\tilde{\Phi}_2(r) = \frac{1}{s^5}\left[\frac{3s\ln(s+1)}{s+1} + \frac{3\ln(s+1)}{s+1} + \frac{s^3}{2s^2+2} - \frac{3s^2}{2s+2} - \frac{2s}{s+1} + \frac{1}{s+1} - 1\right]. \tag{2.23}$$

These terms must be inserted in the general equation (2.20) to obtain the general form of the gravitational potential for oblate and prolate models.
While replacing in the equation (2.17) the equation (2.1) we obtain the general equation of the density expansion:

$$\rho_{exp} = \frac{1}{s(1+s)^2} - \frac{\eta z^2 + \epsilon y^2}{s}\frac{1}{s^2(1+s)^2} - \frac{2}{s(s+1)^3}. \tag{2.24}$$

For the oblate case, we use

$$m^2 = \frac{x^2+y^2}{a^2} + \frac{z^2}{a^2(1-\eta)^2}, \tag{2.25}$$

given by equation (2.10) with $\epsilon = 0$ and $b^2 = a^2(1-\eta)^2$. So choosing $R = \sqrt{x^2+y^2}$ and $z = z$ and substituting in Eq: (2.25):

$$m^2_{obl}(r,z) = \frac{R^2}{a^2} + \frac{z^2}{b^2}. \tag{2.26}$$

The potential is

$$\Phi_{obl}(R,z) = \Phi_0(R) + \eta[\Phi_1(R) - \Phi_0(R)] + \eta z^2\,\Phi_2(R) + \mathcal{O}(\eta^2); \tag{2.27}$$

and the density is

$$\rho_{obl}(R,z) = \rho_0\left[\frac{1}{s(1+s)^2} - \frac{\eta z^2}{s}\frac{1}{s^2(1+s)^2} - \frac{2}{s(s+1)^3}\right]. \tag{2.28}$$

For the prolate case, instead, we have

$$m^2 = \frac{x^2}{a^2} + \frac{z^2 + y^2}{a^2(1-\epsilon)^2}, \tag{2.29}$$

given by equation (2.10) with $c^2 = b^2 = a^2(1-\epsilon)^2$ substituing $z' = x$ and $R' = \sqrt{y^2 + z^2}$ we have:

$$m^2_{pro}(R', z') = \frac{z'^2}{a^2} + \frac{R'^2}{b^2}; \tag{2.30}$$

and

$$\Phi_{pro}(R', z') = \Phi_0(R') + \epsilon[\Phi_1(R') - \Phi_0(R')] + \eta R'^2\, \Phi_2(R') + \mathcal{O}(\epsilon^2). \tag{2.31}$$

The density profile is

$$\rho_{pro}(R', z') = \rho_0 \left[\frac{1}{s(1+s)^2} - \frac{\epsilon R'^2}{s}\frac{1}{s^2(1+s)^2} - \frac{2}{s(s+1)^3}\right]. \tag{2.32}$$

In equation (2.32) we used $s = R'/r_s$ and ρ_0 is the physical normalization[2].

2.2 Dark-Matter Distribution

In this subsection, we present examples of flattened NFW dark matter potential computed with maximum flattening in both the oblate and the prolate cases introduced in section (2.1).

A spherical NFW dark matter distribution is presented in figure (2.1) where are highlighted the isodensity contours that are associated with isopotential regions. A high value of ϵ and η in the potential may create regions of negative dark matter density. We show dark matter maps with a high value of flattening $\eta \equiv 0.5$ and $\epsilon \equiv 0.5$ to display the presence of negative density.

The figure (2.2) shows the dark matter density distribution maps for an oblate and prolate potential. As it can be seen there are some structures on the edges of the isodensity contours and that are associated with the negative values of the density distribution due to the second term of the expansion ($d\rho/dm$ in equation 2.17).

The grey color in the maps in figure (2.2) is associated with the region where there are areas of negative density. The broken isodensity contours highlight regions where the density is negative.

These models are therefore unphysical.

Figure (2.3) presents a zoom of the maps (2.2) in different color scale in a squared region of 500 kpc radius in correspondence of the areas where we found a negative values of the dark-matter density. In these maps the broken lines of the isodensity contours are more evident than in the maps (2.2).

In chapter 3 will be presented models of gravitational potentials and dark matter distributions flattened but physical, so everywhere positive.

---

[2] The ρ_0 is the same as the spherical NFW.

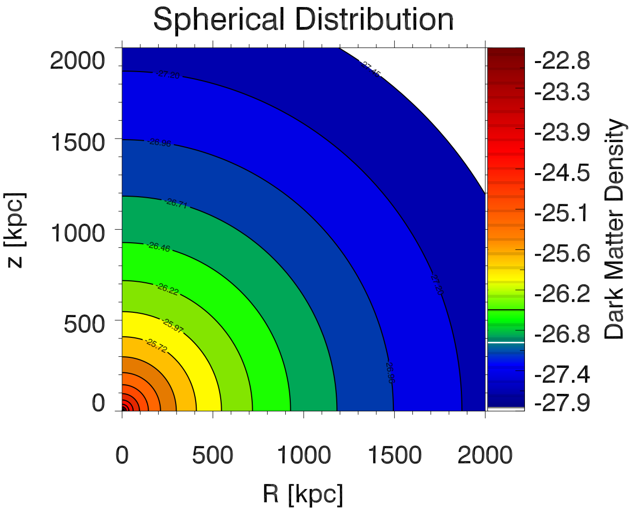

Figure 2.1: Map of dark-matter density in the meridional plane of a spherical NFW, with parameters $M_{200} \equiv 10^{15}\, M_{\odot}$, $C_{200} \equiv 3.98$ and $r_s \equiv 519$ kpc. The map is shown in physical scale with R and z that are expressed in kpc, the contours that are highlighted are referred to the logarithmic isodensity of dark matter in $g\ cm^{-3}$ scale.

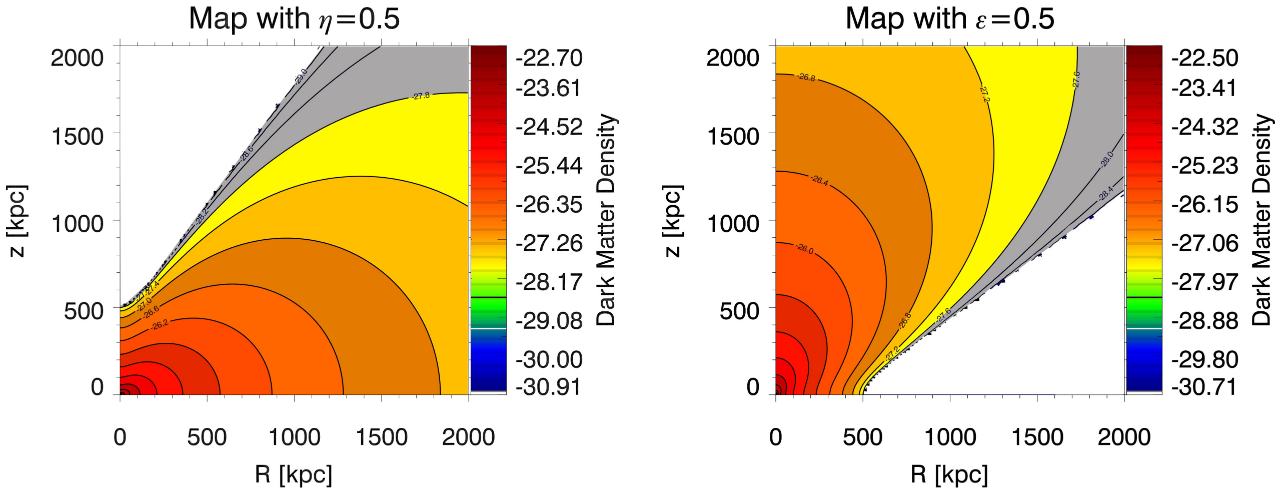

Figure 2.2: Dark-matter density map in the meridional plane in oblate (left) and prolate (right) expansion. The maps are created using the same physical parameters used to create the other dark-matter distribution. The maps are in logarithmic scale of $g\, cm^{-3}$. The grey region is where there is negative density defined with the broken contours lines.

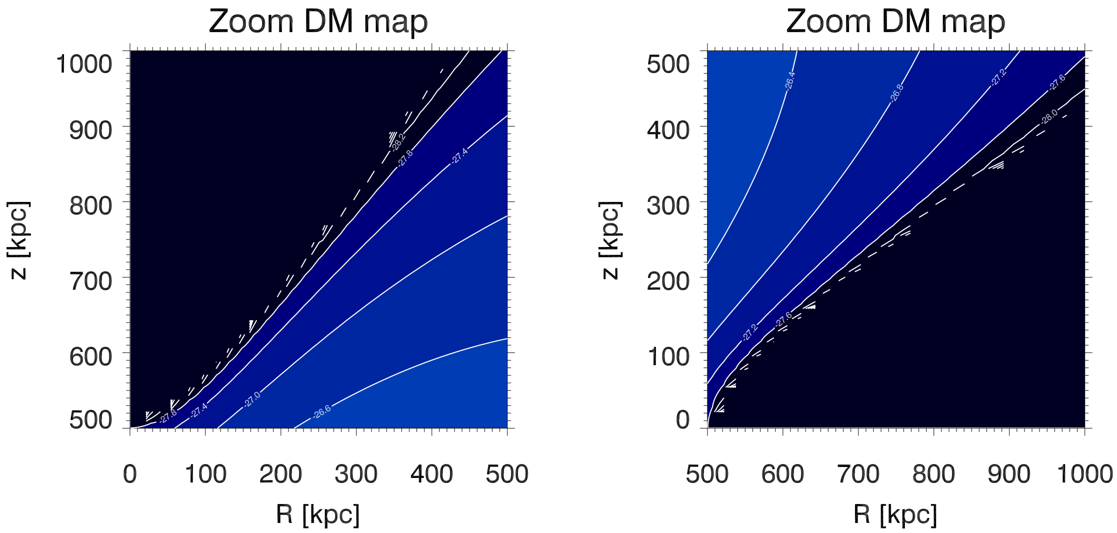

Figure 2.3: Zoom of the dark-matter density maps (2.2). The isodensity value are highlighted and the areas where we found negative density are more evident.

2.3 Hydrodynamics equations

In this section, we report the hydrodynamics equations that we used to build models of rotating ICM.

Euler's equation describes how velocity, pressure and density of a fluid are related under the effect of gravitational potential.

$$\frac{\partial \mathbf{u}}{\partial t} + \mathbf{u} \cdot \nabla \mathbf{u} + \frac{\nabla P}{\rho} = -\nabla \Phi, \tag{2.33}$$

where $\mathbf{u}$ is the gas velocity, Φ is the gravitational potential, ρ is the gas density and P is the pressure.

We consider stationary models (that are independent of time) in which the only non-zero component of the velocity is the azimuthal component u_φ is defined as

$$u_\varphi(R) = \Omega R, \tag{2.34}$$

where Ω is the angular velocity and depends only on radius. For the geometry of our model we use the Euler's equation in cylindrical coordinates (R, φ and z) that describes an axisymmetric gas system in rotation under effect of the gravitational potential

$$\frac{1}{\rho}\frac{\partial P}{\partial z}(R,z) = -\frac{\partial \Phi}{\partial z}(R,z), \tag{2.35}$$

$$\frac{1}{\rho}\frac{\partial P}{\partial R}(R,z) = -\frac{\partial \Phi}{\partial R}(R,z) + \Omega R. \tag{2.36}$$

The potential Φ is assumed to be axisymmetric. It is useful to define the effective potential

$$\Phi_{eff}(R,z) \equiv \Phi(R,z) - \int^{R} \Omega^2(R')\, R'\, dR', \tag{2.37}$$

that is a mathematical representation of how we can describe the effect of the rotation component to the stability of the gas. From the Poincaré-Wavre theorem (Tassoul 2007) we know that a cylindrical rotation pattern is a necessary and sufficient condition to have a barotropic stratification of density and pressure, so the isodensity and the isobaric surfaces coincide with the surfaces of constant effective potential Φ_{eff} and we have P=P(ρ).
For the gravitational potential $\Phi(R,z)$ we adopt the flattened axisymmetric NFW that is described in details in section (2.1).

2.4 Polytropic Distribution of the ICM

The gas distribution can be described as polytropic distribution, so:

$$\frac{P}{P_0} = \left(\frac{\rho}{\rho_0}\right)^{\tilde{\gamma}}, \tag{2.38}$$

where $P_0 \equiv P(\mathbf{x_0})$, $\rho_0 \equiv \rho(\mathbf{x_0})$ and $\mathbf{x_0}$ is a reference position and $\tilde{\gamma}$ is the polytropic index.
To obtain the distribution of pressure and density in terms of effective potential, we substitute in equation (2.35) the equation (2.38) and we get:

$$\gamma \frac{k_B T_0}{\mu m_p} \frac{\rho^{\tilde{\gamma}-1}}{\rho_0^{\tilde{\gamma}-1}} \nabla\rho = -\rho\nabla\Phi_{eff}(R,z), \tag{2.39}$$

where $T_0 \equiv T(\mathbf{x_0})$. Using $\Phi_{eff,0} \equiv \Phi_{eff}(\mathbf{x_0})$ and $\nabla\Phi_{eff} = (d\Phi_{eff}/d\rho)\nabla\rho$ we obtain:

$$\int_1^{\rho(\mathbf{x})/\rho} \tilde{\gamma} \frac{k_B T_0}{\mu m_p} \rho'^{\tilde{\gamma}-2} d\rho' = -\int_{\Phi_{eff,0}}^{\Phi_{eff}(\mathbf{x})} d\Phi'_{eff} \tag{2.40}$$

where we have $\rho' = \rho/\rho_0$.
If $\tilde{\gamma} \neq 1$, we can write the solution of equation (2.40)

$$\rho(R,z) = \rho_0 \left[1 + \frac{\tilde{\gamma}-1}{\tilde{\gamma}} \frac{\mu m_p}{k_B T_0} (\phi_{eff,0} - \phi_{eff})\right]^{\frac{1}{\tilde{\gamma}-1}} \tag{2.41}$$

that is the density distribution in the non-isothermal case. The isothermal case is defined by $\tilde{\gamma} = 1$ and the equation (2.41) is rewritten in this way:

$$\frac{k_B T_0}{\mu m_p} \frac{\nabla\rho}{\rho} = -\nabla\Phi_{eff}(R,z), \tag{2.42}$$

and the density distibution

$$\rho(R,z) = \rho_0 e^{-[\Phi_{eff}(R,z) - \Phi_{eff,0}](\mu m_p/k_B T_0)}. \tag{2.43}$$

By construction the isothermal models have a position-indipendent temperature. For the non-isothermal models instead we have

$$\frac{T}{T_0} = \left(\frac{\rho}{\rho_0}\right)^{\tilde{\gamma}-1}. \tag{2.44}$$

2.5 Composite Polytropic Distribution

In cool-core clusters there is a complex interplay between cooling and heating phenomena (see Hudson et al. (2010) and in section 1.3.1). We assume a stationary model with an increasing temperature in the innermost regions and a decreasing temperature in the outer part. We build these models as composite polytropic gas distribution (Nipoti et al. 2015)

$$\frac{P}{P_0} = \left(\frac{\rho}{\rho_0}\right)^{\tilde{\gamma}_{in}} \qquad if \quad \rho > \rho_0, \tag{2.45}$$

$$\frac{P}{P_0} = \left(\frac{\rho}{\rho_0}\right)^{\tilde{\gamma}_{out}} \qquad if \quad \rho < \rho_0. \tag{2.46}$$

Thus, the density profiles are:

$$\rho_{inner}(R,z) = \rho_0 \left[1 - (\tilde{\gamma}_{in} - 1)\frac{\mu m_p \Phi_{eff}}{\tilde{\gamma}_{in} k_B T_0}\right]^{\frac{1}{\tilde{\gamma}_{in}-1}} \qquad \rho > \rho_0; \tag{2.47}$$

$$\rho_{outer}(R,z) = \rho_0 \left[1 - (\tilde{\gamma}_{out} - 1)\frac{\mu m_p \Phi_{eff}}{\tilde{\gamma}_{out} k_B T_0}\right]^{\frac{1}{\tilde{\gamma}_{out}-1}} \qquad \rho < \rho_0. \tag{2.48}$$

The different behaviour of the distribution depends only on $\tilde{\gamma}_{in}$ and $\tilde{\gamma}_{out}$.

2.6 Velocity Pattern

The velocity patterns that we used are:

$$u_\varphi^2(s) = u_0^2 \left[\frac{\ln(1+s)}{s} - \frac{1}{1+s}\right], \tag{2.49}$$

$$u_\varphi^2(s) = u_0^2 \frac{s^2}{(1+s)^4}, \tag{2.50}$$

where $s = r/r_0$ is a normalized radius and r_0 is shown in table (2.1) for each models that we used.

The velocity pattern showed in equations (2.49, 2.50) were presented in the paper of Bianconi et al. (2013). Recently a paper from Baldi et al. (2017) obtained from numerical simulations of galaxy clusters a test for gas and dark-matter rotation. Baldi et al. (2017) also added another velocity profile that we do not use

$$u_\varphi^2 = u_0^2 \frac{s^2}{(1+s^2)^2}. \tag{2.51}$$

We decided to use the velocity profiles presented in Bianconi et al. (2013) leaving the r_0, a characteristic radius, as it was already set while for each model we have choosen a proper v_0 for fitting the ellipticity profiles.

The properties of the velocity laws that we used are summarized in table (2.1).

We adopted the rotation law VP2 (2.50) with two different velocity maximum to test the best fit with the data. In table (3.1) are shown the different velocity values and physical parameters of all models.

Table 2.1: Table of velocity profiles parameters

Eq.	Velocity Profile	r_0 [kpc]	v_0^{Obl} $[km/s]$	v_0^{Pro} $[km/s]$
2.49	VP1	170	336	1456
2.50	VP2A	120	705	2841
2.50	VP2B	120	1000	2800

For our models we want to reproduce the universal gas fraction that is defined as the ratio between the gas mass and the total mass of the cluster:

$$f_{gas} \equiv \frac{M_{gas}}{M_{200}}. \tag{2.52}$$

We imposed our models to have a reproduce a baryon fraction as observationally inferred (Eckert et al. 2011):

$$f_{gas}(< r_{200}) = (0.15 \pm 0.01) \left(\frac{k_B T}{10\, keV} \right)^{0.478}, \tag{2.53}$$

where T is the gas temperature. M_{200} is the total mass inside r_{200}, from the relation taken by Arnaud et al. (2005):

$$M_{200} = A_{200} \left(\frac{k_B T}{5\, keV} \right)^{\alpha}, \tag{2.54}$$

where:

$$A_{200} = 2.74 \times 10^{14} M_{\odot}, \tag{2.55}$$

and $\alpha = 1.49$. In our models we put $M_{200} = 10^{15}\, M_{\odot}$ at redshift 0.1. Using equation (2.54) we get a $8.7 \times 10^7\, K$ temperature for the ICM and from equation (2.53) we get a gas fraction of 0.13, so we fix $f_{gas} = 0.13$ for all our models. The value of gas fraction that we get from equations (2.53) and (2.54) is in agreement with the values obtained by Kravtsov et al. (2006) and Maughan et al. (2008).

2.7 Surface Brightness and Cooling Function

The X-ray surface brightness of an edge-on axisymmetric galaxy cluster can be computed using:

$$\Sigma(R, z) = 2 \int_R^{\infty} \frac{\dot{E}(R', z)\, R'\, dR'}{\sqrt{R'^2 - R^2}}, \tag{2.56}$$

where

$$\dot{E} = \frac{dE}{dt} = n_e n_i \Lambda(T, Z), \tag{2.57}$$

is the cooling rate. Λ is the cooling function that describes how the astrophysical gas emits photons due to different emission processes, depending on metallicity Z and temperature T. For simplicity we use the notation $\Lambda(T)$, omitting the explicit dependence of Z. For the hot ICM the dominant process is

Table 2.2: Parameters of the cooling function expansion from Tozzi et al. (2000). The physical units for C_1 is 10^{-22} $ergs\, cm^3\, s^{-1}\, keV^{-\alpha}$, for C_2 is 10^{-22} $ergs\, cm^3\, s^{-1}\, keV^{-\beta}$ and for C_3 is 10^{-22} $ergs\, cm^3\, s^{-1}$.

Metallicity $Z_\odot$	C_1	C_2	C_3
0	1.19×10^{-4}	6.3×10^{-2}	1.9×10^{-2}
0.1	2.8×10^{-3}	5.8×10^{-2}	4.0×10^{-2}
0.3	8.6×10^{-3}	5.8×10^{-2}	6.3×10^{-2}

Bremsstrahlung. In this process electrons in motion are decelerated by interacting with nuclei and protons.

In the relevant range of temperatures ($10^7 \sim 10^8$ K) the gas is almost completely ionized.
The most used tabulated cooling function is the Sutherland and Dopita (1993) that cover a wide range of temperatures ($10^4 - 10^{8.5}$) and it is computed for different metallicities. Λ is calculated by integrating the emission from all processes weighted by the energy of the photons:

$$\Lambda(T, Z_i) = \int_0^\infty E\, dE\, \frac{d\alpha}{dE}(E, T, Z_i), \tag{2.58}$$

where $d\alpha/dE$ is the energy-dependent line or continuum power (based on which process we are considering) and Z_i is the metallicity. The cooling function in the range $10^6 - 10^8$ K for three different abundances is presented in figure (2.4), this is taken from Peterson and Fabian 2006. In our work, we adopted the functional from Tozzi et al. (2000) that is an analytic approximation

$$\tilde{\Lambda} = \Lambda n_e n_i, \tag{2.59}$$

where n_i is the ions number density and n_e is electrons number density. $\tilde{\Lambda}$ is a polynomial expansion for an analytic form of the equation:

$$\tilde{\Lambda} = C_1 (k_B T)^\alpha + C_2 (k_B T)^\beta + C_3, \tag{2.60}$$

where we adopted $\alpha = -1.7$ and $\beta = 0.5$. The values of C_i, reported in table (2.2), allow reproducing the Sutherland and Dopita (1993) cooling function above $k_B T = 0.03\ keV$. We remind that for high energy astrophysics is common use identify the temperature in keV using the Boltzmann's constant[3] in the eV K^{-1} (8.617×10^5) to convert the temperature from kelvin into energy (eV).

---

[3] $k_B = 1.38 \times 10^{-16}$ erg K^{-1} in cgs units.

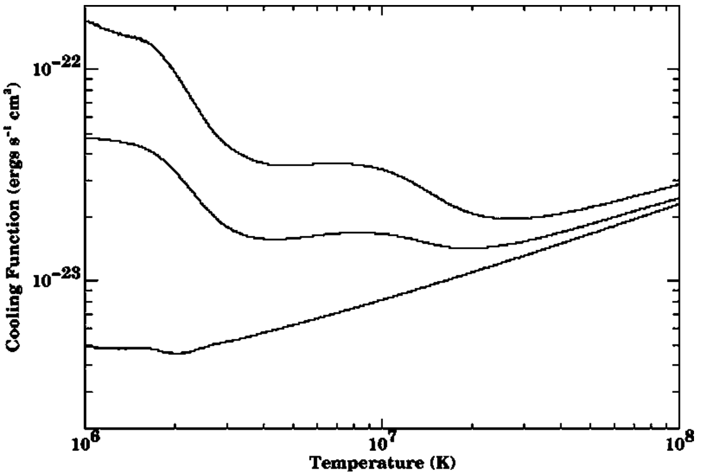

Figure 2.4: Cooling function taken from Peterson and Fabian (2006) from 10^6 to 10^8 K (top line of solar abundance, middle line for $0.3\,Z_{\odot}$ and bottom line for pure hydrogen and helium plasma). The cooling function represented is the form tabulated by Sutherland and Dopita 1993.

Chapter 3

Instrinsic properties of the models

3.1 Galaxy Cluster modelling

In this work we study three families of physical models: isothermal, non-isothermal and cool core.
We assumed the metallicity of the intercluster medium set to $0.3\,Z_{\odot}$ and constant in the cluster (a more realistic representation would be using a power law metal distribution that tends to be lower in the outskirt areas while in the center is much higher, e.g. De Grandi and Molendi 2001).
In this chapter we show the physical properties of the models both for dark matter and gas.

3.1.1 Dark Matter maps and profiles

The everywhere-positive dark matter density distribution, that we discussed in the section (2.1), is presented in figure (3.1) with the maximum value of flattening possible $\epsilon \equiv 1 - b/a \equiv 0.3864$. We found the same value for both oblate and prolate expansion because they derive from the same equations with a different choice of coordinates (R, z) (equations: 2.27, 2.31). The physical parameters of the potential, that determine a unique NFW potential, are $r_s \equiv 519$ kpc (from equation 2.1), $c_{200} \equiv 3.98$ (from equation 2.7) and $M_{200} \equiv 10^{15} M_{\odot}$.

The two maps figure:(3.1) show the dark-matter density distribution in oblate (left) (equation 2.28) and prolate (right) (equation 2.32) models using the maximum value of η in the first case and ϵ in the second one. It is evident that there is a drop in the inner part creating a sort of "peanut" shape. We show also the radial profile.

In figures (3.2) and (3.3) show the logarithmic density profiles of the oblate and prolate models normalized by the value of $\rho_{critic} \sim 10^{-29} \times h^2\, g\, cm^{-3}$ (2.5[1]), and the radius is normalized by the NFW scale radius (r_s). There is evi-

---

[1] For assumed $\Omega = 1$ ΛCDM cosmology.

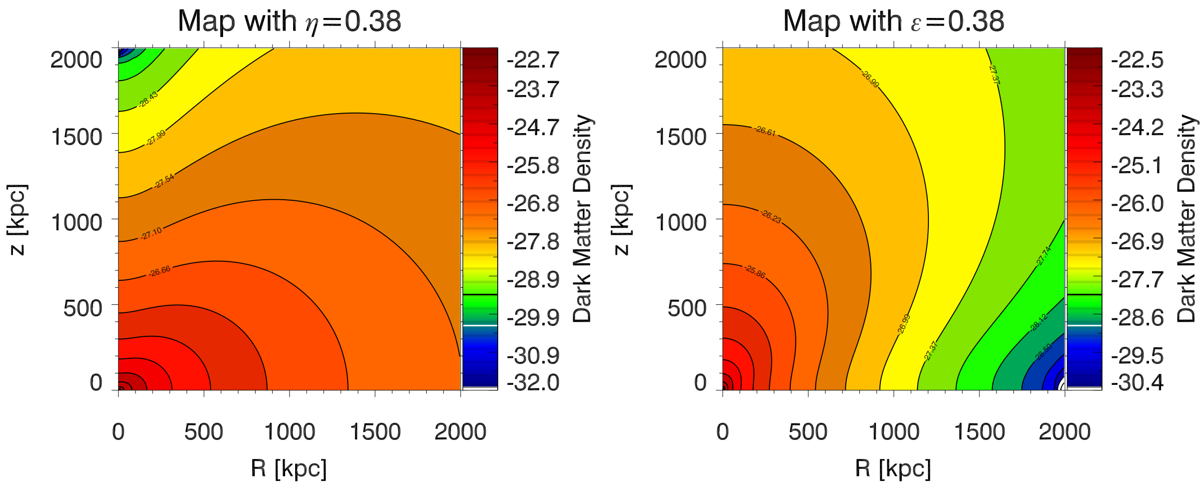

Figure 3.1: Dark-matter density maps in the meridional plane with maximim flattening ($\epsilon = 0.38$ and $\eta = 0.38$). The isodensity contours are highlighted. The maps are in physical scale and the left panel is the oblate distribution while the right is the prolate one, the contours are the isodensity in $g\ cm^{-3}$.

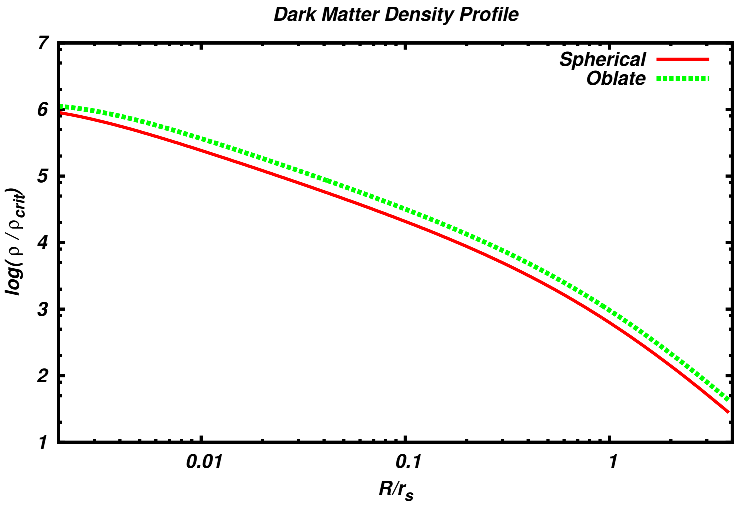

Figure 3.2: Radial density profile at $z = 0$ in the oblate case. The radius is normalized by the scale radius r_s and the density in the y-axis is normalized by a ρ_{critic} value (2.5). For comparison, the profile of the corresponding spherical NFW model is also shown.

dence that the oblate and the prolate cases tend to have slightly higher profile than the spherical NFW, especially in the inner part of the profile. In the prolate

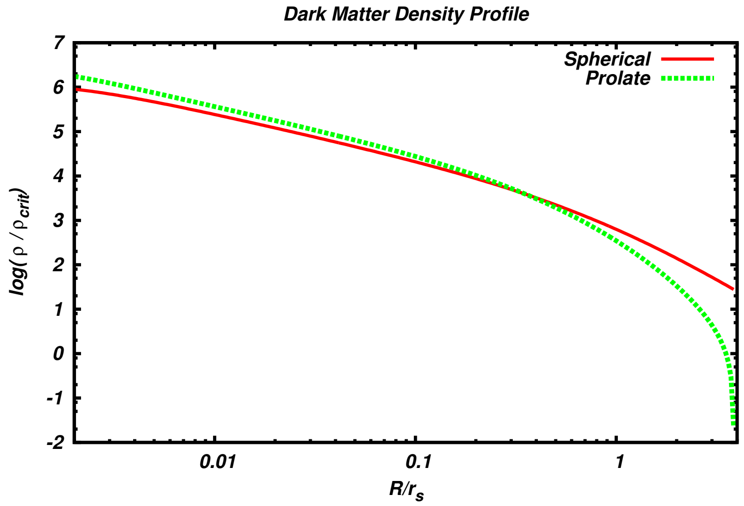

Figure 3.3: Radial density profile at $z = 0$ in the prolate case. The radius is normalized by the scale radius r_s and the density in the y-axis is normalized by a ρ_{critic} value (2.5).For comparison, the profile of the corresponding spherical NFW model is also shown.

case there is evidence of a steep drop in the outer radii of the cluster and it is associated with the shape of the expansion of the gravitational potential. This can be seen also in the oblate dark matter profile in the z direction.

In figures (3.4) and (3.5) the radial total mass profiles of dark-matter in the oblate and prolate cases compared with the analytic spherical mass profile of the NFW are shown. The analytic spherical mass is calculated as

$$M(r) = 4\pi\rho_0 r_s^3 \left[\ln(1 + r/r_s) - \frac{r/r_s}{1 + r/r_s}\right]. \tag{3.1}$$

The dark matter mass integrated in cylindrical coordinates is

$$M(r) = 4\pi \int_0^{r(R,z)} \rho(R, z)\, R\, dR\, dz \tag{3.2}$$

where $\rho(R, z)$ is for the oblate case equation (2.28) and for the prolate case equation (2.32).

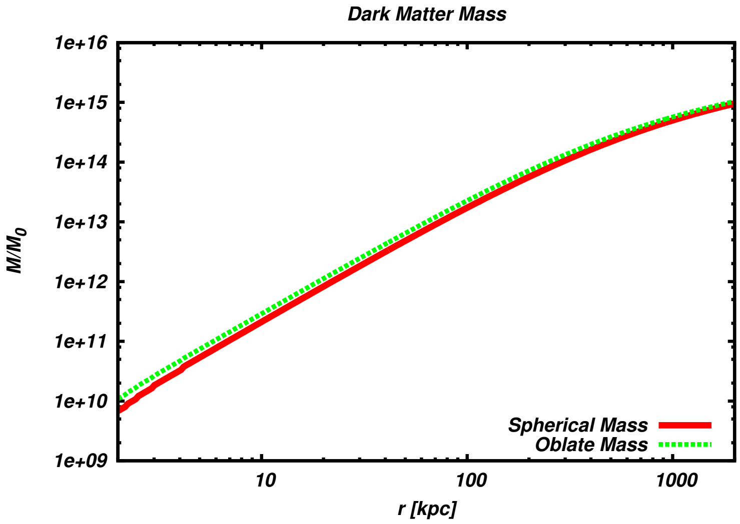

Figure 3.4: Radial dark-matter mass profile of the oblate halo. The red line is the analytic spherical mass of the corresponding spherical NFW halo and the green one is the computed oblate mass value obtained from dark-matter density equation (2.28).

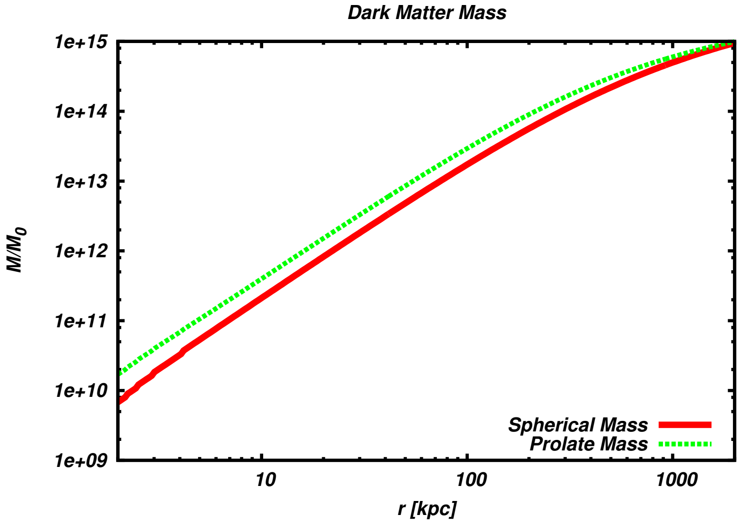

Figure 3.5: Radial dark-matter mass profile of the prolate halo. The red line is the analytic spherical mass of the corresponding spherical NFW halo and the green one is the computed prolate value obtained from dark-matter density equation (2.32).

3.1.2 Physical parameters

We set other physical values:

- in the isothermal models we assumed a constant temperature of T=8.7 ×

10^7 Kelvin ($7.5\,keV$).

- For the non-isothermal models we assumed a temperature $T_{\mathbf{x_0}} = 8.7\times10^7$ K, where $\mathbf{x_0}$ is the reference start of the grid (see appendix A.1, for further details) where we computed the temperature distribution using equation (2.44). In these models we adopted the polytropic index $\tilde{\gamma}_{in} = 1.14$ (equation 2.38).

- For cool core models we adopted the temperature and polytropic index from Nipoti et al. (2015) with three different temperatures ($T_1 = 6.9\,keV$, $T_2 = 7.1\,keV$ and $T_3 = 6.79\,keV$) and three different inner polytropic indices ($\tilde{\gamma}_{in,1} = 0.49,\ \tilde{\gamma}_{in,2} = 0.56$ and $\tilde{\gamma}_{in,3} = 0.43$) while the outer polytropic index is $\tilde{\gamma}_{out} = 1.14$ for all models (see equations 2.45 and 2.46).

All models are built to have a baryon fraction 0.13. We obtained these values starting from the density values from Bianconi et al. (2013) and calculating the gas mass at r_{200} we compared it with the total mass of dark-matter inside the same radius to verify our gas fraction and then we obtained a corrective factor for the initial gas density and we rescaled our models.
We calculated the gas mass and the dark matter mass inside r_{200} in cylindrical coordinates:

$$M_{gas} = 4\pi \int_0^{r_{200}} \rho_{gas}(R,z) R\, dRdz, \tag{3.3}$$

$$M_{200} = 4\pi \int_0^{r_{200}} \rho_{DM}(R,z)\, R\, dRdz; \tag{3.4}$$

so the gas fraction was obtained:

$$f_{gas} = \frac{M_{gas}}{M_{200}}. \tag{3.5}$$

In figure (3.6) we show the temperature profile at $z = 0$ in the non-isothermal and cool core models.

We use the same rotation laws for prolate case and oblate case and we changed the main parameter v_0 to fit the observations of isophotal flattening taken from Lau et al. (2012) and Fang et al. (2009).
The functional form of the rotation laws is the same as what was done in Bianconi et al. (2013) but the different shape of the potential lead the necessity of changing the v_0 parameter. In figure (3.7) we show the velocity profiles (equations 2.49 and 2.50) with the v_0 used to maximize the fit. Between the oblate and prolate rotation laws there is a difference of ~ 400 km/s at the characteristic radius r_0.

3.1.3 Gas maps and profiles

This subsection is dedicated to showing baryon maps and profiles. We present the gas density maps with VP1 velocity profile.

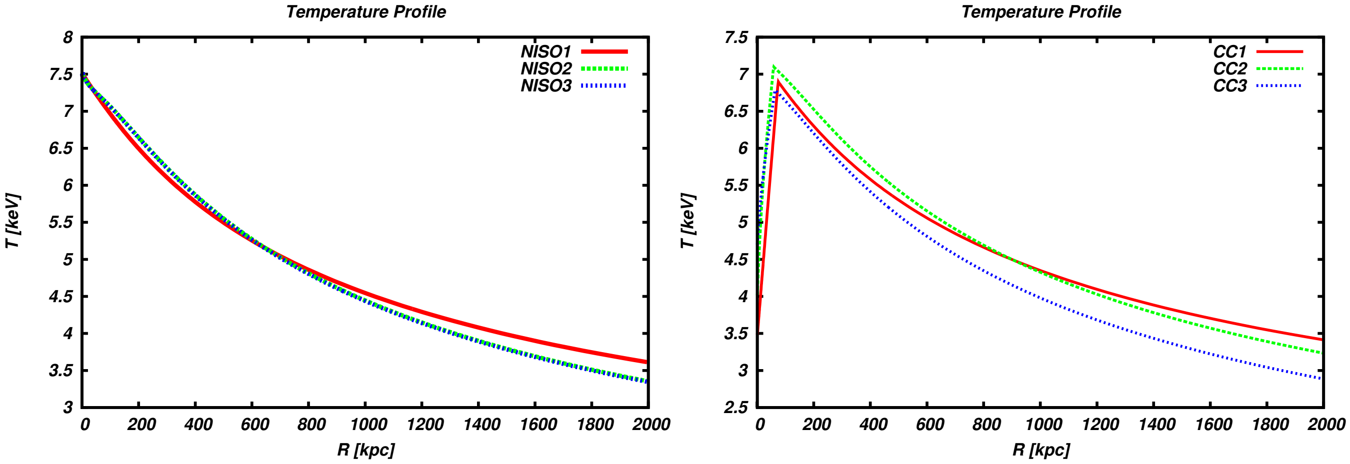

Figure 3.6: Radial temperature profiles at $z = 0$ in non-isothermal (left) and cool core models (right). The parameters are shown in table (3.1).

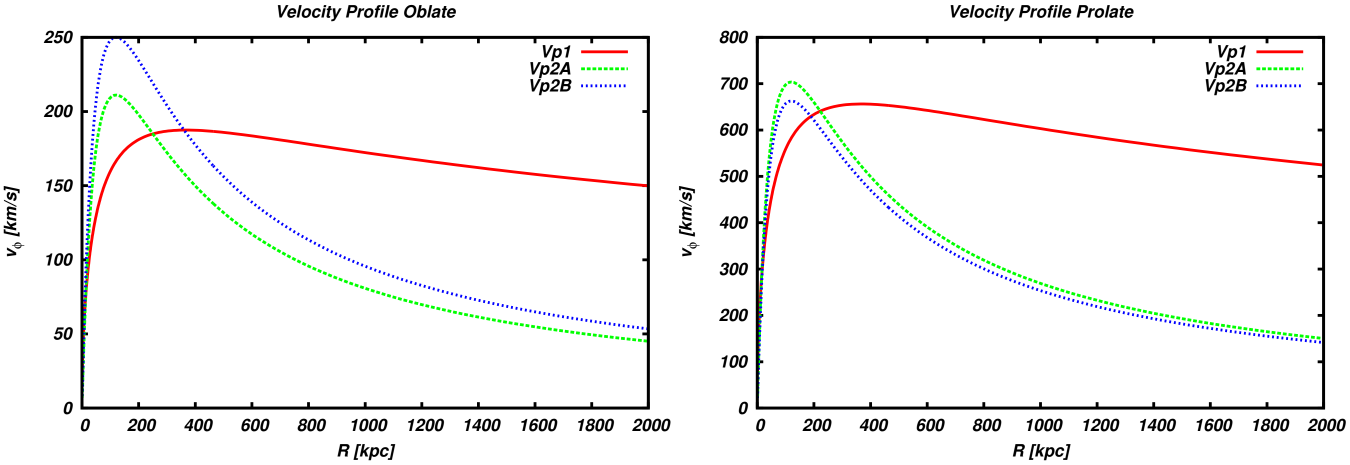

Figure 3.7: Velocity profiles in oblate (left) and prolate (right). The parameters are shown in table (3.1).

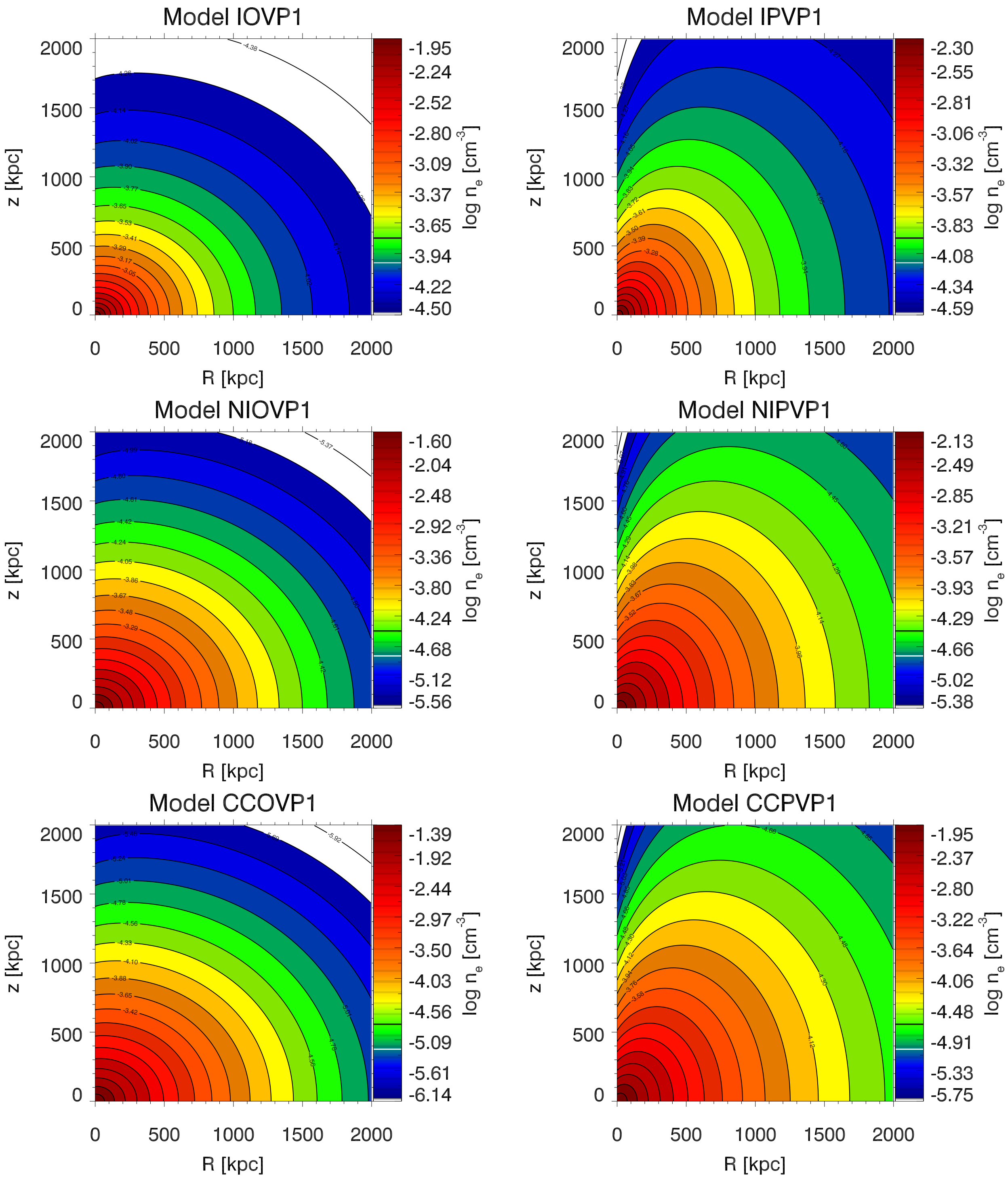

Figure 3.8: Gas density for isothermal (top), non-isothermal (mid), cool core (bottom) oblate (left) and prolate (right) VP1 models

The maps in figure (3.8) are really similar between them. We can see that the different geometry of the gravitational potential is evident in the gas distribution. We can note that the isothermal maps show a lower extension of distribution than what is observed in the non-isothermal and cool core models.

In figures (3.9) and (3.10) we present the density profiles for every oblate and prolate models towards the R and z direction.

The profiles presented in figures (3.9) and (3.10) are really similar due to the gas density in the starting point of the grid of the models. The differences between the gas density for the rotating models are of the order of $\sim 10\%$. For the prolate models we can see that non-rotating models have a higher density both at $z = 0$ and $R = 0$, this derives from the high impact of the velocity profile that changes in a significantly way the gas distribution. The differences between non-rotating and rotating models in the prolate case is of the order of $\sim 35\%$.

In the cool-core models we can note that there is the typical double trend of the gas distribution, where until a radius of 130 kpc the profile is almost flat while at larger radii it starts to drop.

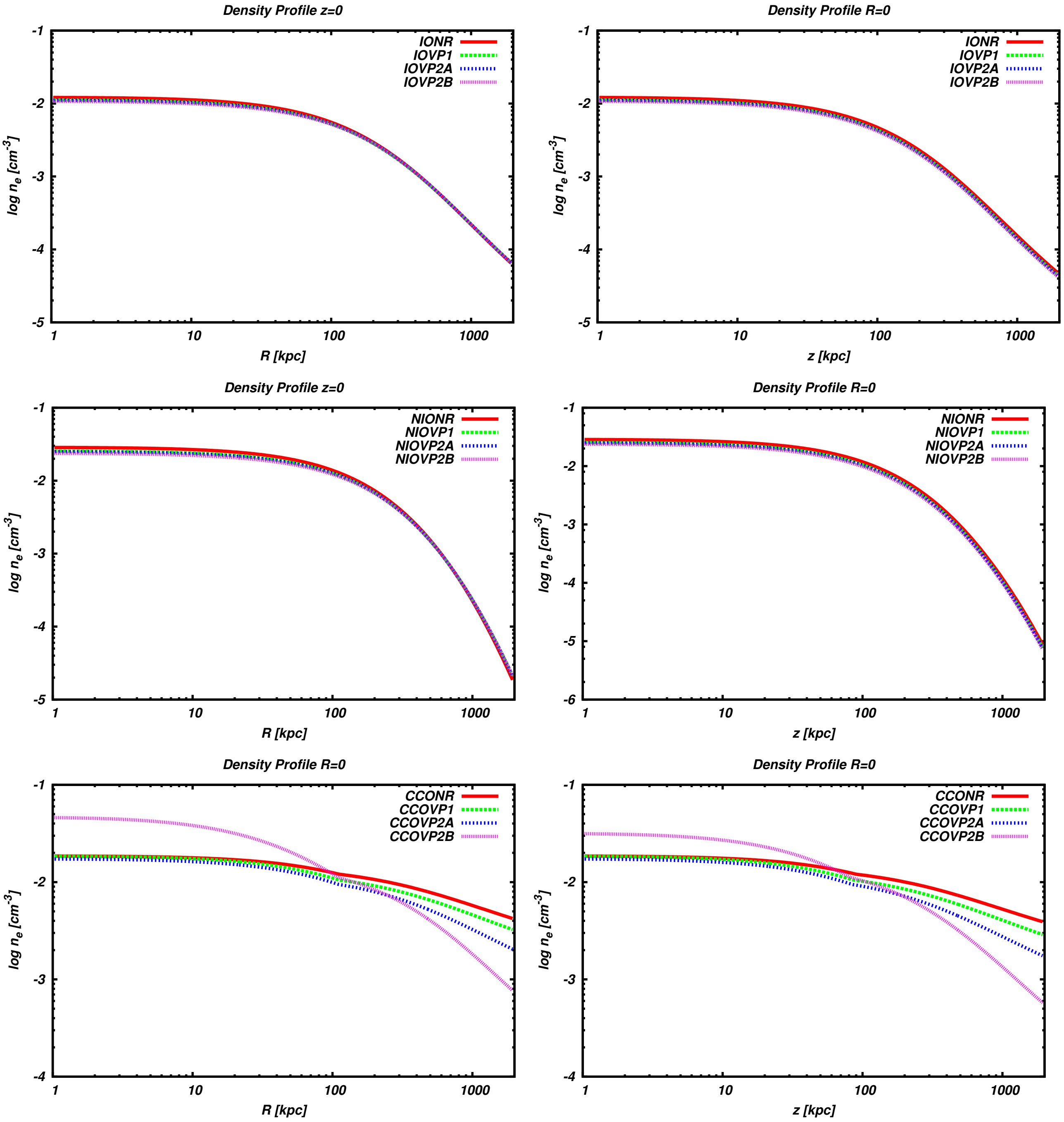

Figure 3.9: Gas density profile for oblate isothermal (top), non-isothermal (middle) and cool core (bottom) at $z = 0$ (left) and $R = 0$ (rigth).

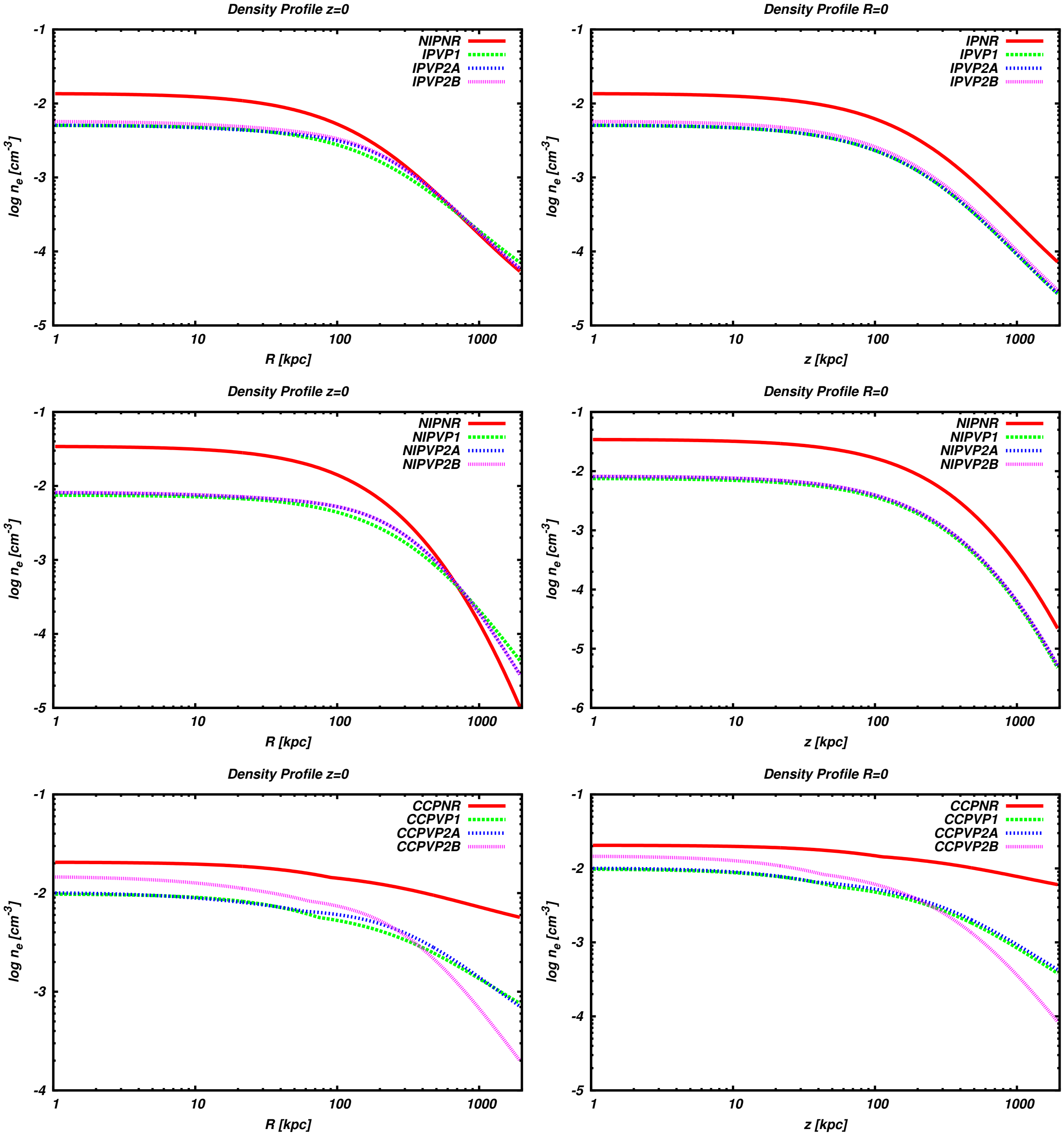

Figure 3.10: Gas density profile for prolate rotating isothermal (top), non-isothermal (middle) and cool core (bottom) at $z = 0$ (left) and $R = 0$ (right).

Table 3.1: Table of physical parameters of all models that we analyzed and their relative references to the figure. We set the metallicy of all our models to $0.3\ Z_\odot$. n_0 is the reference density, $\tilde{\gamma}_{in}$ and $\tilde{\gamma}_{out}$ are the polytropic indices, T_0 is the reference temperature and v_0 is the peak velocity of the velocity patterns.

Distribution	Potential	Name	Figure	n_0 $[cm^{-3}]$	$\tilde{\gamma}_{in}$	$\tilde{\gamma}_{out}$	T_0 $[K]$	Velocity pattern	v_0 $[km/s]$
Isothermal	Obl	IONR	4.5	9.89×10^{-3}	1	1	8.7×10^7	NR	0
	Pro	IPNR	4.5	1.34×10^{-2}	1	1	8.7×10^7	NR	0
Non Isothermal	Obl	NIONR	4.5	2.09×10^{-2}	1.14	1.14	8.7×10^7	NR	0
	Pro	NIPNR	4.5	2.49×10^{-2}	1.14	1.14	8.7×10^7	NR	0
Cool Core	Obl	CCONR	4.5	4.53×10^{-2}	0.49	1.14	8.0×10^7	NR	0
	Pro	CCPNR	4.5	5.50×10^{-2}	0.49	1.14	8.0×10^7	NR	0
Isothermal	Obl	IOVP1	4.6	1.09×10^{-2}	1	1	8.7×10^7	VP1	336
	Obl	IOVP2A	4.6	1.00×10^{-2}	1	1	8.7×10^7	VP2A	705.5
	Obl	IOVP2B	4.6	1.06×10^{-2}	1	1	8.7×10^7	VP2B	1000
Non Isothermal	Obl	NIOVP1	4.7	2.52×10^{-2}	1.14	1.14	8.7×10^7	VP1	336
	Obl	NIOVP2A	4.7	2.47×10^{-2}	1.14	1.14	8.7×10^7	VP2A	705.5
	Obl	NIOVP2B	4.7	2.34×10^{-2}	1.14	1.14	8.7×10^7	VP2B	1000
Cool Core	Obl	CCOVP1	4.8	1.04×10^{-2}	0.49	1.14	8.0×10^7	VP1	336
	Obl	CCOVP2A	4.8	9.44×10^{-3}	0.56	1.14	8.2×10^7	VP2A	705.5
	Obl	CCOVP2B	4.8	1.10×10^{-2}	0.43	1.14	7.8×10^7	VP2B	1000
Isothermal	Pro	IPVP1	4.6	5.54×10^{-3}	1	1	8.7×10^7	VP1	1344
	Pro	IPVP2A	4.6	5.05×10^{-3}	1	1	8.7×10^7	VP2A	2456
	Pro	IPVP2B	4.6	1.82×10^{-3}	1	1	8.7×10^7	VP2B	2700
Non Isothermal	Pro	NIPVP1	4.7	7.49×10^{-3}	1.14	1.14	8.7×10^7	VP1	1456
	Pro	NIPVP2A	4.7	8.02×10^{-3}	1.14	1.14	8.7×10^7	VP2A	2841
	Pro	NIPVP2B	4.7	8.13×10^{-3}	1.14	1.14	8.7×10^7	VP2B	2800
Cool Core	Pro	CCPVP1	4.8	5.64×10^{-3}	0.49	1.14	8.0×10^7	VP1	1456
	Pro	CCPVP2A	4.8	6.54×10^{-3}	0.56	1.14	8.2×10^7	VP2A	2841
	Pro	CCPVP2B	4.8	8.27×10^{-3}	0.43	1.14	7.8×10^7	VP2B	2800

Chapter 4

Photometric Observables

4.1 Measuring the shape of the isophotes

In this chapter we will present the photometric observables of the ICM models like X-ray surface brightness maps and profiles. We will study in detail the flattening of the isophotes.

The X-ray surface brightness maps are the observables that can be used to define the shape of the gas distribution and, at least for non-rotating ICM, the shape of potential, like was discussed in many papers like Binney and Strimpel (1978), Fabricant et al. (1984) and Buote and Tsai (1995).

The intracluster medium emits X-ray photons mainly via Bremsstrahlung radiation, depending on the density, temperature and metallicity of the gas (Sarazin 1988). We want to study the flattening of the X-ray isophotes because we want to make our models as much as possible similar to real clusters comparing them with observational data from the papers of Fang et al. (2009) and Lau et al. (2012).

We explore individually each model (both rotating and non-rotating models) to evaluate how much the rotation effect is visible and important in the flattening of the isophotes. Before exploring the analysis of the models we present a brief description of the methods to evaluate the isophotes ellipticity and the method that we used.

4.1.1 Ellipticity Profile

The method we adopted for calculating the ellipticity of the isophotes of the surface brightness distribution is based on the computation of the inertia matrix. By diagonalizing this object, we can obtain the moments associated with the axes of the distribution.

Starting with the calculus of the inertia matrix, different choices are possible for the selection of the region where calculating the inertia moments, for instance we can choose a circular or elliptical annulus.

The method works best if the surface brightness is almost constant inside the selected region (Dubinski and Carlberg 1991), but using simple shapes for selection, like circles and ellipses, this is not always true, especially in the inner

parts of the distribution.
We will then compare the model isophotes ellipticity with the values observed in many X-ray observations (e.g. Fang et al. 2009, Lau et al. 2012).
To measure the ellipticity of the isophotes, we use the method that is described in the paper of Lau et al. (2012) (that is an application of the original method provided by Dubinski and Carlberg 1991 for dark matter halos in N-body simulations). The method consists in selecting a circular annulus in the X-ray surface brightness and, in that region, calculate the inertia moments. The method used in Lau et al. (2012) adopted a "fitting shape" of the selection. The selected region started from a circular annulus then the evaluation of the first flattening is used to change the selection turning it into an ellipse with the computed ellipticity, that should have better agreement with the real shape of the isophotes. The procedure is then iterated until $\epsilon_i \leq 10^{-4}\epsilon_{i-1}$, where ϵ_i is the current estimate of the ellipticity and ϵ_{i-1} is the previous estimate. There are other methods to evaluate the ellipticity of the isophotes. In the analysis of observed galaxy clusters a method that is often used is based on the evaluation of the fit between the surface brightness isophotes and a general shape (for instance using a toy-ellipse using the `IDL` procedure `ellfit`). Thanks to this comparison we can obtain the value of the flattening, the axial ratio and the angle of the distribution.
However, for consistency in this work we used the method explained in Lau et al. (2012) because we compare our models to their observational data.

4.1.2 Ellipticity Using Inertia Moments

In this subsection, we will provide a brief exposition of the method we used to measure the ellipticity profile of the X-ray isophotes of the models. Let us consider a surface brightness map Σ in a Cartesian system of coordinates (x_i, x_j). To obtain the value of ellipticity we built the inertia tensor where each element of the matrix can be expressed as:

$$I_{ij} = \sum_{\alpha} \Sigma_\alpha x_{\alpha,i} x_{\alpha,j}, \tag{4.1}$$

where the objects I_{ij} are called moments of inertia about the corresponding axes, Σ_α is the weight (the surface brightness) in a region, defined by α, calculated in the direction i and j.

The tensor is symmetrical so we have

$$I_{ik} = I_{ki}. \tag{4.2}$$

Then the Inertia tensor is (Landau and Lifshitz 1969)

$$I \equiv \begin{pmatrix} I_{xx} & I_{xz} \\ I_{zx} & I_{zz} \end{pmatrix},$$

where we called $x_i = x$ and $x_j = z$. To compute the inertia matrix we use the eigenvalues λ: we sum all the components in the selected region and we compute the elements of the matrix obtaining

$$I - \lambda\mathbf{I} \equiv \begin{pmatrix} I_{xx} - \lambda & I_{xz} \\ I_{zx} & I_{zz} - \lambda \end{pmatrix}$$

where **I** is the identity matrix; calculating the determinant of the above matrix we get the eigenvalues $\lambda = \lambda_i$ and $\lambda = \lambda_j$ so the ellipticity is:

$$\epsilon = \begin{cases} 1 - \sqrt{\dfrac{\lambda_i}{\lambda_j}}, & if\ \lambda_i < \lambda_j; \\ 1 - \sqrt{\dfrac{\lambda_j}{\lambda_i}}, & if\ \lambda_j < \lambda_i. \end{cases} \tag{4.3}$$

We are free to choose along what axis we can calculate the inertia moments. We have the choice between a horizontal and vertical selection based on the geometry of the model taken in account. To select the best region to extract the eigenvalues we can choose a radius, for example r_{500}, and we compute the I_{xx} and I_{zz} within a circular aperture of radius r_{500} then:

$$I_{xx} > I_{zz} \ \Rightarrow \quad Horizontal\, Selection; \tag{4.4}$$

$$I_{xx} < I_{zz} \ \Rightarrow \quad Vertical\, Selection. \tag{4.5}$$

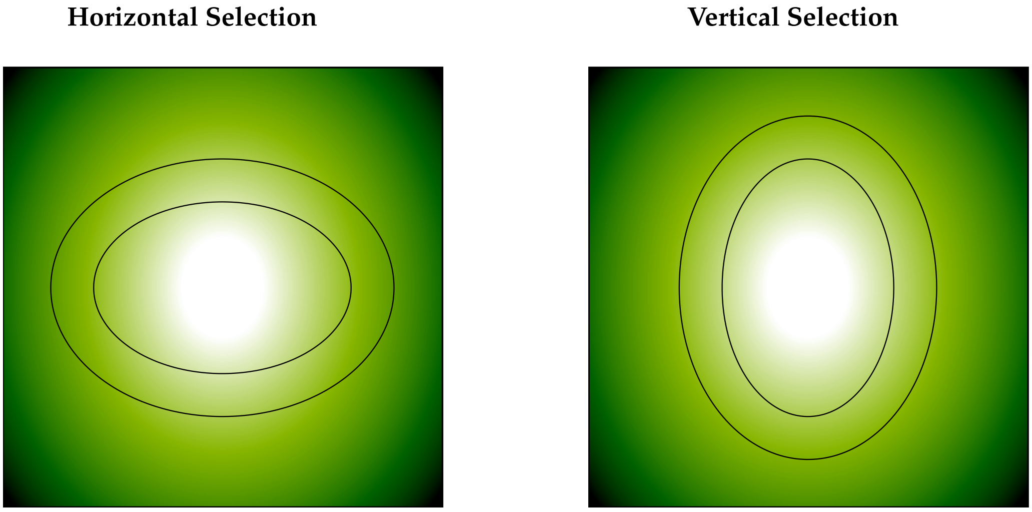

Figure 4.1: In this graph we show how we select the elliptic annuli region where we evaluate the ellipticity of the isophotes in the prolate non-rotating case. It is evident that the selection in the horizontal direction tends to take in account too many contributes with different weights making the evaluation worse.

In figure (4.2) we can note the big difference between the effect of the horizontal and vertical selection. In the figure (4.2) the ellipticity measured with the horizontal selection is almost increasing until $0.3\, r_{500}$ where it goes over the limits of the observational points (above 0.28). While for the vertical selection we measure a growth starting from $0.04\, r_{500}$ and the values are comparable with the observational points (between 0.15 and 0.20).
For all the rotating models we adopted the horizontal selection while for the prolate non-rotating case, we needed to choose the vertical selection because

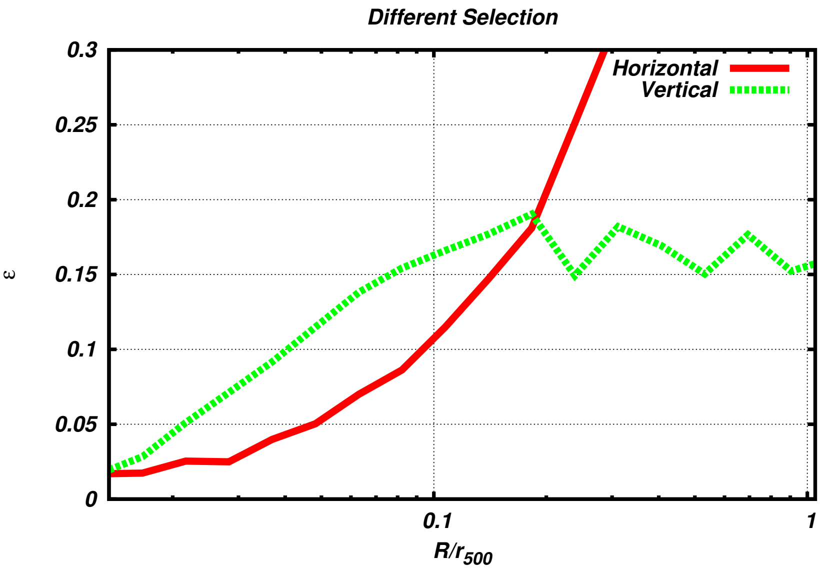

Figure 4.2: Results of method for different selection of the prolate isothermal non-rotating model with R (red line) and z (green line), horizontal and vertical selections as shown in figure 4.1.

the flattening of the surface brightness isophotes are in mainly in that direction. We show in figure (4.1) the effect of the choice in the horizontal and vertical orientation in the X-ray map for a prolate non-rotating model, it is evident that the different portions of surface brightness regions selected with the radial choice (left figure) will lead a better measurement.

4.1.3 Test for evaluating the ellipticity

In order to test the reliability of our method for evaluating the ellipticity we decided to make a toy model distribution (figure 4.3) with a fixed and known flattening and we expected that the values obtained with the measurements will have good agreement with what we set.
We created a toy model distribution with know axial ratio starting from the definition of the ellipsoidal radius m

$$m = R^2 + \frac{z^2}{(1-\epsilon)^2}, \tag{4.6}$$

where we set $\epsilon \equiv 0.3$. This is the radius where is stratified the power law distribution chosen for the toy model

$$\Sigma(m) = \left(\frac{m}{m_0}\right)^{-1}, \tag{4.7}$$

m_0 is an arbitrary constant and we have chosen a power law for semplicity.

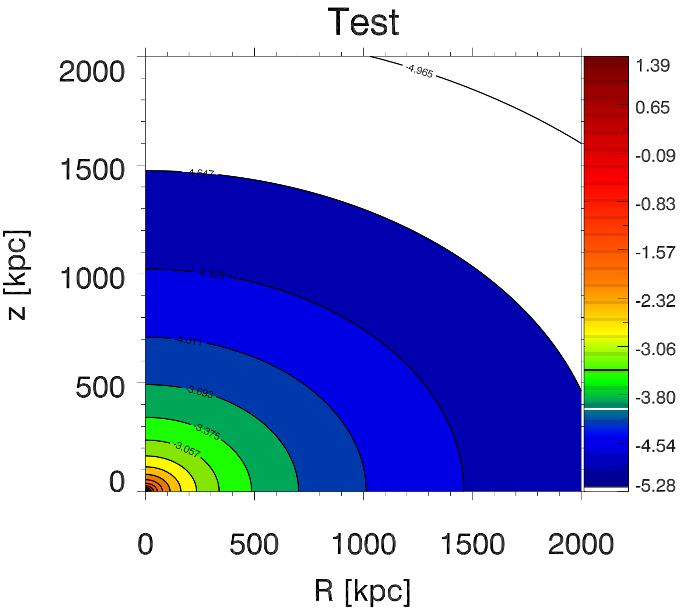

Figure 4.3: This is the surface brightness of a toy model with flattening of $\epsilon = 0.3$ in physical scale.

In figure (4.3) we show the surface brightness distribution of the toy-model we used the horizontal method for evaluating the inertia moments inside elliptical coronae and obtaining the eigenvalues of the axes for obtaining the ellipticity.
In figure (4.4) we can see the ellipticity profile until $r_{500} = 1345$ kpc. The very inner parts of the profile in figure (4.4), the first ~ 30 kpc, show larger discrepancies probably due to the way we compute the inertia moments or from how we built the main physical parameters where we may suffer from characterizing the shape of the innermost part of the distribution. Using a more refined grid (see A.1 for a description) or a more precise method to select the regions to compute the inertia moments would have constrained better the inner part, leaving unchanged what we observe in the remaining plot. In fact starting from $0.06\ r_{500}$ the profile is in good agreement with what we expect, excepting for fluctuations of the measurements that are inside $10\% \sim 15\%$ of the value. But for our purposes this method is reliable enough.

For the model with fixed flattening of 0.3 we measure, with our method, a mean value of 0.27 (as can be seen in figure 4.4).
We assumed the standard deviation as error for each measurement. We are aware that the shape of the profile is not so clear but it suffers from the way

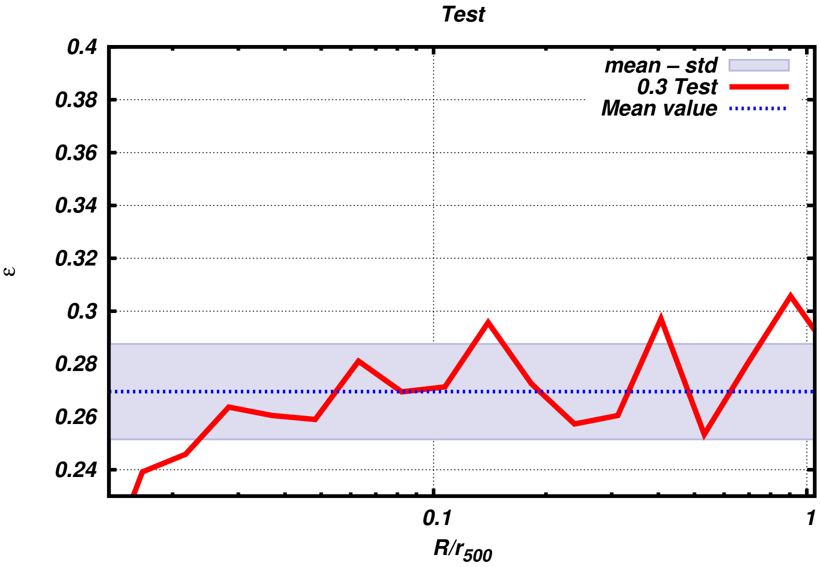

Figure 4.4: Ellipticity profile of the toy model until r_{500}. The horizontal line is the average value and the shadowed band indicates the standard deviation.

the selection is made but it reproduces the observed values with a sufficient approximation for our purpose. This method is what we used for evaluating the ellipticity profiles in all cluster models in the next section (4.2).

4.2 Photometry of the cluster models

In this section, we present the surface brightness maps for every model, rotating, non-rotating, oblate and prolate. For more information about the models check the table (3.1) where are presented the temperature, velocity profile values and density value of the starting point of the grid.
We also show the surface brightness profiles and ellipticity profiles of every model compared to the observational data.
The observations are taken from two different instruments: `CHANDRA` (Fang et al. 2009) and `ROSAT PSPC` (Buote and Canizares 1996); the second performed the analysis at the outer radii of clusters while the first one, using a follow-up method, examined the innermost parts of a sample of clusters obtaining a full coverage of the structure. The ellipticity profiles are normalized to $r_{500} = 1345$ kpc to be consistent with the work of Lau et al. (2012).

4.2.1 Surface Brightness Maps

We present the surface brightness maps of the different models we built. We separated the models in rotating and non-rotating showing the main differences and the peculiarities of the surface brightness maps.

For rotating models we adopted the velocity profiles from Bianconi et al. (2013) in the formulation shown in equations (2.49) and (2.50) with the parameters of initial velocity (v_0) changed to better reproduce the observation. All the physical parameters are shown in table (3.1).
We recall the velocity parameters reported in table (4.1), those are the parameters of the rotation profiles that were used in the oblate models and prolate models.

Velocity Pattern VP	r_0 $[kpc]$	v_0^{Obl} $[km/s]$	v_0^{Pro} $[km/s]$
1	170	336	1456
2A	120	705.5	2841
2B	120	1000	2800

Table 4.1: Velocity pattern parameters for oblate and prolate models

4.2.2 Non-Rotating Models

We start presenting the surface brightness maps of the non-rotating models (isothermal, non-isothermal and cool core) both oblate and prolate. We are interested in showing this type of maps because they represent a direct observable of the shape of the gravitational potential in the absence of rotation.
The physical parameters used to create these models are shown in table (3.1).

We can note in figure (4.5) that the isothermal models (4.5, top) tend to have a flatter shape both in oblate and prolate potential while the non-isothermal

(4.5, middle) and cool core models (4.5, bottom) are more similar and more rounder shape, even without the support of rotation.

4.2.3 Isothermal Rotating Models

In this subsection we will discuss about the surface brightness maps of the isothermal models both prolate and oblate.

In the maps (4.6) we can notice that the prolate models show a peaked shape in the region of $R \sim 150$ kpc in correspondence of the peak of the velocity profile. This peculiarity of the prolate models is not so evident in the oblate models that have a less peaked shape.

4.2.4 Non-Isothermal Rotating Models

In figure (4.7) we present the non-isothermal rotating models. Like what was already evident in the isothermal models, the prolate models have a peaked shape in correspondence of the peak of rotation profile and like was already known from non-rotating models, the non-isothermal, have a larger extension of brightness surface.

4.2.5 Cool Core Rotating Models

In the cool core models, figure (4.8) the differences with the non-isothermal models are really few and we find the same characteristic analyzed in the previous models.

4.3 Surface Brightness Profiles

The surface brightness of the models is a fundamental parameter in our work, so we decided to reproduce the profiles of this quantity in both radial and azimuthal direction.

In the figures (4.9) and (4.10) we show the surface brightness profiles for all models starting with the oblate (figure 4.9) and the prolate (figure 4.10).
We can say that in the oblate models the non-isothermal and isothermal models are similar and comparable (both rotating and non-rotating), this derives from the small differences in the density profiles, where we presented in section (3.1.3). The cool-core models present the typical double-trend in the inner part and in the outer (after 130 kpc) region of the cluster that is observed also in the density profiles.
As already discussed for the density profiles, the prolate models present a higher surface brightness in the non-rotating case. Comparing oblate and prolate surface brightness profiles we can notice that the oblate models tend to have a higher profile, about an order of magnitude, compared the other models.

model	$< \epsilon_{obl} >$	$< \epsilon_{pro} >$
INR	0.11 ± 0.014	0.13 ± 0.012
NINR	0.11 ± 0.015	0.12 ± 0.015
CCNR	0.14 ± 0.013	0.13 ± 0.015

Table 4.2: Mean ellipticity value for the non rotating models (isothermal, non-isothermal and cool core)

4.4 Ellipticity Profiles

The analysis of the ellipticity profile of the isophotes is the main term of comparison between our models and the real observations. We worked to obtain the maximum correspondence between the models observables and what was observed in Lau et al. 2012.

4.4.1 Non-Rotating Models

In figure (4.12) we can easily note that, even without the support of a rotation velocity, at $0.1\, r_{500}$ there is quite good agreement with the observational data due to the flattening of the potential.
We measure the mean ellipticity for the models, reported in table (4.2), where we also show the fluctuations of the values.

The ellipticity profiles of both oblate and prolate models are very similar in this case and it is in line with what expected because they were built under the same assumptions.
These models tend to be quite reliable in reproducing the ellipticity observed even without inserting a motion of the gas. This is predictable because the flattening of the potential leads a flattening in the density distribution. On average at radii larger than $0.1\, r_{500}$ we find a better fit of the observational data for almost every model, while in the innermost part of the profile our models show a lower trend: this can be related to a bad evaluation of the inertia moments in the innermost regions (see the analysis in section 4.1.1), like what happens at small radii, or due to a physical effect of growth of the shape of the gas distribution that creates less flattened isophotes in the inner part.

4.4.2 Isothermal Rotating Models

In the panel (4.12) are shown the isothermal rotating models oblate (left) and prolate (right) with the different velocity profile VP1 (top), VP2A (middle) and VP2B (bottom). Analyzing the fitting of the models with the observational points we can say that the oblate models show a growing trend distancing from the centre of the cluster and there is no correlation between the shape of the velocity profile and the ellipticity profile. This effect has been evident since from the analysis of the surface brightness maps of these models. For the prolate models instead there is a greater impact of the velocity profile. In fact the velocity pattern 2 (equation 2.50) creates a higher peak ($R \sim 0.1\, r_{500} \sim 150$ kpc) that is evident even in the ellipticity analysis. The first velocity pattern

model	$< \epsilon_{obl} >$	$< \epsilon_{pro} >$
IVP1	0.15 ± 0.015	0.12 ± 0.016
IVP2A	0.16 ± 0.015	0.17 ± 0.02
IVP2B	0.18 ± 0.014	0.14 ± 0.02

Table 4.3: Mean ellipticity value for the rotating isothermal models.

model	$< \epsilon_{obl} >$	$< \epsilon_{pro} >$
NIVP1	0.14 ± 0.016	0.11 ± 0.016
NIVP2A	0.15 ± 0.017	0.16 ± 0.02
NIVP2B	0.17 ± 0.015	0.16 ± 0.02

Table 4.4: Mean ellipticity value for the rotating non-isothermal models.

(VP1, equation 2.49) for the prolate model instead shows a lower agreement with the observational points and increasing the initial velocity (v_0) would not have changed anything.
In table (4.3) we show the mean ellipticity for the models with the fluctuations.

4.4.3 Non-Isothermal Rotating Models

The results of the non-isothermal models are really similar to the isothermal models because the ellipticity profile is really similar (figure 4.13).
In all models we measure an increasing value of the ellipticity in the region of $R \sim 0.1\, r_{500}$ consistent with the effect of the rotation pattern imposed. The results of the ellipticity are presented in table (4.4). We measure mean values that are comparable with previous work ($\epsilon \sim 0.18$, Vikhlinin et al. 2009).

4.4.4 Cool Core Rotating Models

The considerations about these cool core models are equivalent to the ones that we have already exposed for non-isothermal models (figure 4.14). We report the mean ellipticity in table (4.5).

The effect of rotation is particularly important in the increasing of the flattening of the isophotes.

model	$< \epsilon_{obl} >$	$< \epsilon_{pro} >$
CCVP1	0.14 ± 0.016	0.16 ± 0.019
CCVP2A	0.15 ± 0.016	0.16 ± 0.02
CCVP2B	0.16 ± 0.019	0.14 ± 0.02

Table 4.5: Mean ellipticity value for the rotating cool core models.

4.5 Photometric Results

Here we summarize the results of the comparison between the observational points and the ellipticity measurements and the surface brightness profiles that we made on our models. The surface brightness maps, for the rotating models, suffer from the shape of the velocity profiles creating a distortion of the brightness distribution in the inner radii (below ~ 150 kpc) that is only dependent on the choice of r_0 of the velocity profile.
The ellipticity measurements are comparable, inside the errors and fluctuations that are evident in the evaluation method (see in details section 4.1.1), with the observational values. This is a strong proof of the goodness and reliability of our models.

- The surface brightness maps of the non rotating models are useful to see the effect of the gravitational potential and how the gas is stratified. For the rotating models it is interesting to study how the velocity profiles modify the distribution creating a peculiar peak in the maps in the region of $R \sim 150$ kpc.
- The surface brightness profile, that was analyzed both along R and z, show that generally the non-rotating models have a higher surface brightness value than the rotating ones. For the prolate models we do not see high discrepancies along R and z profiles in all models.
- The flattened gravitational potential that we made gives an initial flattening of the gas distribution that leads to an isophotal flattening observable in X-ray measurements. Under the right choice of selection for the region to extract the ellipticity we do not measure great differences between the oblate or prolate non-rotating models and between the different physical assumptions (isothermal, non-isothermal and cool core). We measure a mean ellipticity value for all models of $< \epsilon > \sim 0.14$ that is lower than what was found in Lau et al. (2012) ($< \epsilon > \sim 0.25$) but is comparable with what was found in Vikhlinin et al. (2009) ($< \epsilon > \sim 0.18$).

- For rotating oblate models we need a lower velocity at the peak of the profile, below 1000 km/s (see table (4.1)), than what was found in Bianconi et al. (2013) to achieve ellipticity profiles comparable to those of observed clusters. The computed mean ellipticity is higher than what was found for the non-rotating models and the cool core models show an even higher value ($< \epsilon > \sim 0.15$ for the isothermal and non isothermal while $< \epsilon > \sim 0.18$ for the cool core) that is comparable with the previous results from Vikhlinin et al. (2009).

- For rotating prolate models we found that a higher velocity profile is needed, of the order of 2400 km/s (see table 4.1), to have our measurements comparable with the real observations. Like was already found for the oblate models, the differences between the different physical models are almost negligible.
  For the prolate models the mean value is lower for the cool core model

($< \epsilon >\sim 0.15$) than in the oblate cool cores but it is higher for the non-isothermal models ($< \epsilon >\sim 0.17$). All of them are still comparable with the observational data and with previous works (Vikhlinin et al. 2009).

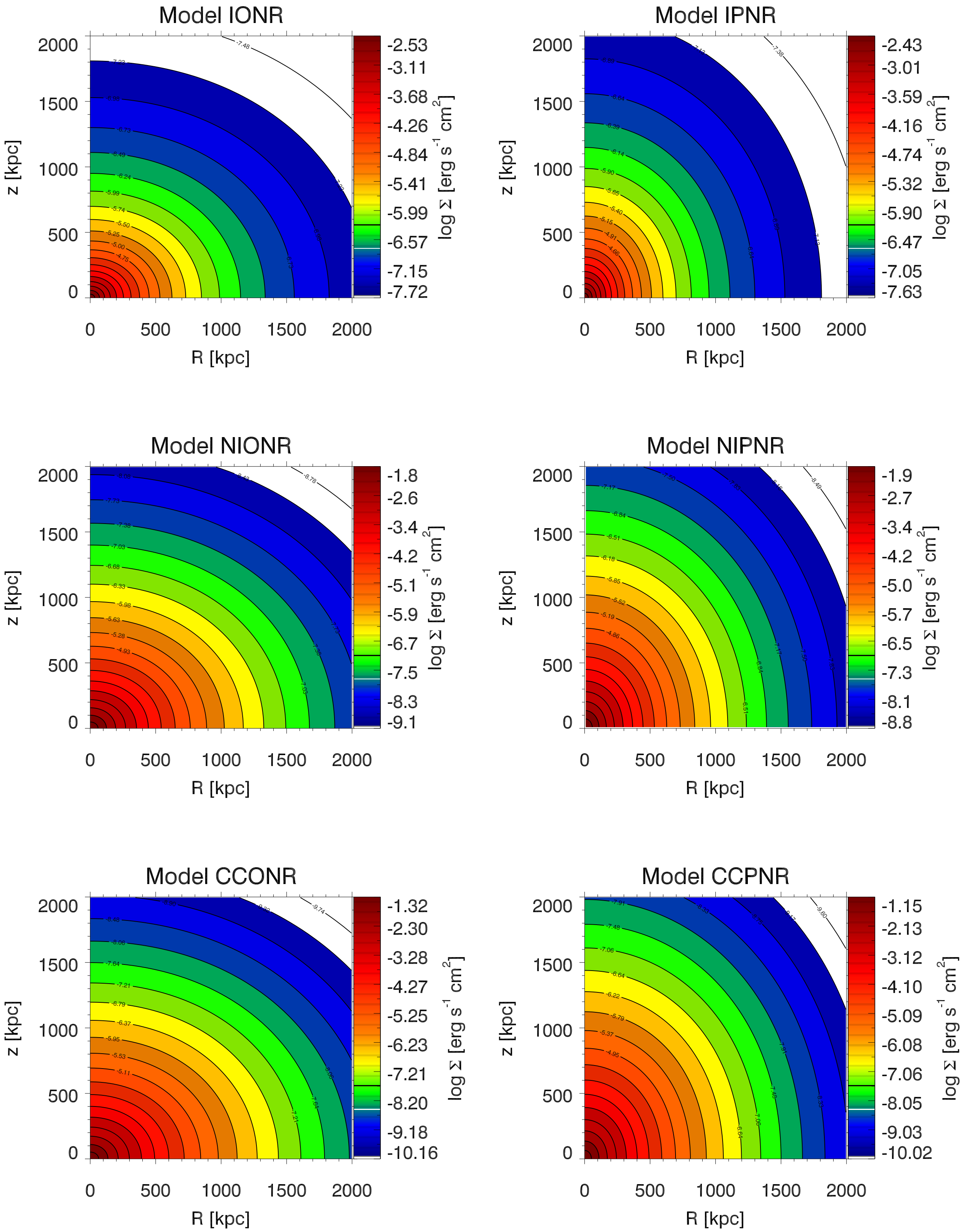

Figure 4.5: Surface brightness maps of the non-rotating oblate model (left) and prolate (right). Top isothermal models, middle non-isothermal and bottom cool core. The parameters are shown in table (3.1).

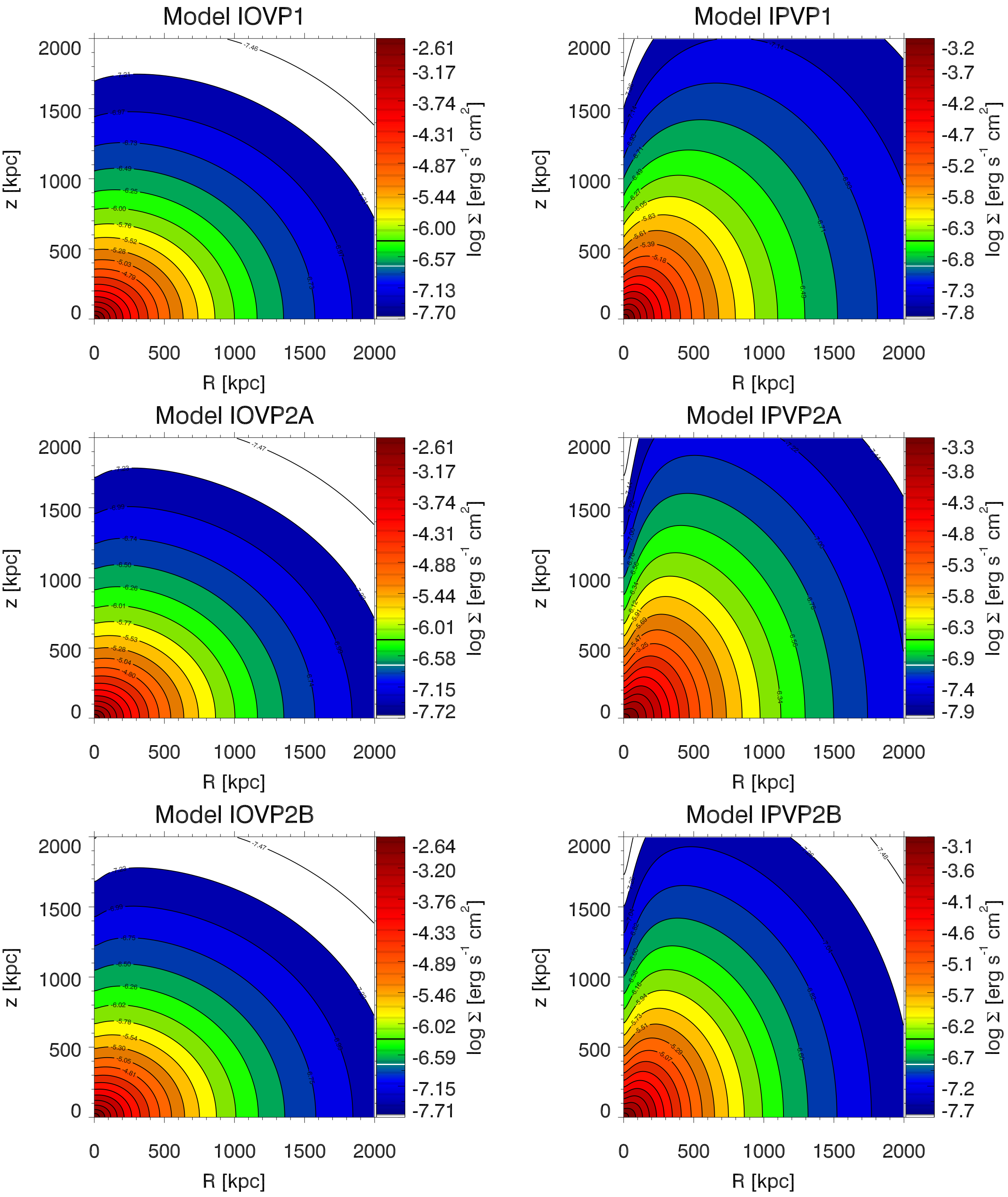

Figure 4.6: Surface brightness maps of the isothermal rotating oblate models (left) and prolate (right). In this graphs we have at the top the model with VP1, at the middle the models with VP2A and at the bottom the VP2B models.

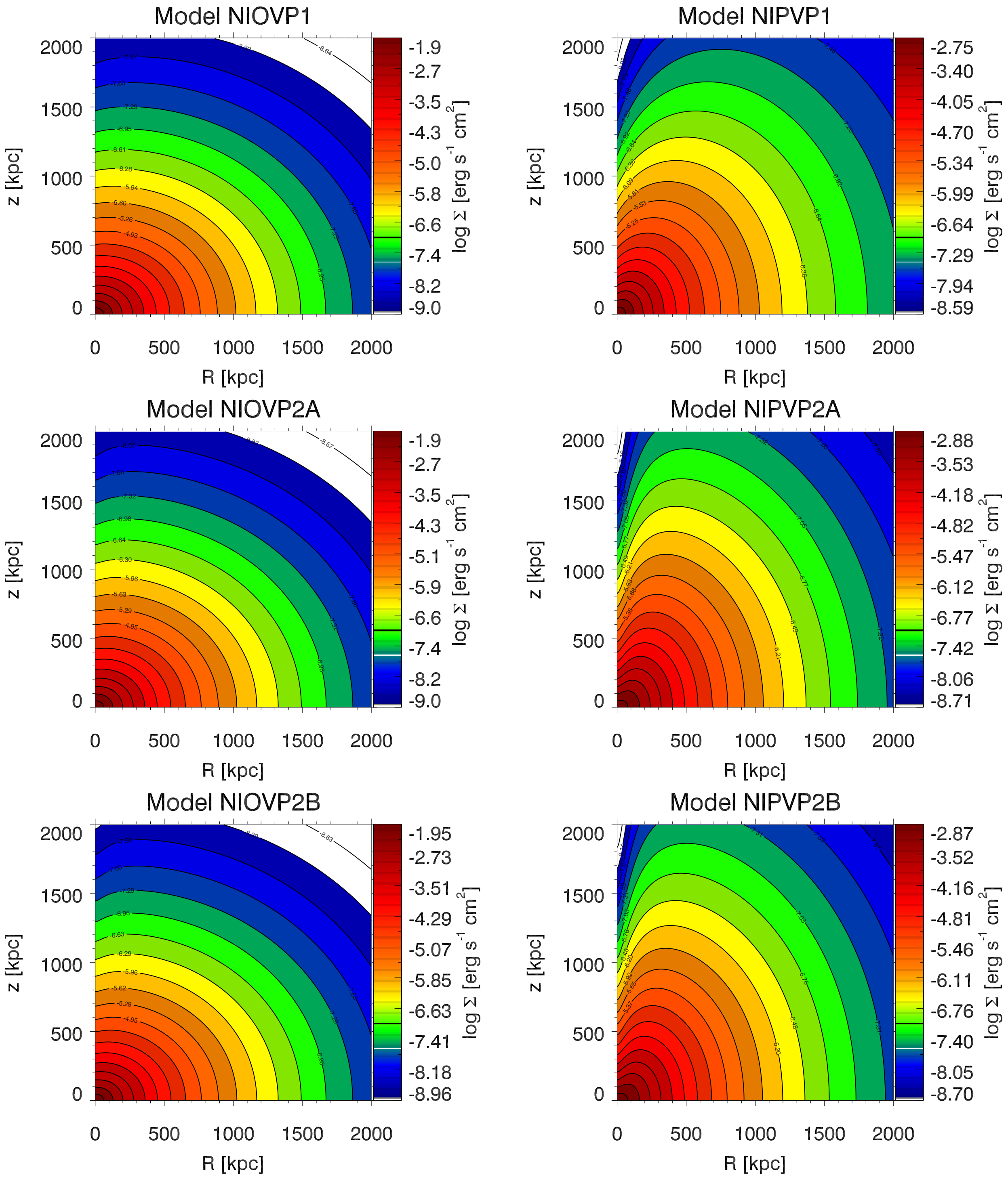

Figure 4.7: Surface brightness maps of the non-isothermal rotating oblate models (left) and prolate (right). In this graphs we have at the top the model with VP1, at the middle the models with VP2A and at the bottom the VP2B models.

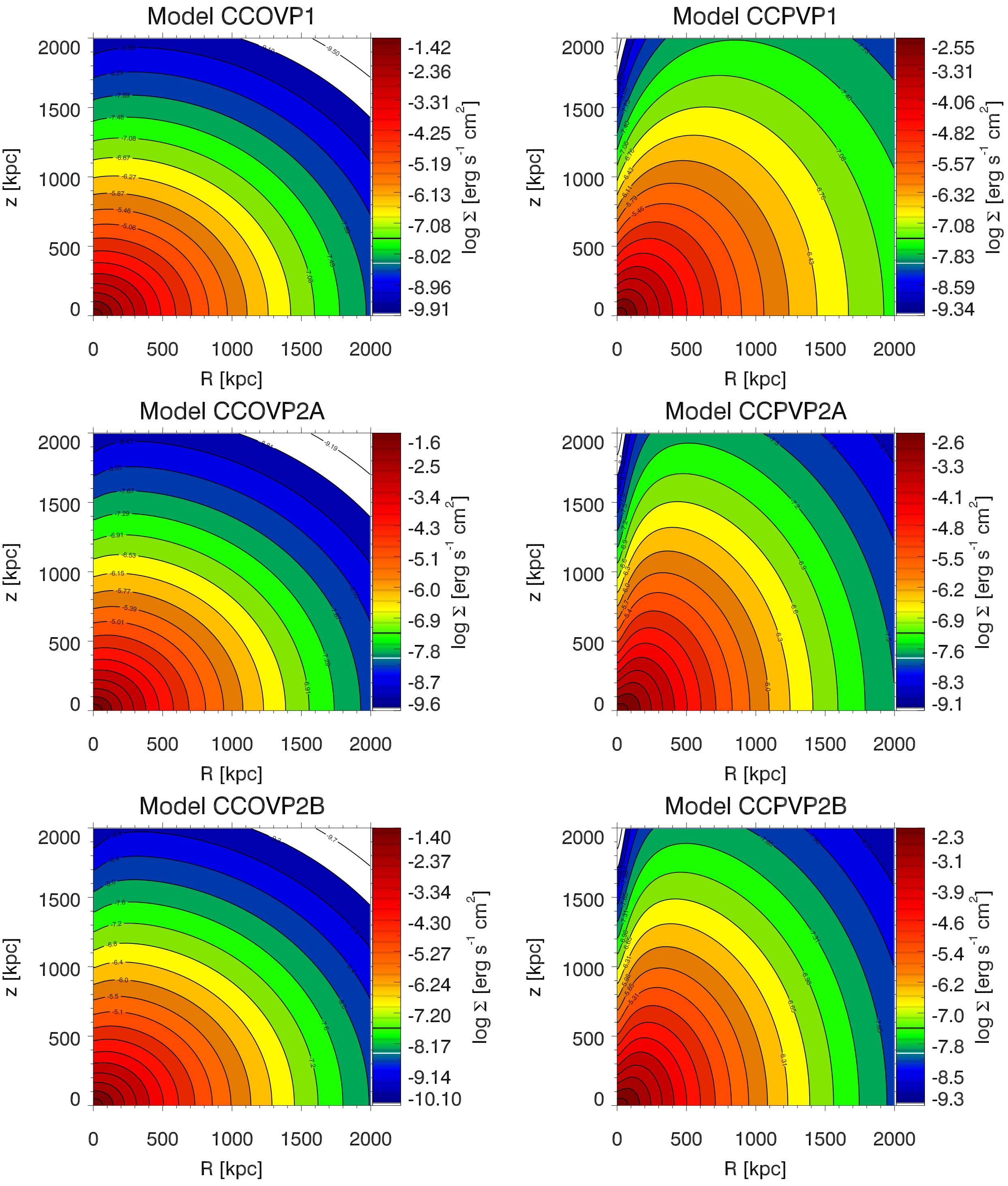

Figure 4.8: Surface brightness maps of the cool core rotating oblate models (left) and prolate (right). In this graphs we have at the top the model with VP1, at the middle the models with VP2A and at the bottom the VP2B models .

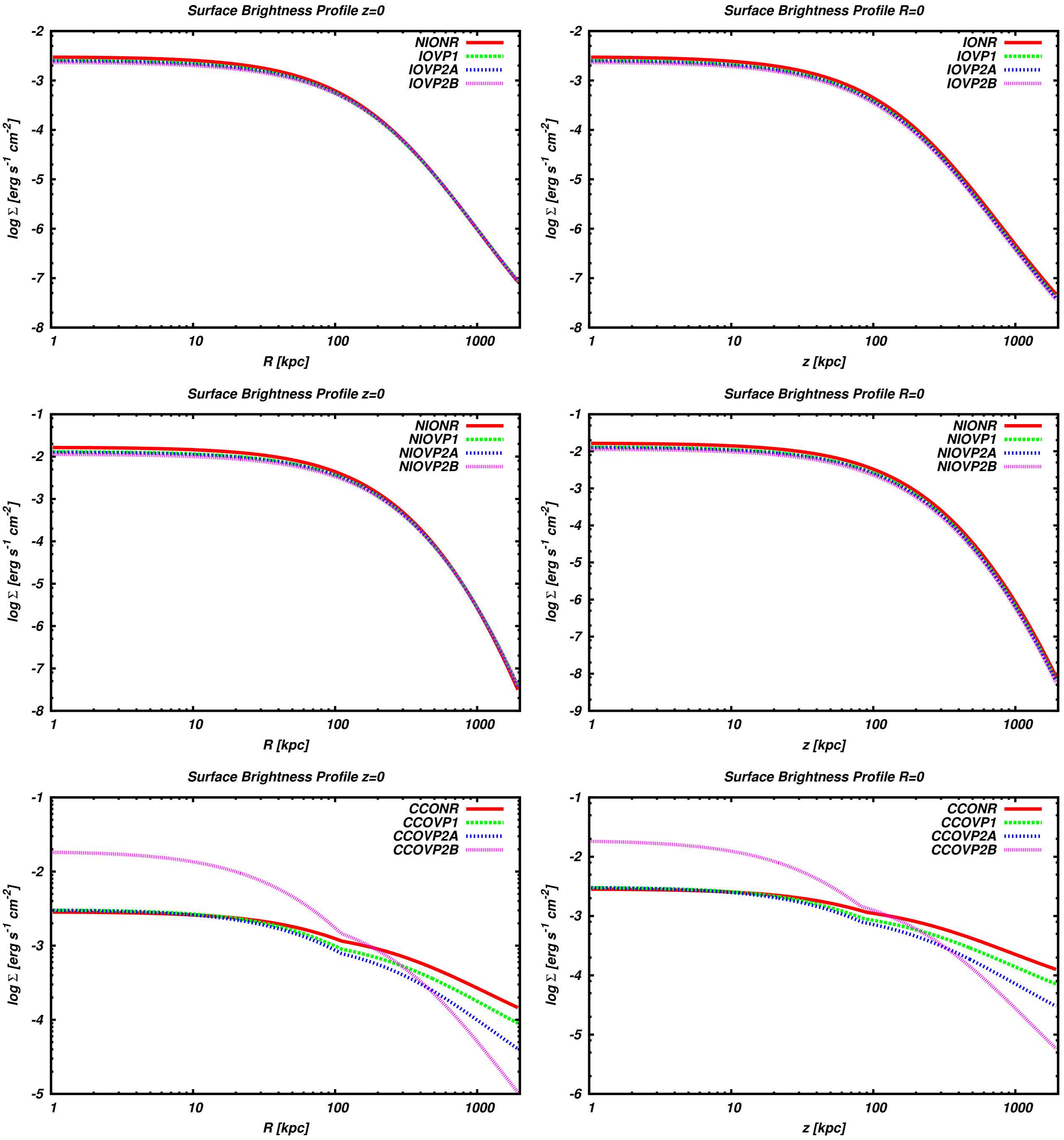

Figure 4.9: Surface brightness profile for isothermal (top), non-isothermal (mid), cool core (bottom) oblate models along R (left) and z (right)

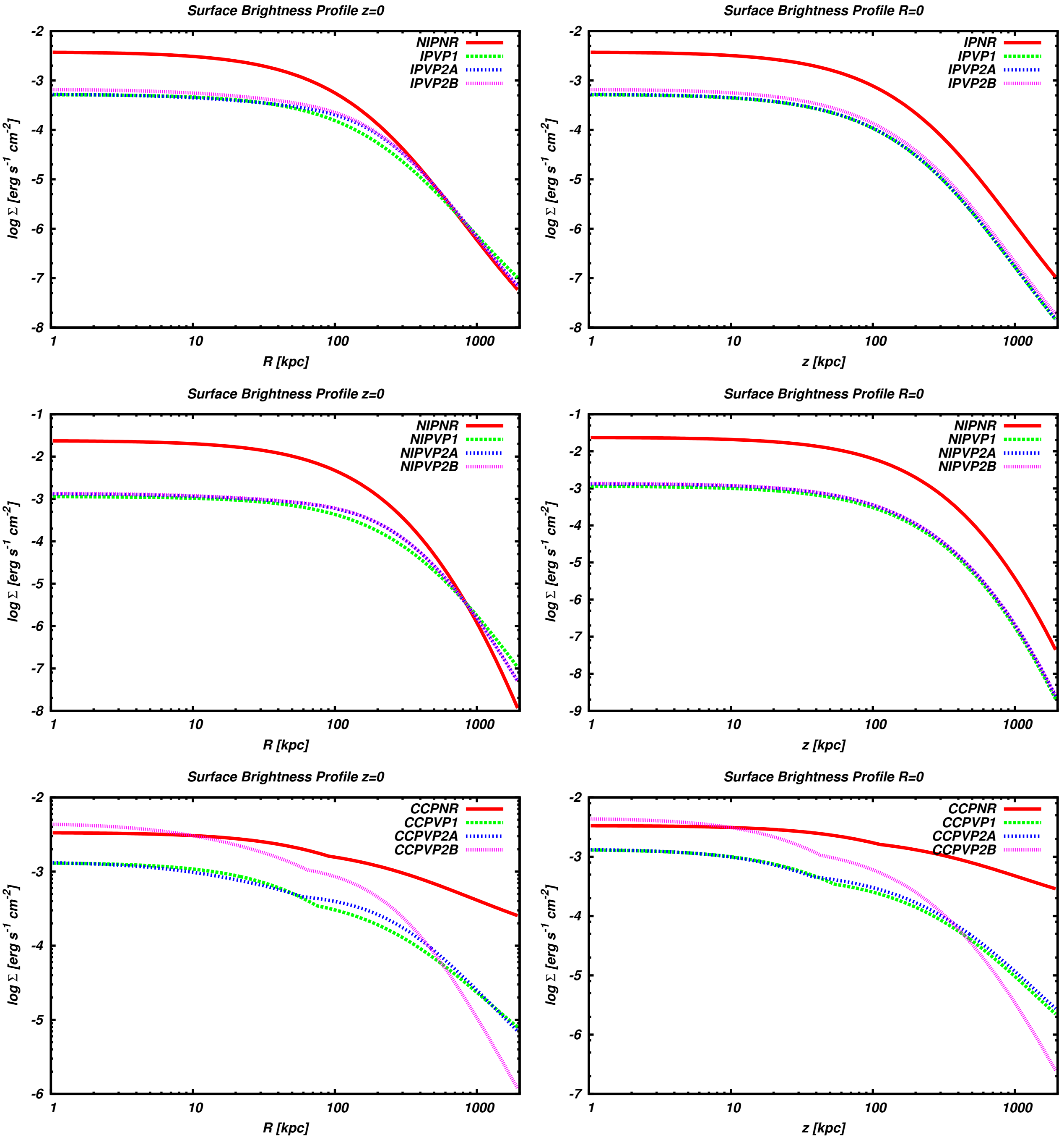

Figure 4.10: Surface brightness profile for isothermal (top), non-isothermal (middle), cool core (bottom) prolate models along R (left) and z (right)

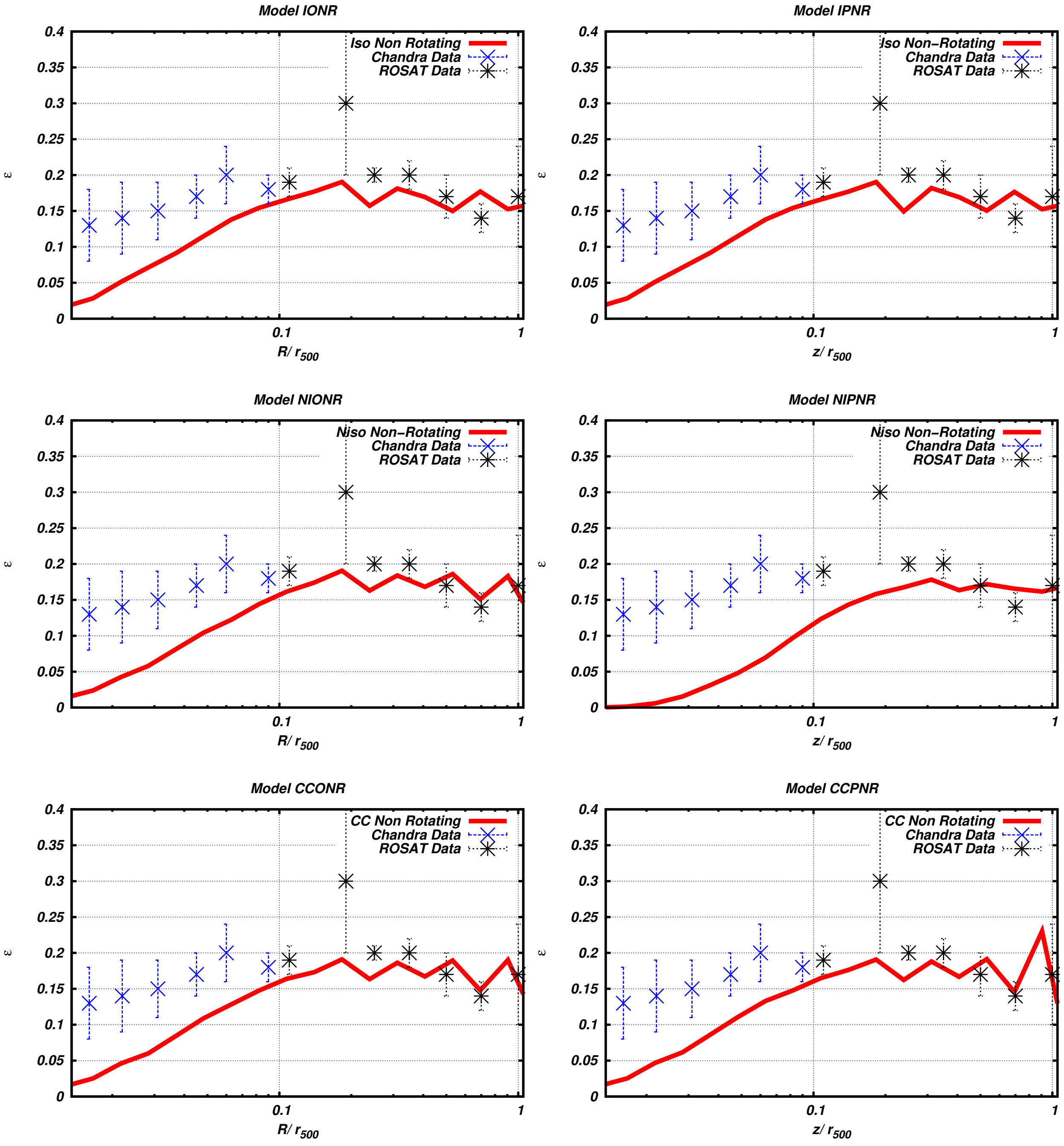

Figure 4.11: Ellipticity profile of the isothermal (top), non-isothermal (mid) and cool core (bottom) non rotating oblate (left) and prolate (right) models in order of r_{500} and with observational points of Chandra and Rosat from Lau et al. (2012).

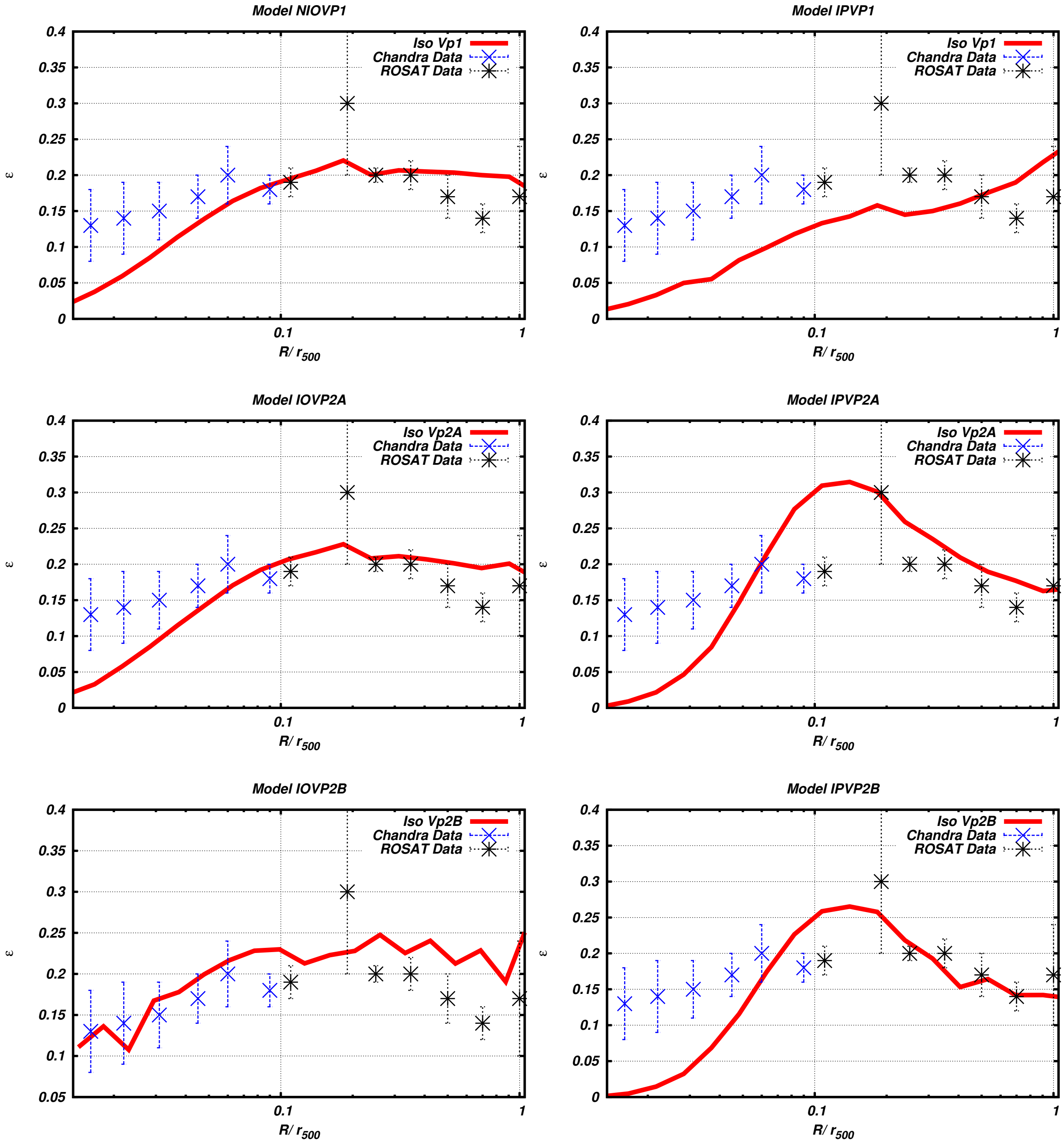

Figure 4.12: Ellipticity profile of the isothermal VP1 (top), VP2A (mid) and VP2B (bottom) non rotating oblate (left) and prolate (right) models in order of r_{500} and with observational points of Chandra and Rosat from Lau et al. (2012).

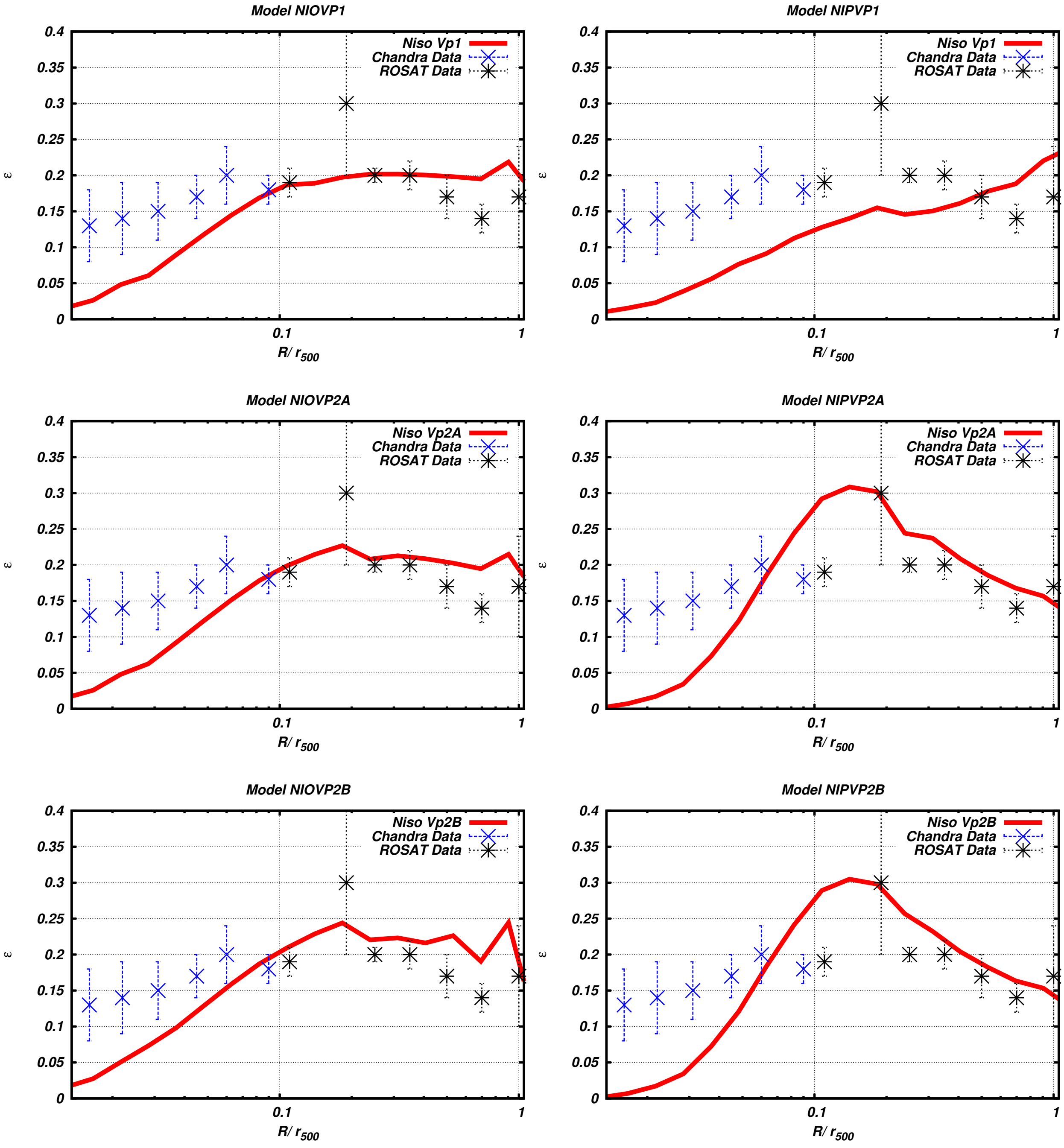

Figure 4.13: Ellipticity profile of the non-isothermal VP1 (top), VP2A (mid) and VP2B (bottom) non rotating oblate (left) and prolate (right) models in order of r_{500} and with observational points of Chandra and Rosat from Lau et al. (2012).

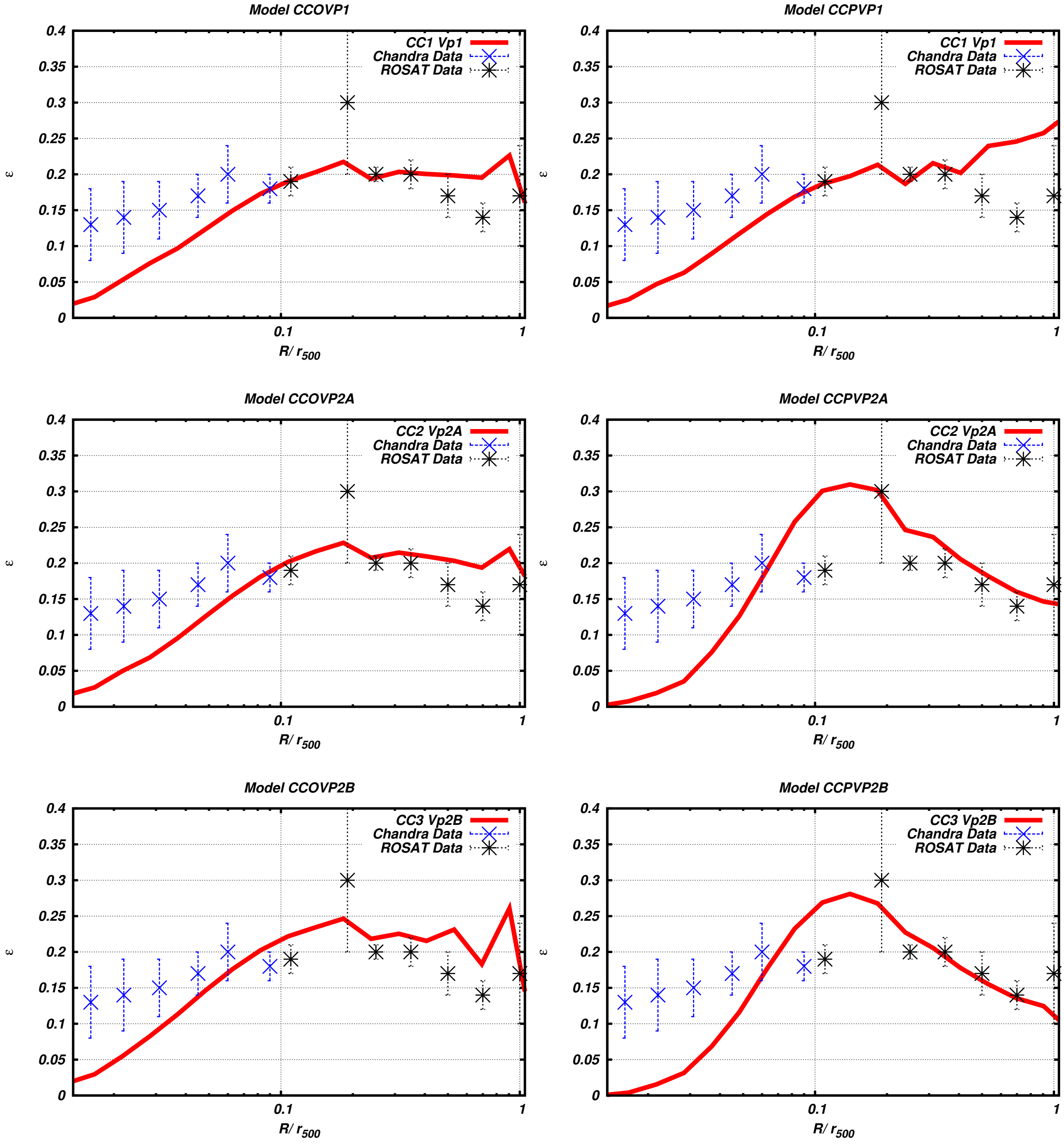

Figure 4.14: Ellipticity profile of the cool core VP1 (top), VP2A (mid) and VP2B (bottom) non rotating oblate (left) and prolate (right) models in order of r_{500} and with observational points of Chandra and Rosat from Lau et al. (2012).

Chapter 5

X-Ray Spectroscopy

In this last chapter, we want to analyze mock observations of our cluster models to obtain a perspective of what will be available with `ATHENA`. We use the specifics of the high resolution microcalorimeter that will be on board of the next big project in X-ray astronomy regarding ESA, `ATHENA`.

5.1 ATHENA Instruments

The Advanced Telescope for High-ENergy Astrophysics (`ATHENA`) is the European future for X-ray observations after the mission of `XMM-Newton` (XMM). This satellite is scheduled to be launched in L_2 [1] in 2028 and it has many scientific scopes like the search and census of supermassive black holes (SMBH) and map the structures of the X-ray emitting gas in galaxy clusters (information from http://www.the-athena-x-ray-observatory.eu/).

The telescope will have a 12 meters focal length and an effective area of about $15000\ cm^2$ at 1 keV and the main instruments on board will be a Wide Field Imager (WFI) that will be used for imaging and high-time resolution of bright sources and the X-ray Integral Field Unit (X-IFU) that will be a high-resolution cryogenic microcalorimeter fundamental for high quality spectroscopy.

Another characteristic feature of the X-IFU will be the big hexagonal pointing field of view (FOV) with a diameter of approximately 5 arcmin in the energy range $0.2 - 12$ keV. The high-resolution spectroscopy is a fundamental goal for galaxy cluster astrophysics because it will confirm and test many aspects of gas motion, for example, the effect of turbulence, the interplay between AGN[2] feedback and turbulence, the formation of radio halos and mini-halos due to energetic loss of the turbulence. In our study, the possibility of having such good energy resolution will allow the analysis of the rotation pattern of the ICM and the coherent motion of the gas in clusters.

Summary technical characteristics of the `ATHENA` telescope:

---

[1] L_2 is the Lagrangian point in the Three Body Sistem Sun-Earth-Moon it is a gravitational unstable region due to the gravitational field produced by these three objects, in fact the motion of the satellite, in this case, is fundamental to correct the orbit and contrast the effect of the gravitational instability. In that gravitational point will be set the James Webb Space telescope (the successor of Hubble Space Telescope) and Euclid Space Telescope (EUCLID).

[2] Active Galactic Nuclei

Instrument	**WFI**	**X-IFU**
Detector type	Si APS (DEPFET)	Micro-calorimeter/TES
Operating temperature	210 K	50 mK
Detector size (mm)	102.4×102.4	31.2×31.2
Energy range (keV)	$0.2 - 15$	$0.2 - 12$
Energy resolution ($FWHM$)	70 eV @ 1 keV	2.5 eV $<$ 7 keV
Field of view ($arcmim$)	$40'$	$5'$

Table 5.1: Main technical parameters of ATHENA from the site of ESA, under the assuption of circular FOV. In table is reported the diameter of the FOV in arcmin.

5.2 X-Ray Observations

X-ray spectroscopy is a tool for understanding the physics that rules the emission from intracluster plasma. The high temperature of the gas ionizes most of the chemical species present and the emission line spectrum is characterized by the presence of the Fe XXV (6.7 keV, also called *He-like iron lines*) and Fe XXVI (6.9 keV) emission lines. Typical emission of 6.7 keV is fundamental to obtain information about redshift (so we can obtain the distance of the cluster) and the inner motion of the gas that generates a Doppler shift of the studied line. We are interested in studying the effects of the gas motion on both the centroid shift (e.g. Liu et al. 2015, Liu et al. 2016) and the broadening (e.g. Inogamov and Sunyaev 2003) of the emission lines associated to the ionized metals of the ICM. In the next section (5.3), we analyze the Doppler shift of the 6.7 keV line for rotating models with different rotation laws comparing the observed results with the theoretical prediction. In section (5.4) we analyze the effect of the line broadening due to the velocity dispersion in the line of sight and the centroid shift.

5.3 Mock Spectra

We analyze the mock spectra created with XSPEC (Arnaud 1996), using models that reproduce the free-free continuum emission and line emission of the elements typical of astrophysical plasma: `apec` and `bapec`. The `apec`[3] model reproduces the emission spectrum from collisionally-ionized diffuse gas based only on temperature, metallicity and redshift. The `bapec` [4] model, instead, reproduces a velocity and thermally-broadened emission spectrum from collisionally-ionized diffuse gas. In figure (5.1) we show the theoretical `apec` and `bapec` spectra of a 6 keV thermal plasma with 0.3 solar metallicity at a 0.1 redshift observed with the X-IFU calorimeter in a 100 ksec of observation. In the right figure, the `bapec` spectra, is evident the broadening of the 6.7 keV line imposed to the model ($\sim$ 150 km/s). This mock data are convolved with the spectral response of the detector and with the absorption of the column density of hydrogen of our galaxy and without considering the background contribution.

---

[3] https://heasarc.gsfc.nasa.gov/xanadu/xspec/manual/XSmodelApec.html

[4] https://heasarc.gsfc.nasa.gov/xanadu/xspec/manual/XSmodelBapec.html

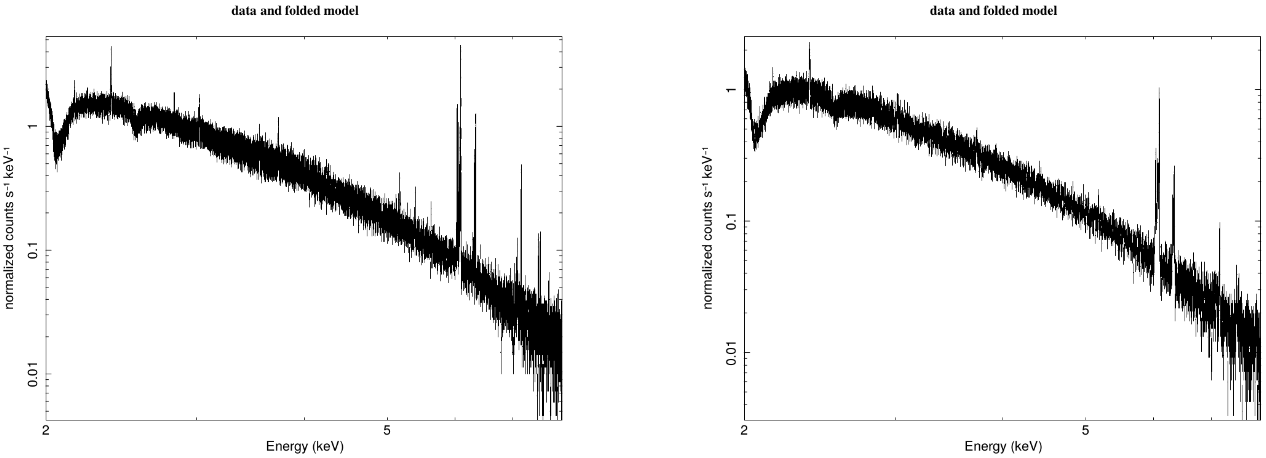

Figure 5.1: Simulated spectrum of the `apec` model (left) and `bapec` (right) with 100 ksec between 2 and 7 keV.

We consider our cluster at a redshift of 0.1, with a 1.68 ratio between arcseconds and kpc. We consider five circular regions in the median plane of the cluster with radius of 15 arcsec (25 kpc), 30 arcsec (53 kpc), 59 arcsec (100 kpc), 1.18 arcmin (127 kpc) and 2.01 arcmin (210 kpc) and located at 200, 500, 700, 1100 and 1600 kpc from the cluster's center. We selected these regions with those extensions to collect a good number of source counts (between 5000 and 10000) with a typical X-IFU exposure of 100 ksec. We divided our regions in 32, 25, 22, 17 and 10 cylindrical blocks assuming that in every single box there is a constant density, constant temperature and gas velocity. We considered separately the blue-shifted (approaching) regions (denoted as B) and red-shifted (receding) regions (denoted as R) to account for the different response of the models at various energies. We projected the density onto the sky plane in order to obtain the normalization constant for the models. Then, we evaluate the line-of-sight component of the rotational velocity, being this the factor responsible of the Doppler shift of the emission line centre. For the fit we added a component of interstellar medium absorption of our galaxy due to the column density of hydrogen in the line-of-sight fixed at a value of 0.05×10^{22} atoms per cm^2 using the model `tbabs`[5].

In the tables we report the values used to fit the models and the results at 3σ for every model and every region where we calculated the Doppler shift.

For the fitting parameters we adopted the emission-weighted value of the temperature (5.1) and for the velocity (5.2) in the centre of the cylindrical block:

$$T_{EW} = \frac{\int n_e T_i dV}{\int n_e dV}; \tag{5.1}$$

$$\overline{v}_{EW} = \frac{\int n_e v_i dV}{\int n_e dV}; \tag{5.2}$$

---

[5] https://heasarc.gsfc.nasa.gov/xanadu/xspec/manual/node251.html tbabs

where i identifies the block where the values are calculated and V is the volume of the cylindrical block.

The velocity pattern of the gas motion make the 6.7 keV line (fluorescent He-like iron line) shift like there is a blue-redshift effect and thanks to the energy resolution of 2.5 eV, achievable with ATHENA, this could be detected.

$$\frac{\Delta E}{E} = \frac{\Delta z}{1+z} = z_{pec} \approx \frac{v}{c}, \tag{5.3}$$

$$\frac{2.5\,eV}{6700\,eV} = \frac{\Delta z}{1+0.1} \Rightarrow \Delta z = \frac{1.1 \times 2.5\,eV}{6700\,eV} \approx 4 \times 10^{-4}. \tag{5.4}$$

In equation (5.4) we present the maximum shift detectable with the energy resolution of ATHENA. Considering that we are interested in the properties 6.7 keV emission line we analyze the simulated spectra between 2 to 7 keV. The best-fit parameters are obtained minimizing the C-Statistic (Cash 1979). We decided to analyze all models for each type of cluster (isothermal, non-isothermal and cool core) and verify if there are differences between the three velocity profiles (VP1, VP2A and VP2B) in the spectroscopic analysis and particularly in the case of VP2A and VP2B where the physical parameters are really similar and the analysis of ellipticity showed almost the same results.

We quote the input parameters of the models and the best-fit values in appendix (B.1). Starting with the oblate isothermal models we explore the fitting parameters and their errors with a confidence of $3\,\sigma$. For every model and region we used the metal abundance set to $0.3\ Z_{\odot}$ but we do not report this value in table.

The fit response of the models is always comparable with the parameters that we imposed within the statistical uncertainties that are always present. The results obtained for the regions at 1100 and 1600 kpc are the most inaccurate ones because of the low flux associated with these regions, but they are still consistent with the input parameters. We reproduce the Doppler shift diagrams showing the theoretical deviations of the shift and the observed shift of our models. We expect that going from the region at 200 kpc to the one at 1600 kpc we should measure a decreasing deviation from 0.1, that is the redshift of the clusters. We expect also that in the study of the shift we can find the velocity profile that we imposed at our gas. In the figures (5.2, 5.3, 5.4) we show the Doppler shift obtained with the mock observations compared with the theoretical behaviour of the shift for each model at different distance from the cluster's centre.

We start showing the oblate models that have a less important rotation, due to their flatter potential, and it made the Doppler shift less important than what we can spot in the prolate models. We present coupled oblate and prolate models with the same velocity profiles in order to show how much the rotation velocity affects the shifts.

We can say that the higher velocity of the prolate models tends to have a major effect in the shift of the lines, reaching a $\Delta z \sim 2 \times 10^{-3}$, especially in the inner regions (1,2 and 3). We can see also that the line shift of the various models strongly depends on the shape of the velocity profile in fact, as you can see for example in figure (5.2, top), the VP1 (2.49) shows a flatter trend in all radii and it is obtained by the centroid shift measurement.

For the outer regions (4,5) sometimes the low statistic, caused by the low surface brightness, creates higher fluctuations of the parameters of the fit.
We find that for the oblate models we have an energy shift ΔE of ~ 4 eV for the VP1 and about 5 eV for the VP2 (A and B) for the inner regions (1,2 and 3) while the regions 4 and 5 present a lower shift in the order of ~ 2 eV that is the limit of energy resolution of X-IFU. While for the prolate models we find a mean ΔE between 14 and 15 eV for the innermost regions and an energy shift for the outer regions consistent with $3 \sim 4$ eV.
As shown in figure (5.1), the Doppler shift of the Fe line can be resolved significantly from Athena-XIFU, allowing to constrain the velocity profile of the ICM.

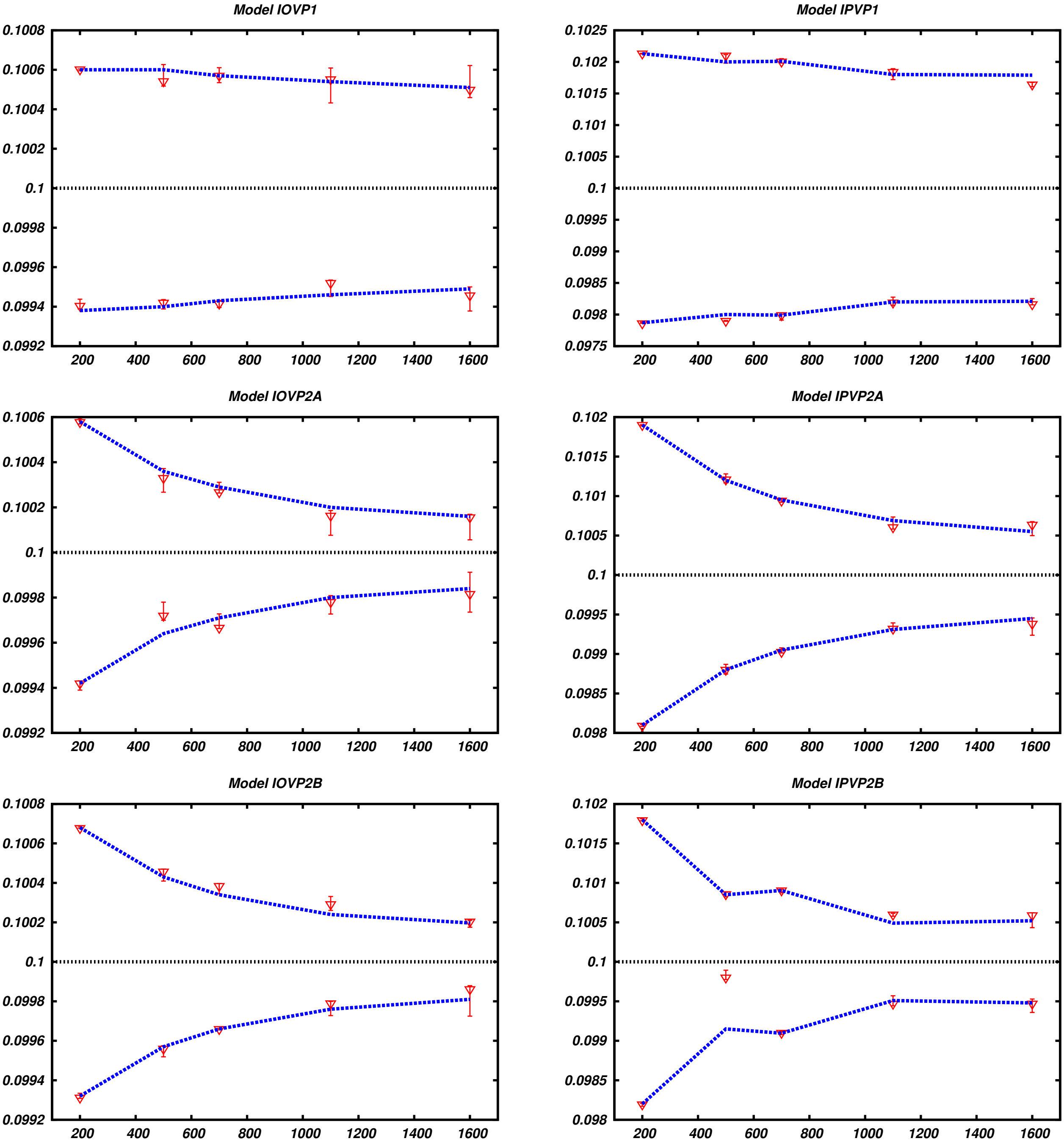

Figure 5.2: Doppler shift diagrams for the isothermal oblate (left) and prolate (right) models. The tables with the results of the fit are B.1-B.10 (Top), B.2-B.11 (middle) and B.3-B.12 (bottom). The blue lines are the expected values from the models while the red points are the results of the fit. The black line at 0.1 is the redshift of the cluster. We remind that the errors are at a level of confidence of 3σ.

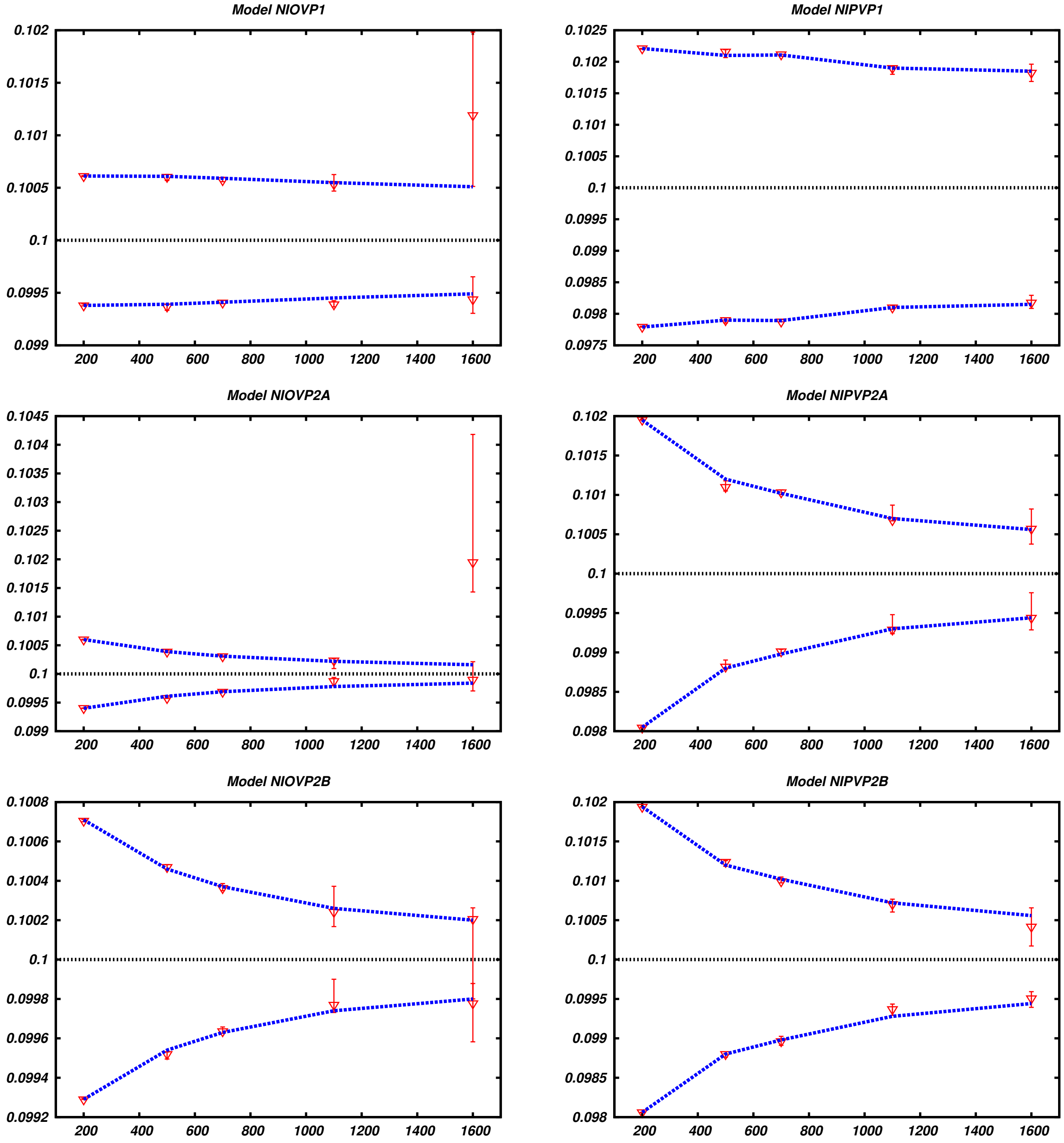

Figure 5.3: Doppler shift diagrams for the non-isothermal oblate (left) and prolate (right) models. The tables with the results of the fit are B.4-B.13 (Top), B.5-B.14 (middle) and B.6-B.15 (bottom). The blue lines are the expected values from the models while the red points are the results of the fit. The black line at 0.1 is the redshift of the cluster We remind that the errors are at a level of confidence of 3σ.

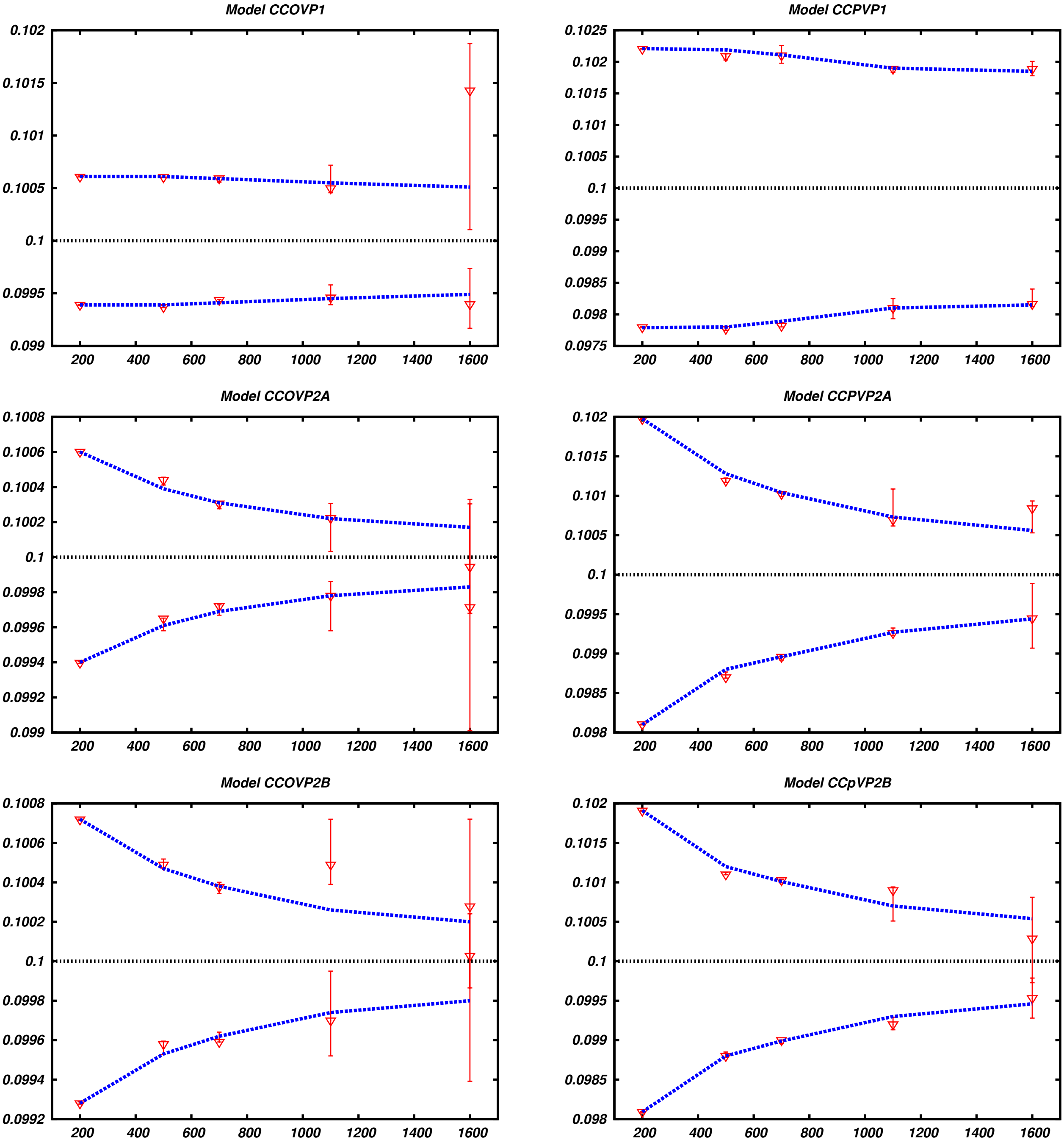

Figure 5.4: Doppler shift diagrams for the cool core oblate (left) and prolate (right) models. The tables with the results of the fit are B.7-B.16 (Top), B.8-B.17 (middle) and B.9-B.18 (bottom). The blue lines are the expected values from the models while the red points are the results of the fit. The black line at 0.1 is the redshift of the cluster We remind that the errors are at a level of confidence of 3σ.

5.4 BAPEC Model Fitting

After the analysis of the pure centroid shift of the lines in the section (5.3) we want to study the effect of the velocity dispersion of the gas in the line of sight. To estimate this parameter we studied how much the velocity changes in the direction on the line-of-sight and at different radii of the cluster.

Like was done in the previous study we selected the same five regions with the same extensions. We studied the broadening using the `bapec` model of `Xspec` analysis tool inserting the same physical parameters of the `apec` modelling and adding the emission-weighted velocity dispersion (5.5) of the lines due to the gas motion.

$$\sigma^2_{EW} = \frac{\int n_e (v_i - \overline{v})^2 dV}{\int n_e dV}. \tag{5.5}$$

The $\overline{v}$ is the averaged velocity in the cylinder. In appendix (C.1) we show the parameters fitted with `Xspec` with a confidence of 3σ. We report the normalization parameter[6] (N) in the order of $[10^{-4}]$, like was already done in the `apec` fit, but here it is not reported in the tables. The abundance is set for all models to $0.3\,Z_\odot$ and we report only the results of the fit.

We present the results of the Doppler shifts and the broadening profiles. We start presenting the broadening profiles where we compare the measured broadening with the expected value from the models.

After having presented all Doppler shifts and broadening profiles we can say that, differently from the `apec` models we find that the broadening alters the measurement of the shifts, in fact we have fluctuations in all models in the order of 10^{-4} that are consistent with the magnitude order of the correction of the centroid shift.

We can say that all models in the Doppler shift present a good fit with the predictions of the models, excluding the measurements of the last points (regions 4 and 5) that are affected by the low normalization of the models like was already evident in the `apec` results.

Like was already evident in the Doppler shift analysis of the `apec` fits the shape of the velocity profiles are obtained back from the observations in both broadening and shifts profiles.

The VP1 profile, like what was found in the previous section, is almost flat and especially for the oblate models with a lower rotation velocity the broadening is really small, lower than 150 km/s. For the prolate models instead we can reach a broadening of over 1000 km/s in the inner regions (1 and 2) due to the high velocity peak and to the steep velocity profile.

For the first velocity profile we are aware that the fluctuations of the values are bigger than the other profiles and the profile itself is not always well reproduced by the observed measurements.

---

[6] The normalization parameter of the `apec` and `bapec` is defined as:

$$N = \frac{10^{-14}}{4\pi[D_A(1+z)]^2} \int n_e n_H dV \tag{5.6}$$

where D_A is the diameter angular distance to the source (cm),z is the redshift of the source, dV is the cylindrical volume (in our case) and n_e and n_H are the densities of electrons and H (cm^{-3}).

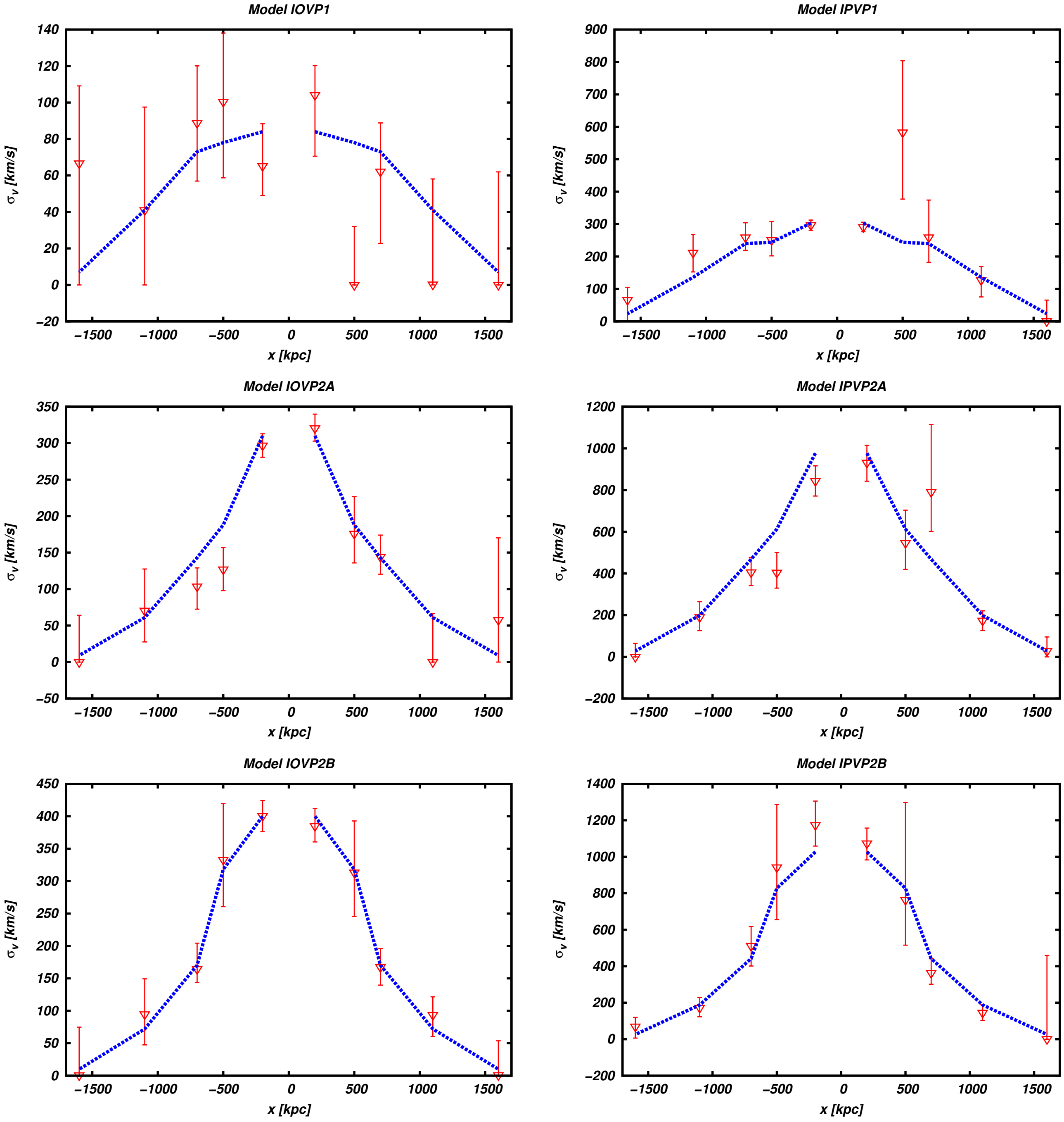

Figure 5.5: Broadening profiles of the isothermal oblate (left) and prolate (right) models in the order of VP1 (top, table of values C.1-C.10), VP2A (middle, table of values C.2-C.11) and VP2B (bottom, table of values C.3-C.12). The lines are the expected values obtained from the models while the red points are the values from the fit with error of 3σ.

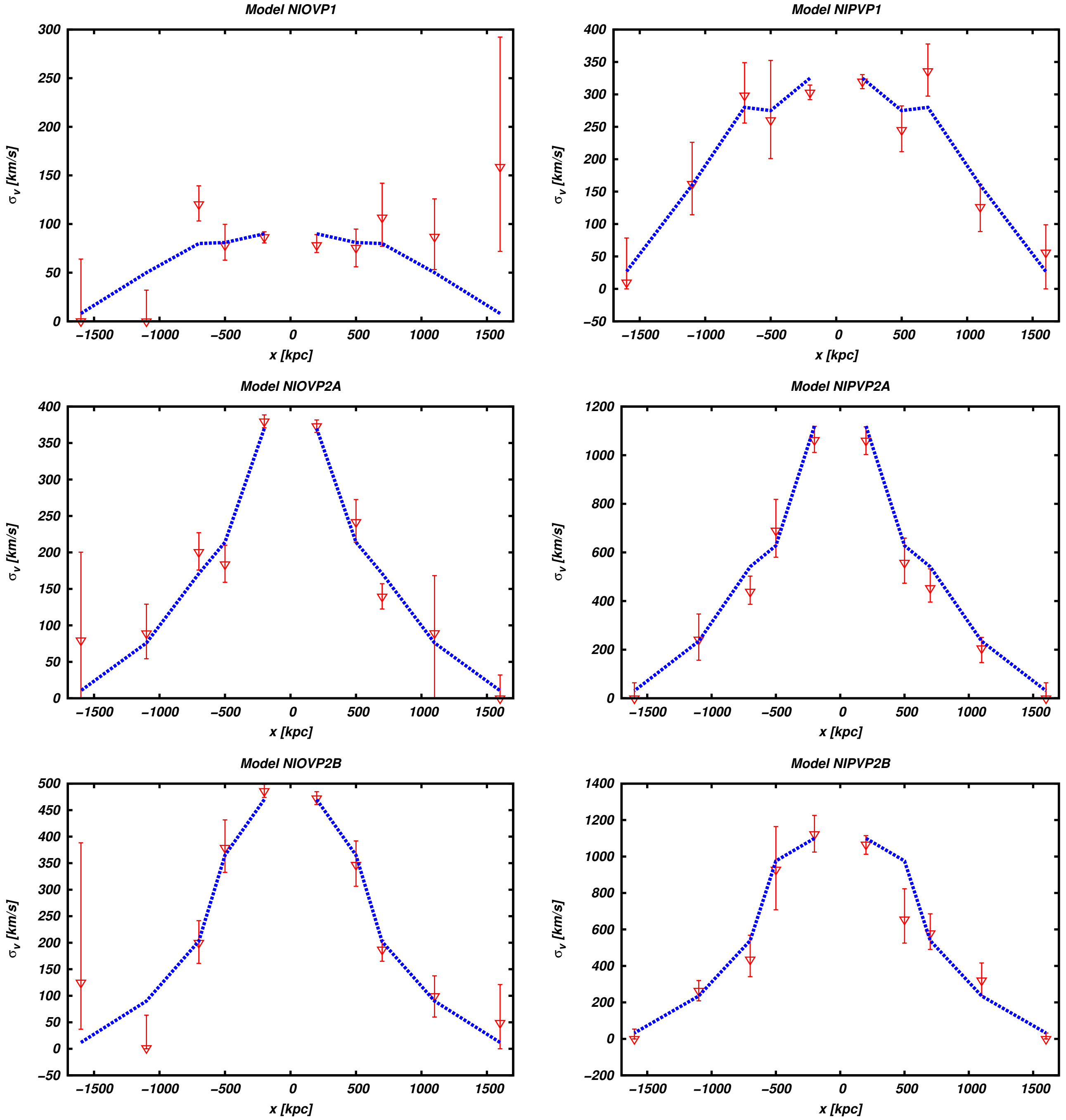

Figure 5.6: Broadening profiles of the non-isothermal oblate (left) and prolate (right) models in the order of VP1 (top, table of values C.4-C.13), VP2A (middle, table of values C.5-C.14) and VP2B (bottom, table of values C.6-C.15). The lines are the expected values obtained from the models while the red points are the values from the fit with error of 3σ.

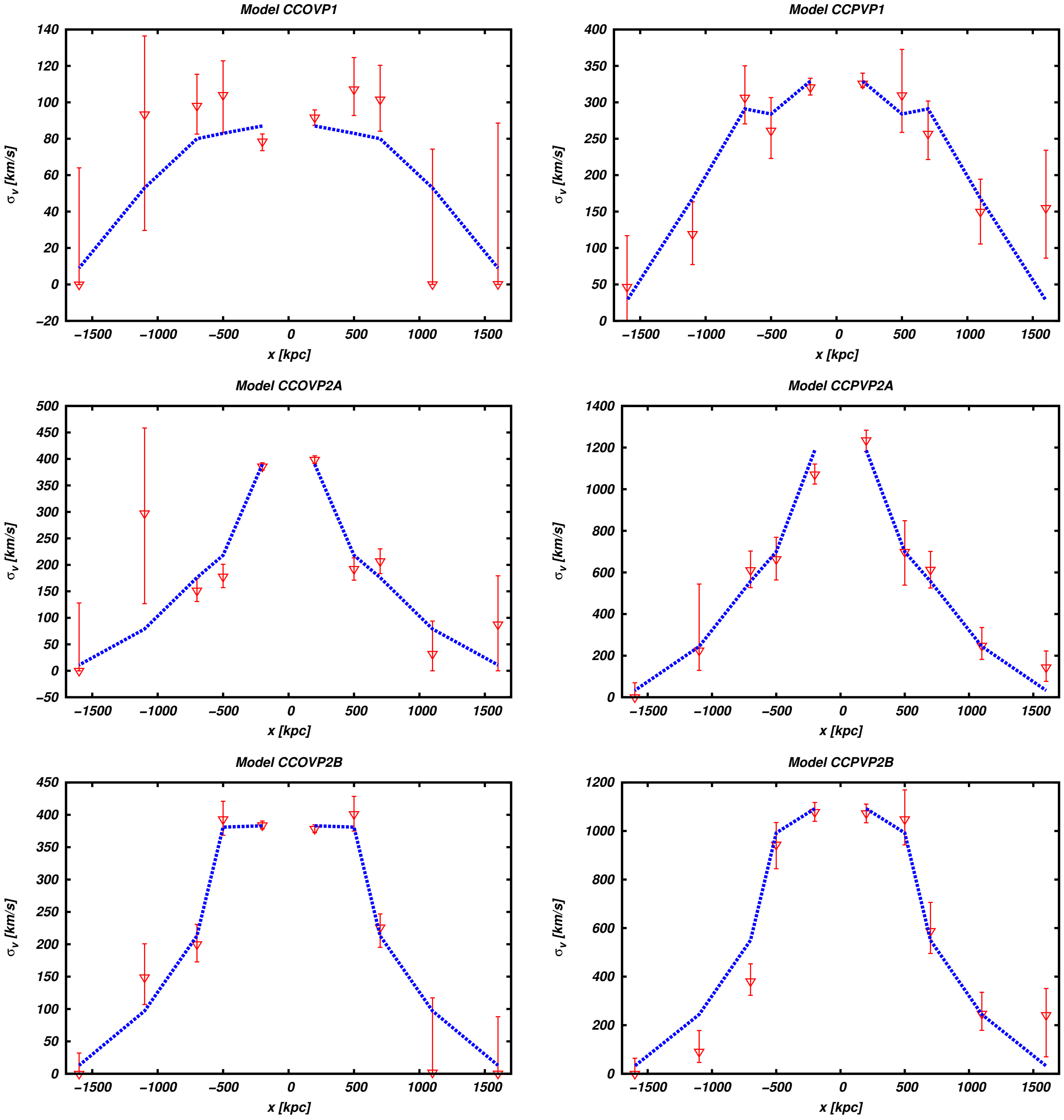

Figure 5.7: Broadening profiles of the cool core oblate (left) and prolate (right) models in the order of VP1 (top, table of values C.7-C.16), VP2A (middle, table of values C.8-C.17) and VP2B (bottom, table of values C.9-C.18). The lines are the expected values obtained from the models while the red points are the values from the fit with error of 3σ.

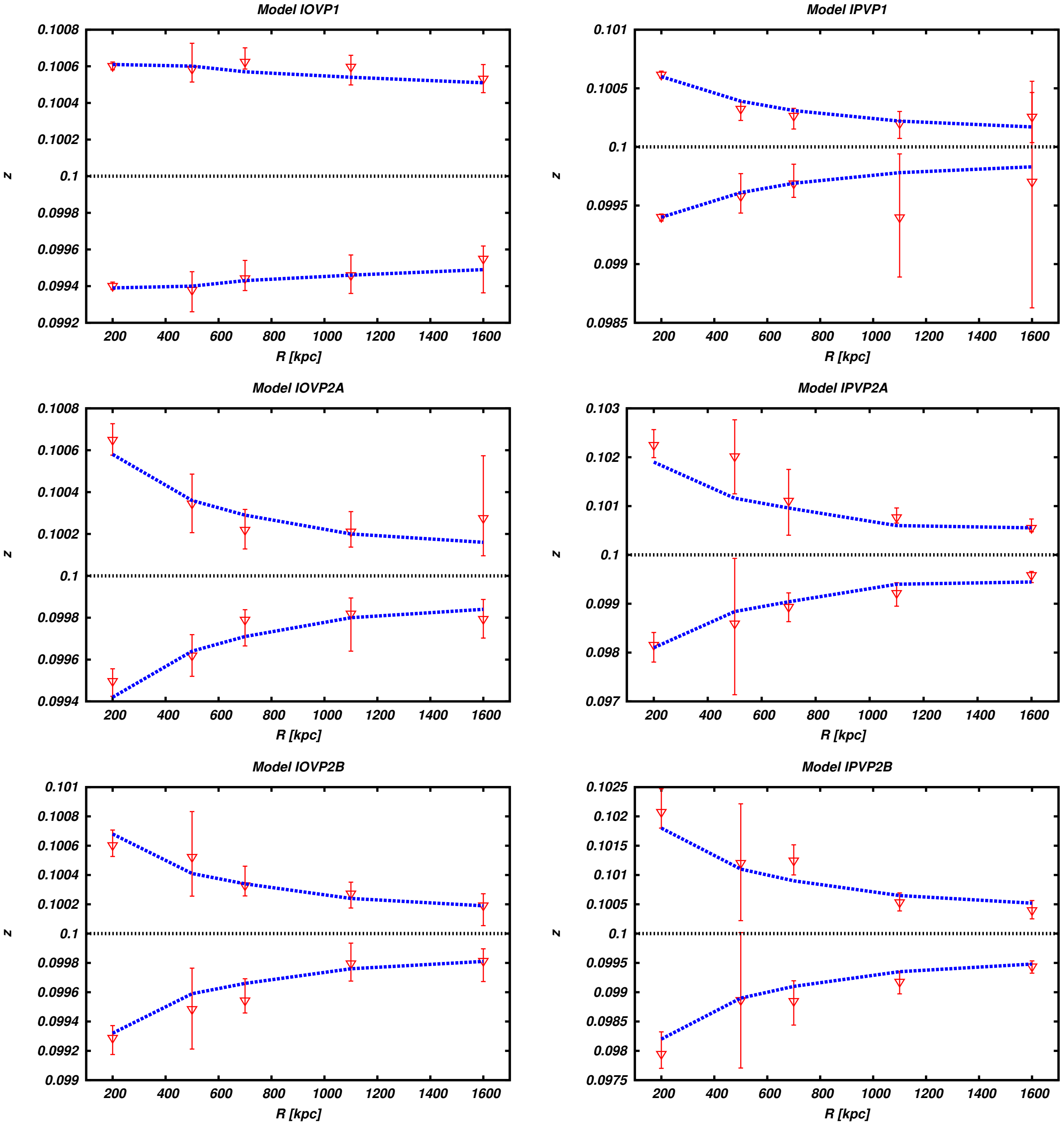

Figure 5.8: Doppler shift of the isothermal oblate (left) and prolate (right) models in the order of VP1 (top, table of values C.1-C.10), VP2A (middle, table of values C.2-C.11) and VP2B (bottom, table of values C.3-C.12). The lines are the expected values obtained from the models while the red points are the values from the fit with error of 3σ.

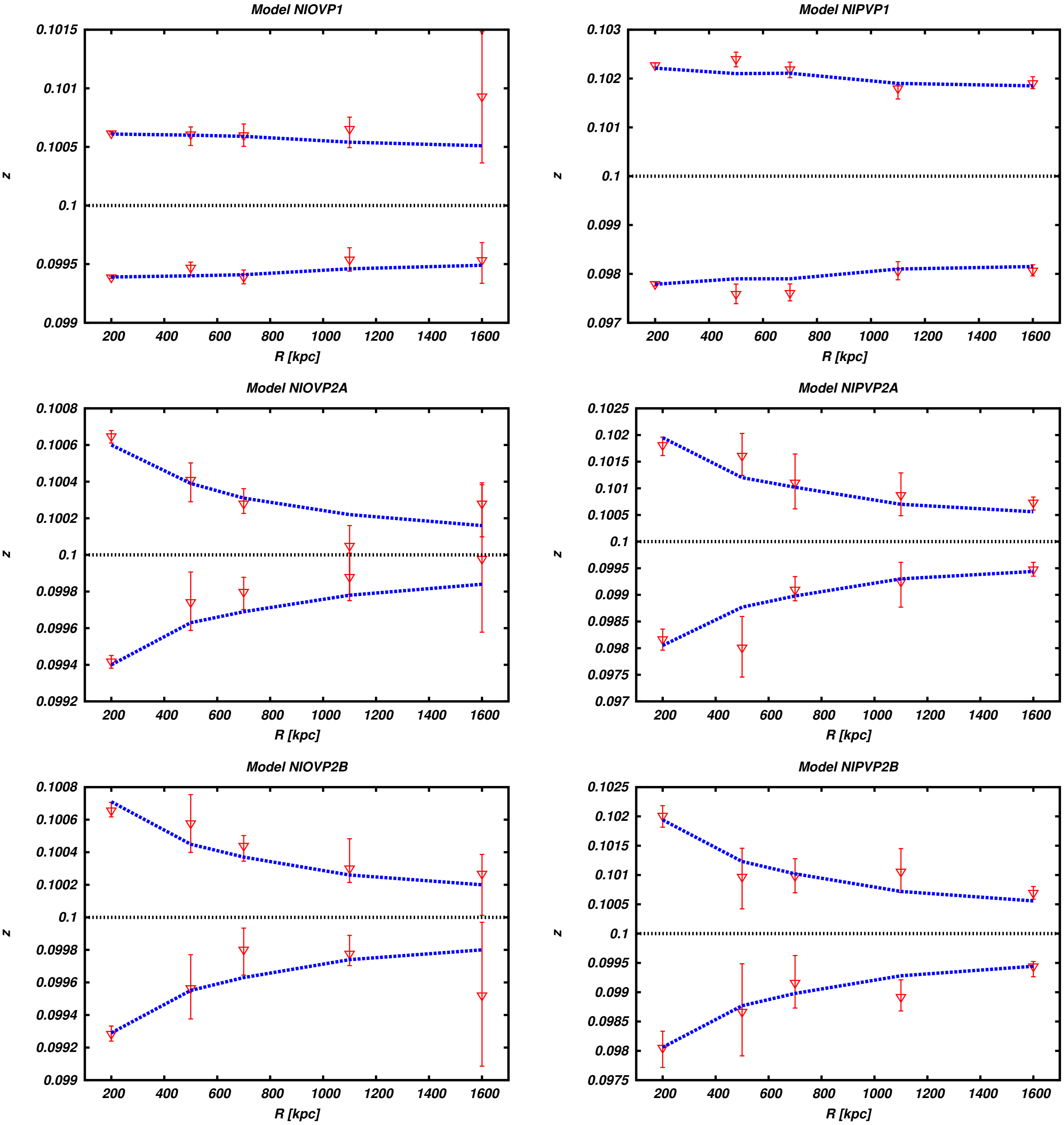

Figure 5.9: Doppler shift of the non isothermal oblate (left) and prolate (right) models in the order of VP1 (top, table of values C.4-C.13), VP2A (middle, table of values C.5-C.14) and VP2B (bottom, table of values C.6-C.15). The lines are the expected values obtained from the models while the red points are the values from the fit with error of 3σ.

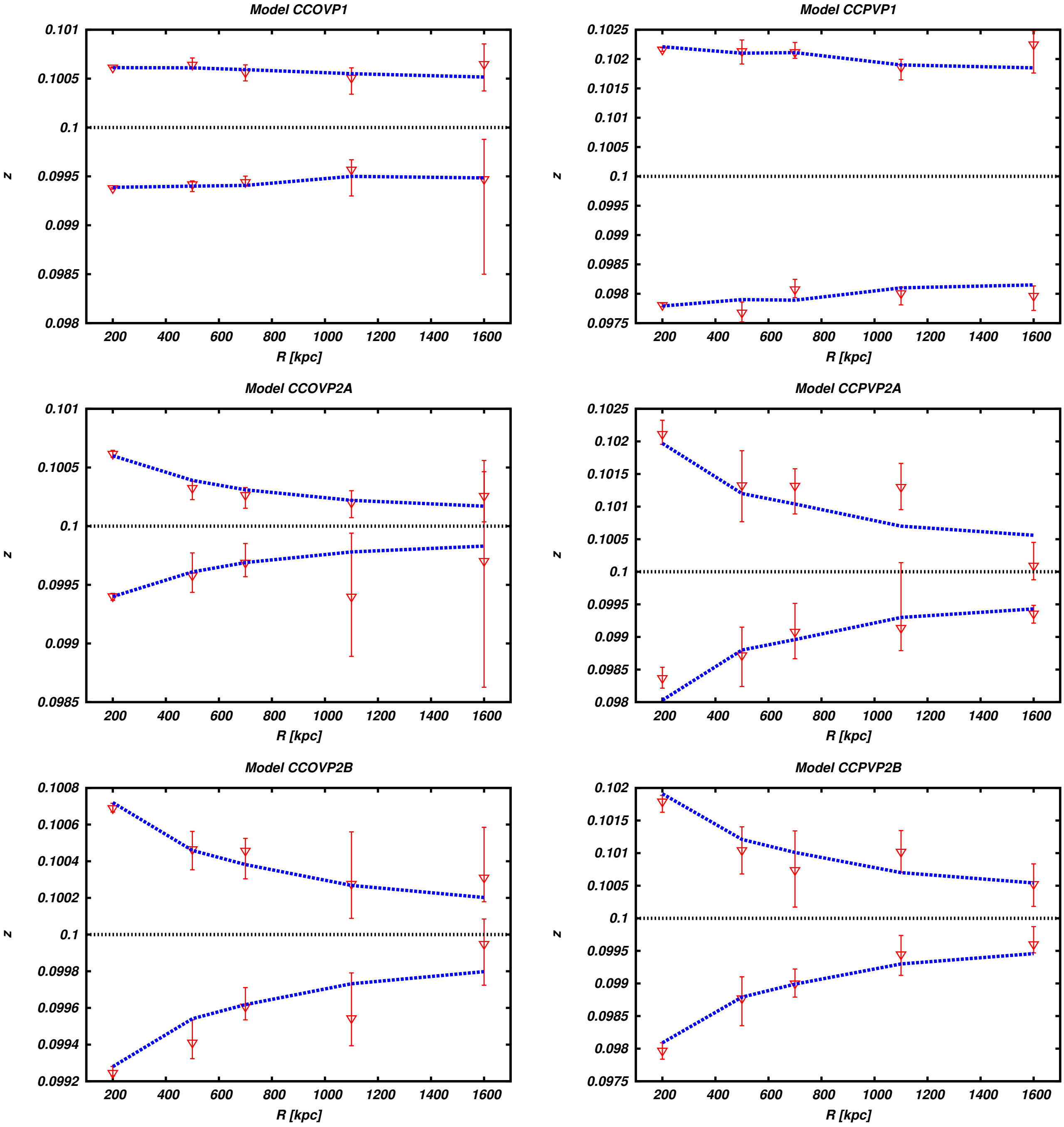

Figure 5.10: Doppler shift of the cool core oblate (left) and prolate (right) models in the order of VP1 (top, table of values C.7-C.16), VP2A (middle, table of values C.8-C.17) and VP2B (bottom, table of values C.9-C.18). The lines are the expected values obtained from the models while the red points are the values from the fit with error of 3σ.

5.5 Spectroscopic Results

In the last section of this chapter we discuss the main results of the spectroscopic analysis that we performed.
We selected five regions in the median plane of the cluster and with sufficient spatial extension in order to have a good amount of counts, nevertheless we found out that in the outer regions (at 1100 and 1600 kpc) the fit in some models is unstable and the uncertainties are higher. We obtain the following results:

- the velocity creates a centroid shift that is consistent with what is found in the work of Liu et al. 2015, 2016 in the order of few eV. The oblate centroid shifts are lower and in the order of $\Delta E = 4 \sim 6$ eV for the inner regions, denoted as 1-2-3, while in the outer regions (4-5) the energy shift is in the order of $2 \sim 3$ eV just above the limit resolution of X-IFU. While for the prolate models we measure a Doppler shift in the order of $\Delta E = 14 \sim 16\ eV$. Performing the five regions lead us to reproduce the velocity profile toward the radius in a good range of confidence (3σ);

- the analysis with the line broadening along the line of sight gives us another proxy to measure the motion and obtain information on how steep is the velocity profile. We can spot that the models with the velocity profile 1 (VP1) are shallower and almost flat profile both in the Doppler shift diagrams and in broadening profiles. While the VP2 profiles have a more delineated shape verifiable both in Doppler shifts and broadening;

- the steep profile and the high rotation velocity of the VP2 prolate create a line broadening in the order of 1000 km/s that is particularly high but we are aware of the low reliability of this result because it is strongly affected by the choice of the parameters obtained by the ellipticity comparison, see section (4.5).

Chapter 6

Conclusions

6.1 Discussion

We built models of gas in motion in flattened axisymmetric potential. The dark matter halos that we built are comparable to the real observed halos. Our dark matter halos are not extreme cases, those could have an axial ratio of $0.3 \sim 0.4$ with correspondent flattening of $0.7 \sim 0.6$. In our cases the axial ratio is 0.6 with a ellipticity of ~ 0.4. The flattening of isophotes is directly connected with the shape of the gravitational potential but the presence of baryonic matter tends to reduce the flattening as observed in simulations and observations (Bryan et al. 2013; Kazantzidis et al. 2004). Thus our halo models should be realistic representation of halos expected in ΛCDM.
The rotation has a direct impact on the distribution of the gas modifying the effect of potential. The velocity parameters that we adopted in the work aimed to reproduce the observed isophotal flattening from the work of Lau et al. (2012).
Last but not least, the spectroscopic results are a good test for the possibilities available with `ATHENA`. The low Doppler shift of the oblate models could be considered as lower limit test for the energy resolution of the instruments. The big field of view of the X-IFU could permit also high quality observations even in the range of low surface brightness, like the case of the regions above r_{500}.
In the next subsections we briefly discuss the main results of the work.

6.1.1 Photometric Results

In the various models we studied, one of the main comparable observable is the flattening of the isophotes that can be considered as direct evaluation of the shape of the dark matter halo at least for non-rotating models. The method to evaluate the ellipticity was based on the selection of elliptic coronae and computing the inertia moments of the surface brightness in that region (see in detail section 4.1.1). Thanks to this method we could study the models and make comparison between the models and the observative data to understand which model fits better.

- For non rotating models we obtain a mean ellipticity through the full dimension of the cluster that is lower but comparable to the observed values. This is due to the flattening of the potential that tends to modify and flatten the gas density distribution and consequently the surface brightness distribution.

- For rotating models we differ oblate from prolate case. The oblate case needed a lower velocity support, with a maximum of ~ 1000 km/s for reproducing the observed flattening. The prolate case instead needed a higher velocity component above 2400 km/s. All models fit the observed data at larger radii than $0.1\ r_{500}$. At inner radii we find a lower ellipticity and this can be associated with different causes, for instance the way we compute the inertia moments, that in the innermost regions may affect the evaluation. Other possible explanation of this bad sampling can be associated with the way we characterize the physical parameters in the inner regions where the isophotes may be less flattened than what we find in outer radii. The shape of the gas distribution and surface brightness is strongly connected with the shape of the rotation profile imposed. The drop of the surface brightness in the innermost part, below 300 kpc, that is evident in all models, especially in prolate models, is a direct consequence with the shape of the velocity profile. This feature is not observed in real observations and may be corrected with presence of low-scale turbulence and with a rotation profile that is not so strongly dependent on the radius.

- The surface brightness profiles of all rotating models do not show many differences (under 10% for the rotating models, higher than 20% comparing rotating to the non-rotating case) because the choice of reproducing a fixed gas fraction lead the models to have a similar gas density in the innermost grid points and consequently all models have almost the same values, see table (3.1).

6.1.2 X-ray Spectroscopic Results

The goal of 2.5 eV for X-IFU calorimeter is a big challenge for X-ray astrophysics and our models could be considered as good tests for the calorimeter. The oblate models in fact, have an energy shift of 5 eV that is enough to provide a good measurements of the shift. We performed measurements in multiple regions in order to test also, under the assumption of a standard observation of 100 ksec, the great field of view and the possibility to obtain good amount of counts even in low brightness regime, as can be considered the region in the proximity of r_{500}. The choice of reproducing the gas motion both receding and approaching was made to test at different energy range the models' response. We summarize some of the most interesting results of the spectroscopic analysis:

- for the oblate models, due to their low rotation velocity (as we already discussed in section 6.1.1), we measure a low shift of the lines and, especially for the outer regions mainly due to the low normalization, we find big fluctuations of temperature and metallicity from the fitting parameters value.

- For the prolate models the high rotation velocity produced a sensible centroid shift of the lines, of the order of 15 eV and the higher normalization parameters tends to minimize the parameters fluctuations making the analysis more stable.

- The choice of performing 5 regions at different radii of the cluster let us determine not only the shift evolution in radius but also shape of the velocity profile of the gas that could be used to discriminate one model from the other.

- Analyzing the line broadening in the line of sight we can understand the velocity of the models and the impact of the velocity in the characterization of the rotation profiles. Another compelling aspect that was interesting to analyze is the combined effect of the Doppler shift and the broadening of the line. In fact the presence of the broadening made the evaluation of the Doppler shift less accurate than in the case without broadening, see section (5.5) for details.

6.2 Future Work

This is only the starting point of the modelling of gas rotation in deep potential wells. One of the first upgrades that could be done is adding a turbulence influence (e.g. Brunetti and Jones 2014, Ettori 2014) in the pressure of the gas that could change some features in the surface brightness and in X-ray spectroscopic observations.
The turbulence will affect the broadening of the lines of the ICM and may affect the measurements of the Doppler shift of Fe lines.
The resolution of some not-observed features that we found in the brightness surface and gas maps is another important step for improving the work that we started. For example a core in the velocity rotation or another shape of velocity rotation, maybe the one presented in equation (2.51) from Baldi et al. 2017, can avoid the formation of the peaked structure in the brightness map that is not observed in real galaxy clusters. Another important step may be the correction of the evaluation of the gas mass inside r_{200} using an ellipsoidal shape correction, this may change the gas fraction and the starting density values that were chosen to reproduce a 0.13 gas fraction.
The ellipticity profiles that we found are in good agreement with the observational data from $0.1\,r_{500}$ and may be a good improvement modelling our models in the innermost parts (under ~ 150 kpc) in order to have a better agreement even at smaller radii.
All these prospects of the work are addressed to characterize the gravitational potential and its influence in the gas equilibrium in order to provide other tools to resolve the hydrostatic bias in numerical simulations and observations.
Finally, it would be useful to compare the ICM shape obtained with high-resolution Sunyaev-Zel'dovich imaging. This is a potentially powerful means

of extending this analysis to higher redshifts, because of the redshift independence of the Sunyaev-Zel'dovich effect.

Appendix A

Appendix

A.1 Grid costruction

In this appendix we show how we built the numerical grid where we costructed our models.
We have chosen a logarthmic grid because we wanted an higher resolution in the inner part of the cluster. In particular, due to the axisymmetry of our models, we constructed our grid in cylindrical coordinates (R,z).
We used 256 (N_{grid}) grid points for each component (R,z) with a integer index i. Under this assumption we obtain a grid of 256×256 points. We determine the grid composition using a logarithmic increment step:

$$X_M = \log_{10}(R_{Max}), \tag{A.1}$$

and

$$X_m = \log_{10}(R_{min}); \tag{A.2}$$

where we used $R_{Max} \equiv 2066$ kpc and $R_{min} \equiv 1$ kpc obtaining $X_M \equiv 3.31$ and $X_m \equiv 0$.
X_m and X_M are needed to determine the grid step:

$$\Delta X = \frac{X_M - X_m}{N_{grid-1}}. \tag{A.3}$$

Thanks to the formulation of ΔX and for $i = 0 \rightarrow N_{grid-1}$ we built:

$$X_i = X_m + i \times \Delta X, \tag{A.4}$$

and:

$$R_i = z_i = 10^{X_i}. \tag{A.5}$$

In figure (A.1) we show the different refinement of the grid due to the logarithmic sampling in the inner part (below ~ 1000 kpc) and in the outer part of the point distribution.

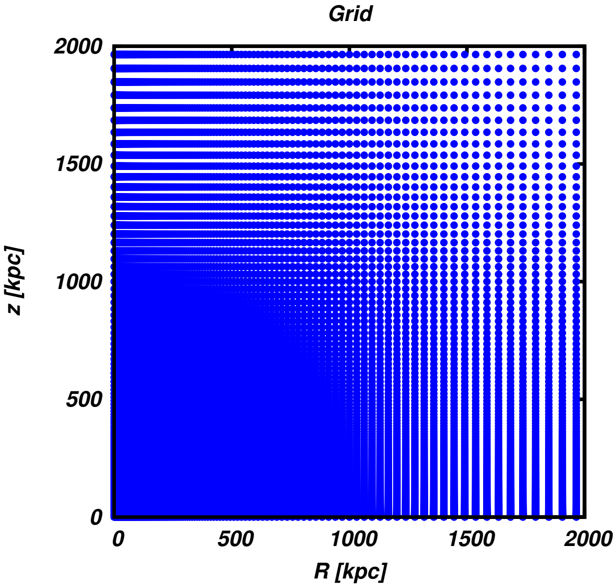

Figure A.1: The grid used in the modelling.

Appendix B

Appendix

In these appendices we report the fitting value and the results of the simulated spectra with the software Xspec through the `apec` and `bapec` models. Galaxy cluster models are studied with a fixed metallicity of $0.3\ Z_{\odot}$ and we estimated the errors with a confidence range of $3\,\sigma$.

B.1 Apec Fitting Parameters

In the `apec` fitting we studied only the centroid shift of the line to evalutate how much the rotation changes the position of centroid of the line. The results of this study are in section (5.3). We report for each region denoted as 1,2,3,4 and 5 in correspondence of the distance of the centre of the cluster (200, 500, 700, 1100, 1600 kpc) and we denote the R the region for the receding motion (redshift) and B for approaching motion (blueshift).

Region	T_{obs} keV	T_{Fit} keV	Z_{obs} $Z_\odot$	z_{obs}	z_{fit}	$N_{0,\,obs}$ $[10^{-4}]\,cm^{-5}$	$N_{0,\,fit}$ $[10^{-4}]\,cm^{-5}$
1R	$7.49^{+0.24}_{-0.18}$	7.5	$0.32^{+0.03}_{-0.02}$	$0.100602^{+1\times10^{-6}}_{-6\times10^{-6}}$	0.1006	$13^{+0.08}_{-0.08}$	13
1B	$7.51^{+0.21}_{-0.21}$	7.5	$0.30^{+0.02}_{-0.01}$	$0.09941^{+3\times10^{-5}}_{-1\times10^{-5}}$	0.0994	$12.7^{+0.1}_{-0.1}$	13
2R	$7.36^{+0.76}_{-0.69}$	7.5	$0.28^{+0.06}_{-0.05}$	$0.10054^{+8.4\times10^{-5}}_{-2.4\times10^{-5}}$	0.10060	$1.72^{+0.03}_{-0.02}$	1.8
2B	$8.31^{+1.09}_{-0.74}$	7.5	$0.31^{+0.07}_{-0.06}$	$0.09942^{+1.5\times10^{-5}}_{-3.1\times10^{-5}}$	0.0994	$1.76^{+0.03}_{-0.03}$	1.8
3R	$8.10^{+0.49}_{-0.65}$	7.5	$0.34^{+0.03}_{-0.07}$	$0.10057^{+4.0\times10^{-5}}_{-3.5\times10^{-5}}$	0.10057	$1.01^{+0.01}_{-0.03}$	1
3B	$8.18^{+0.61}_{-0.56}$	7.5	$0.30^{+0.05}_{-0.04}$	$0.09941^{+1.6\times10^{-5}}_{-1.9\times10^{-5}}$	0.09943	$0.98^{+0.02}_{-0.03}$	1
4R	$7.51^{+1.56}_{-0.69}$	7.5	$0.27^{+0.05}_{-0.09}$	$0.100552^{+5.7\times10^{-5}}_{-1.2\times10^{-4}}$	0.10054	$0.69^{+0.01}_{-0.01}$	0.686
4B	$7.94^{+1.03}_{-0.87}$	7.5	$0.37^{+0.09}_{-0.08}$	$0.09952^{+1.4\times10^{-5}}_{-6.8\times10^{-5}}$	0.09946	$0.67^{+0.02}_{-0.09}$	0.686
5R	$7.80^{+0.95}_{-0.96}$	7.5	$0.29^{+0.08}_{-0.07}$	$0.10049^{+1.2\times10^{-4}}_{-4\times10^{-5}}$	0.10051	$0.43^{+0.01}_{-0.01}$	0.43
5B	$7.33^{+1.00}_{-0.84}$	7.5	$0.30^{+0.09}_{-0.07}$	$0.09945^{+4.3\times10^{-5}}_{-7.9\times10^{-5}}$	0.09949	$0.44^{+0.02}_{-0.02}$	0.43

Table B.1: Table of the parameters of the model IOVP1 for `APEC` with temperatures in keV, metallicity in solar scale, density and redshift as the value obtained by the best fit model and the values that was set.

Region	T_{obs} keV	T_{Fit} keV	Z_{obs} $Z_\odot$	z_{obs}	z_{fit}	$N_{0,\,obs}$ $[10^{-4}]\,cm^{-5}$	$N_{0,\,fit}$ $[10^{-4}]\,cm^{-5}$
1R	$7.66^{+0.21}_{-0.21}$	7.5	$0.29^{+0.01}_{-0.01}$	$0.10057^{+1.6\times10^{-5}}_{-8.3\times10^{-6}}$	0.10058	$12.9^{+0.08}_{-0.08}$	13
1B	$7.38^{+0.21}_{-0.20}$	7.5	$0.29^{+0.01}_{-0.01}$	$0.09941^{+1.1\times10^{-5}}_{-2.9\times10^{-5}}$	0.09942	$12.8^{+0.11}_{-0.12}$	13
2R	$7.75^{+0.74}_{-0.71}$	7.5	$0.36^{+0.07}_{-0.06}$	$0.10033^{+4.2\times10^{-5}}_{-6.2\times10^{-5}}$	0.10036	$1.78^{+0.02}_{-0.02}$	1.8
2B	$6.93^{+0.95}_{-0.64}$	7.5	$0.28^{+0.04}_{-0.07}$	$0.09972^{+5.9\times10^{-5}}_{-2\times10^{-5}}$	0.09964	$1.84^{+0.03}_{-0.03}$	1.8
3R	$8.31^{+0.59}_{-0.74}$	7.5	$0.29^{+0.06}_{-0.03}$	$0.100267^{+4.4\times10^{-5}}_{-3.4\times10^{-6}}$	0.10029	$0.97^{+0.33}_{-0.37}$	1.01
3B	$7.09^{+0.56}_{-0.47}$	7.5	$0.27^{+0.04}_{-0.04}$	$0.09966^{+6.1\times10^{-5}}_{-3.5\times10^{-6}}$	0.09971	$1.01^{+0.02}_{-0.02}$	1.01
4R	$7.83^{+1.05}_{-0.93}$	7.5	$0.26^{+0.08}_{-0.06}$	$0.100163^{+2.3\times10^{-5}}_{-8.7\times10^{-5}}$	0.1002	$0.68^{+0.19}_{-0.18}$	0.67
4B	$7.12^{+0.96}_{-0.58}$	7.5	$0.33^{+0.08}_{-0.07}$	$0.09978^{+2.9\times10^{-5}}_{-5.2\times10^{-5}}$	0.0998	$0.68^{+0.03}_{-0.03}$	0.67
5R	$7.16^{+1.02}_{-0.90}$	7.5	$0.30^{+0.09}_{-0.07}$	$0.100156^{+1.3\times10^{-5}}_{-9.9\times10^{-5}}$	0.10016	$0.42^{+0.02}_{-0.02}$	0.42
5B	$7.02^{+1.27}_{-0.78}$	7.5	$0.18^{+0.10}_{-0.05}$	$0.09981^{+9.6\times10^{-5}}_{-8.0\times10^{-5}}$	0.09984	$0.42^{+0.01}_{-0.02}$	0.42

Table B.2: Table of the parameters of the model IOVP2A , same as B.1.

Region	T_{obs} keV	T_{Fit} keV	Z_{obs} $Z_{\odot}$	z_{obs}	z_{fit}	$N_{0,\,obs}$ $[10^{-4}]\,cm^{-5}$	$N_{0,\,fit}$ $[10^{-4}]\,cm^{-5}$
1R	$7.41^{+0.21}_{-0.2}$	7.5	$0.30^{+0.01}_{-0.01}$	$0.100678^{+9.0\times10^{-6}}_{-8.5\times10^{-8}}$	0.10068	$12.9^{+0.07}_{-0.07}$	13.2
1B	$7.64^{+0.05}_{-0.11}$	7.5	$0.29^{+0.009}_{-0.01}$	$0.09931^{+2.1\times10^{-5}}_{-3.8\times10^{-6}}$	0.09932	$13^{+0.02}_{-0.02}$	13.2
2R	$8.57^{+0.65}_{-1}$	7.5	$0.34^{+0.06}_{-0.07}$	$0.100457^{+4.8\times10^{-5}}_{-1.29\times10^{-5}}$	0.10043	$2.33^{+0.03}_{-0.03}$	2.37
2B	$7.92^{+0.77}_{-0.86}$	7.5	$0.34^{+0.06}_{-0.08}$	$0.09956^{+4.1\times10^{-5}}_{-1.4\times10^{-5}}$	0.09957	$2.30^{+0.03}_{-0.03}$	2.37
3R	$7.68^{+0.57}_{-0.55}$	7.5	$0.27^{+0.04}_{-0.04}$	$0.100384^{+1.2\times10^{-5}}_{-3.9\times10^{-5}}$	0.10034	$1.81^{+0.02}_{-0.02}$	1.89
3B	$8.15^{+0.35}_{-0.60}$	7.5	$0.29^{+0.05}_{-0.04}$	$0.09965^{+3.04\times10^{-6}}_{-4.08\times10^{-6}}$	0.09966	$1.72^{+0.04}_{-0.05}$	1.89
4R	$7.2^{+0.82}_{-0.9}$	7.5	$0.34^{+0.07}_{-0.08}$	$0.100292^{+3.16\times10^{-5}}_{-3.9\times10^{-5}}$	0.10024	$0.64^{+0.02}_{-0.02}$	0.67
4B	$7.62^{+0.8}_{-1.15}$	7.5	$0.27^{+0.07}_{-0.06}$	$0.09979^{+6.2\times10^{-5}}_{9.6\times10^{-6}}$	0.09976	$0.67^{+0.02}_{-0.01}$	0.67
5R	$6.13^{+1.16}_{-0.59}$	7.5	$0.30^{+0.11}_{-0.06}$	$0.100204^{+6.22\times10^{-6}}_{-2.8\times10^{-5}}$	0.100197	$0.45^{+0.01}_{-0.01}$	0.42
5B	$9.01^{+2.29}_{-1.02}$	7.5	$0.40^{+0.08}_{-0.15}$	$0.09986^{+1.7\times10^{-5}}_{-1.3\times10^{-4}}$	0.09981	$0.40^{+0.01}_{-0.01}$	0.42

Table B.3: Table of the parameters of the model IOVP2B for `APEC`, same as B.1.

Region	T_{obs} keV	T_{Fit} keV	Z_{obs} $Z_{\odot}$	z_{obs}	z_{fit}	$N_{0,\,obs}$ $[10^{-4}]\,cm^{-5}$	$N_{0,\,fit}$ $[10^{-4}]\,cm^{-5}$
1R	$5.90^{+0.04}_{-0.08}$	5.91	$0.30^{+0.008}_{-0.006}$	$0.10061^{+5.4\times10^{-6}}_{-4.57\times10^{-6}}$	0.100612	$65.8^{+0.12}_{-0.11}$	66.4
1B	$5.88^{+0.06}_{-0.06}$	5.91	$0.29^{+0.006}_{-0.007}$	$0.09937^{+1.3\times10^{-5}}_{-4.4\times10^{-6}}$	0.09939	$66.1^{+0.18}_{-0.17}$	66.4
2R	$4.70^{+0.17}_{-0.28}$	4.73	$0.33^{+0.02}_{-0.05}$	$0.100604^{+2.34\times10^{-5}}_{-3.3\times10^{-5}}$	0.100609	$2.89^{+0.04}_{-0.04}$	2.82
2B	$4.67^{+0.24}_{-0.22}$	4.73	$0.26^{+0.03}_{-0.03}$	$0.09937^{+1.9\times10^{-5}}_{-3.6\times10^{-5}}$	0.099391	$2.74^{+0.05}_{-0.07}$	2.82
3R	$4.08^{+0.16}_{-0.16}$	4.23	$0.26^{+0.03}_{-0.02}$	$0.100573^{+2.7\times10^{-5}}_{-1.5\times10^{-5}}$	0.10059	$2.59^{+0.09}_{-0.03}$	2.6
3B	$4.25^{+0.23}_{-0.15}$	4.23	$0.31^{+0.03}_{-0.03}$	$0.0994^{+2.1\times10^{-5}}_{-9.8\times10^{-6}}$	0.09941	$2.6^{+0.04}_{-0.03}$	2.6
4R	$3.36^{+0.41}_{-0.33}$	3.47	$0.26^{+0.09}_{-0.08}$	$0.100535^{+9.08\times10^{-5}}_{-6.6\times10^{-5}}$	0.100549	$0.34^{+0.04}_{-0.01}$	0.32
4B	$3.65^{+0.49}_{-0.41}$	3.47	$0.23^{+0.11}_{-0.06}$	$0.09939^{+3.5\times10^{-5}}_{-2.3\times10^{-5}}$	0.099451	$0.32^{+0.02}_{-0.01}$	0.32
5R	$2.92^{+0.70}_{-0.64}$	2.95	$0.24^{+0.26}_{-0.15}$	$0.10119^{+7.9\times10^{-4}}_{-6.7\times10^{-4}}$	0.10051	$0.07^{+0.02}_{-0.01}$	0.06
5B	$2.94^{+0.62}_{-0.57}$	2.95	$0.30^{+0.33}_{-0.11}$	$0.099437^{+2.1\times10^{-4}}_{-1.3\times10^{-4}}$	0.09949	$0.07^{+0.007}_{-0.006}$	0.06

Table B.4: Table of the parameters of the model NIOVP1 for `APEC`, same as B.1.

Region	T_{obs} keV	T_{Fit} keV	Z_{obs} $Z_{\odot}$	z_{obs}	z_{fit}	$N_{0,\,obs}$ $[10^{-4}]\,cm^{-5}$	$N_{0,\,fit}$ $[10^{-4}]\,cm^{-5}$
1R	$5.92^{+0.06}_{-0.06}$	5.94	$0.30^{+0.007}_{-0.007}$	$0.100601^{+5.0\times10^{-6}}_{-7.8\times10^{-6}}$	0.1006	$66.8^{+0.32}_{-0.32}$	67.5
1B	$5.98^{+0.06}_{-0.06}$	5.94	$0.30^{+0.007}_{-0.007}$	$0.09940^{+7.6\times10^{-7}}_{-5.8\times10^{-6}}$	0.0994	$66.7^{+0.3}_{-0.30}$	67.5
2R	$4.81^{+0.24}_{-0.22}$	4.75	$0.29^{+0.035}_{-0.03}$	$0.10038^{+2.3\times10^{-5}}_{-0.7\times10^{-5}}$	0.10039	$2.75^{+0.04}_{-0.04}$	2.8
2B	$4.75^{+0.25}_{-0.21}$	4.75	$0.3^{+0.036}_{-0.03}$	$0.09958^{+1.7\times10^{-5}}_{-0.8\times10^{-5}}$	0.09961	$2.83^{+0.04}_{-0.04}$	2.8
3R	$4.23^{+0.21}_{-0.13}$	4.24	$0.33^{+0.02}_{-0.05}$	$0.100308^{+6.8\times10^{-6}}_{-1.2\times10^{-5}}$	0.10031	$2.57^{+0.03}_{-0.03}$	2.6
3B	$4.21^{+0.17}_{-0.15}$	4.24	$0.30^{+0.03}_{-0.03}$	$0.09968^{+1.9\times10^{-5}}_{-3.9\times10^{-6}}$	0.09969	$2.58^{+0.4}_{-0.3}$	2.6
4R	$3.86^{+0.36}_{-0.46}$	3.47	$0.40^{+0.10}_{-0.13}$	$0.100234^{+3.5\times10^{-5}}_{-4\times10^{-4}}$	0.10022	$0.29^{+0.01}_{-0.01}$	0.31
4B	$3.9^{+0.48}_{-0.41}$	3.47	$0.41^{+0.13}_{-0.10}$	$0.099874^{+6.3\times10^{-5}}_{-7.9\times10^{-5}}$	0.09978	$0.28^{+0.02}_{-0.02}$	0.31
5R	$2.94^{+0.95}_{-0.67}$	2.94	$0.14^{+0.23}_{-0.12}$	$0.10195^{+2.2\times10^{-4}}_{-5.1\times10^{-4}}$	0.10016	$0.06^{+0.02}_{-0.01}$	0.06
5B	$2.26^{+0.46}_{-0.31}$	2.94	$0.32^{+0.22}_{-0.14}$	$0.09989^{+3.1\times10^{-4}}_{-1.9\times10^{-4}}$	0.09984	$0.07^{+0.008}_{-0.008}$	0.06

Table B.5: Table of the parameters of the model NIOVP2A for `APEC`, same as B.1.

Region	T_{obs} keV	T_{Fit} keV	Z_{obs} $Z_{\odot}$	z_{obs}	z_{fit}	$N_{0,\,obs}$ $[10^{-4}]\,cm^{-5}$	$N_{0,\,fit}$ $[10^{-4}]\,cm^{-5}$
1R	$5.96^{+0.06}_{-0.06}$	5.96	$0.29^{+0.007}_{-0.007}$	$0.100705^{+5.9\times10^{-6}}_{-5.3\times10^{-6}}$	0.10071	$63.9^{+0.23}_{-0.23}$	64.7
1B	$5.99^{+0.06}_{-0.06}$	5.96	$0.30^{+0.007}_{-0.007}$	$0.09929^{+5.6\times10^{-6}}_{-2.7\times10^{-7}}$	0.09929	$63.6^{+0.19}_{-0.19}$	64.7
2R	$4.8^{+0.23}_{-0.24}$	4.78	$0.31^{+0.03}_{-0.03}$	$0.10047^{+1.0\times10^{-5}}_{-1.2\times10^{-5}}$	0.10046	$5.70^{+0.06}_{-0.07}$	5.72
2B	$4.47^{+0.20}_{-0.22}$	4.78	$0.29^{+0.03}_{-0.03}$	$0.09952^{+2.5\times10^{-5}}_{-1.06\times10^{-5}}$	0.09954	$5.72^{+0.04}_{-0.06}$	5.72
3R	$4.15^{+0.16}_{-0.15}$	4.28	$0.29^{+0.03}_{-0.03}$	$0.100363^{+2.3\times10^{-5}}_{-1.3\times10^{-5}}$	0.10037	$2.83^{+0.08}_{-0.08}$	2.83
3B	$4.18^{+0.17}_{-0.15}$	4.28	$0.32^{+0.03}_{-0.03}$	$0.09963^{+2.1\times10^{-5}}_{-9.9\times10^{-6}}$	0.09963	$2.81^{+0.04}_{-0.04}$	2.83
4R	$3.98^{+0.61}_{-0.36}$	3.51	$0.28^{+0.08}_{-0.11}$	$0.100242^{+7.4\times10^{-5}}_{-1.3\times10^{-4}}$	0.10026	$0.29^{+0.007}_{-0.03}$	0.32
4B	$3.48^{+0.39}_{-0.40}$	3.51	$0.36^{+0.09}_{-0.11}$	$0.09977^{+3.9\times10^{-5}}_{-1.3\times10^{-4}}$	0.09974	$0.3^{+0.01}_{-0.01}$	0.32
5R	$3.01^{+0.73}_{-0.55}$	2.98	$0.34^{+0.38}_{-0.17}$	$0.100206^{+5.6\times10^{-5}}_{-4\times10^{-4}}$	0.10020	$0.06^{+0.01}_{-0.01}$	0.01
5B	$2.97^{+0.88}_{-0.61}$	2.98	$0.26^{+0.24}_{-0.15}$	$0.09977^{+1\times10^{-4}}_{-1.9\times10^{-4}}$	0.0998	$0.06^{+0.02}_{-0.01}$	0.06

Table B.6: Table of the parameters of the model NIOVP2B for `APEC`, same as B.1.

Region	T_{obs} keV	T_{Fit} keV	Z_{obs} $Z_\odot$	z_{obs}	z_{fit}	$N_{0,\,obs}$ $[10^{-4}]\,cm^{-5}$	$N_{0,\,fit}$ $[10^{-4}]\,cm^{-5}$
1R	$5.35^{+0.03}_{-0.03}$	5.36	$0.30^{+0.005}_{-0.005}$	$0.100608^{+7.6\times10^{-6}}_{-1.8\times10^{-5}}$	0.10061	$12.1^{+0.52}_{-0.52}$	12.1
1B	$5.35^{+0.03}_{-0.03}$	5.36	$0.30^{+0.005}_{-0.005}$	$0.09938^{+3.4\times10^{-6}}_{-7.39\times10^{-6}}$	0.09939	$12^{+0.53}_{-0.52}$	12.1
2R	$4.33^{+0.21}_{-0.17}$	4.18	$0.32^{+0.03}_{-0.03}$	$0.100604^{+4.8\times10^{-7}}_{-2.0\times10^{-6}}$	0.10061	$2.97^{+0.03}_{-0.04}$	3.1
2B	$4.19^{+0.14}_{-0.15}$	4.18	$0.33^{+0.03}_{-0.03}$	$0.09937^{+1.4\times10^{-5}}_{+6\times10^{-6}}$	0.09939	$3.11^{+0.04}_{-0.04}$	3.1
3R	$3.83^{+0.10}_{-0.26}$	3.68	$0.26^{+0.03}_{-0.02}$	$0.100593^{+1.0\times10^{-5}}_{-3.6\times10^{-5}}$	0.10059	$2.53^{+0.03}_{-0.03}$	2.69
3B	$3.75^{+0.15}_{-0.15}$	3.68	$0.30^{+0.03}_{-0.02}$	$0.099437^{+4.2\times10^{-6}}_{-1.4\times10^{-5}}$	0.09941	$2.58^{+0.03}_{-0.03}$	2.69
4R	$2.91^{+0.45}_{-0.34}$	2.91	$0.29^{+0.1}_{-0.13}$	$0.100498^{+2.2\times10^{-4}}_{-4.1\times10^{-5}}$	0.10055	$0.17^{+0.01}_{-0.01}$	0.18
4B	$2.90^{+0.36}_{-0.41}$	2.91	$0.30^{+0.15}_{-0.10}$	$0.09946^{+1.2\times10^{-4}}_{-6.8\times10^{-5}}$	0.09945	$0.18^{+0.01}_{-0.02}$	0.18
5R	$2.07^{+0.97}_{-0.49}$	2.36	$0.18^{+0.32}_{-0.15}$	$0.101428^{+4.4\times10^{-4}}_{-1.3\times10^{-4}}$	0.10051	$0.02^{+0.012}_{-0.008}$	0.02
5B	$2.99^{+1.71}_{-0.75}$	2.36	$0.32^{+0.53}_{-0.22}$	$0.099396^{+3.3\times10^{-4}}_{-2.2\times10^{-4}}$	0.09949	$0.019^{+0.006}_{-0.003}$	0.02

Table B.7: Table of the parameters of the model CCOVP1 for `APEC`, same as B.1.

Region	T_{obs} keV	T_{Fit} keV	Z_{obs} $Z_\odot$	z_{obs}	z_{fit}	$N_{0,\,obs}$ $[10^{-4}]\,cm^{-5}$	$N_{0,\,fit}$ $[10^{-4}]\,cm^{-5}$
1R	$5.56^{+0.01}_{-0.01}$	5.57	$0.30^{+0.001}_{-0.001}$	$0.100601^{+1.1\times10^{-6}}_{-1.09\times10^{-6}}$	0.1006	9.99^{+1}_{-1}	10
1B	$5.56^{+0.05}_{-0.04}$	5.57	$0.29^{+0.005}_{-0.005}$	$0.09939^{+7.4\times10^{-6}}_{-3.0\times10^{-6}}$	0.0994	$9.99^{+0.31}_{-0.31}$	10
2R	$4.33^{+0.2}_{-0.16}$	4.38	$0.26^{+0.03}_{-0.028}$	$0.10044^{+1.58\times10^{-5}}_{-2.9\times10^{-5}}$	0.10039	$3.04^{+0.04}_{-0.05}$	3
2B	$4.47^{+0.21}_{-0.18}$	4.38	$0.3^{+0.03}_{-0.03}$	$0.09965^{+2.36\times10^{-6}}_{-7\times10^{-5}}$	0.09961	$2.96^{+0.04}_{-0.04}$	3
3R	$3.76^{+0.15}_{-0.15}$	3.88	$0.25^{+0.03}_{-0.03}$	$0.100306^{+9.9\times10^{-6}}_{-3.00\times10^{-5}}$	0.10031	$2.83^{+0.04}_{-0.04}$	2.75
3B	$3.96^{+0.15}_{-0.16}$	3.88	$0.31^{+0.03}_{-0.03}$	$0.09972^{+6.9\times10^{-6}}_{-5.22\times10^{-5}}$	0.09969	$2.65^{+0.04}_{-0.03}$	2.75
4R	$3.10^{+0.59}_{-0.25}$	3.10	$0.3^{+0.19}_{-0.06}$	$0.100223^{+8.29\times10^{-5}}_{-1.9\times10^{-4}}$	0.10022	$0.25^{+0.01}_{-0.01}$	0.21
4B	$2.66^{+0.31}_{-0.22}$	3.10	$0.3^{+0.13}_{-0.07}$	$0.09978^{+8.13\times10^{-5}}_{-2\times10^{-4}}$	0.09978	$0.24^{+0.01}_{-0.01}$	0.21
5R	$2.53^{+0.64}_{-0.67}$	2.55	$0.30^{+0.40}_{-0.19}$	$0.09994^{+3.5\times10^{-4}}_{-2.6\times10^{-4}}$	0.10017	$0.03^{+0.01}_{-0.004}$	0.03
5B	$2.35^{+0.93}_{-0.42}$	2.55	$0.20^{+0.29}_{-0.12}$	$0.099714^{+6.1\times10^{-4}}_{-7.0\times10^{-4}}$	0.09983	$0.03^{+0.01}_{-0.004}$	0.03

Table B.8: Table of the parameters of the model CCOVP2A for `APEC`, same as B.1.

Region	T_{obs} keV	T_{Fit} keV	Z_{obs} $Z_{\odot}$	z_{obs}	z_{fit}	$N_{0,\,obs}$ $[10^{-4}]\,cm^{-5}$	$N_{0,\,fit}$ $[10^{-4}]\,cm^{-5}$
1R	$5.30^{+0.03}_{-0.03}$	5.30	$0.29^{+0.004}_{-0.004}$	$0.100719^{+1.7\times10^{-6}}_{-3.95\times10^{-6}}$	0.10072	$13.0^{+0.53}_{-0.52}$	13.1
1B	$5.28^{+0.03}_{-0.03}$	5.30	$0.29^{0.005}_{-0.004}$	$0.09928^{+7.2\times10^{-6}}_{-4.4\times10^{-6}}$	0.09928	$13.0^{+0.25}_{-0.25}$	13.1
2R	$4.09^{+0.14}_{-0.15}$	4.12	$0.31^{+0.029}_{-0.03}$	$0.10049^{+1.8\times10^{-5}}_{-2.8\times10^{-5}}$	0.10047	$6.87^{+0.09}_{-0.05}$	6.93
2B	$4.37^{+0.16}_{-0.21}$	4.12	$0.3^{+0.032}_{-0.034}$	$0.09958^{+5.24\times10^{-5}}_{-1.5\times10^{-5}}$	0.09953	$6.94^{+0.08}_{-0.08}$	6.93
3R	$3.62^{+0.19}_{-0.11}$	3.62	$0.30^{+0.05}_{-0.02}$	$0.100377^{+2.3\times10^{-5}}_{-3.4\times10^{-5}}$	0.10038	$2.57^{+0.03}_{-0.04}$	2.65
3B	$3.53^{+0.14}_{-0.14}$	3.62	$0.27^{+0.03}_{-0.03}$	$0.09959^{+4.9\times10^{-5}}_{-6.1\times10^{-8}}$	0.09962	$2.67^{+0.04}_{-0.03}$	2.65
4R	$2.72^{+0.26}_{-0.4}$	2.84	$0.29^{+0.10}_{-0.13}$	$0.10049^{+1.0\times10^{-4}}_{-2.3\times10^{-4}}$	0.10026	$0.17^{+0.01}_{-0.01}$	0.16
4B	$2.83^{+0.40}_{-0.37}$	2.84	$0.30^{+0.09}_{-0.17}$	$0.09970^{+1.8\times10^{-4}}_{-2.5\times10^{-4}}$	0.09974	$0.16^{+0.02}_{-0.02}$	0.16
5R	$2.06^{+0.85}_{-0.50}$	2.28	$0.42^{+0.78}_{-0.25}$	$0.100278^{+4.4\times10^{-4}}_{-4.1\times10^{-4}}$	0.10020	$0.017^{+0.008}_{-0.007}$	0.01
5B	$2.28^{+1.12}_{-0.48}$	2.28	$0.29^{0.45}_{-0.2}$	$0.100028^{+2.1\times10^{-4}}_{-6.3\times10^{-4}}$	0.09980	$0.0015^{+0.005}_{-0.005}$	0.01

Table B.9: Table of the parameters of the model CCOVP2B for `APEC`, same as B.1.

Region	T_{obs} keV	T_{Fit} keV	Z_{obs} $Z_{\odot}$	z_{obs}	z_{fit}	$N_{0,\,obs}$ $[10^{-4}]\,cm^{-5}$	$N_{0,\,fit}$ $[10^{-4}]\,cm^{-5}$
1R	$7.73^{+0.36}_{-0.35}$	7.5	$0.30^{+0.03}_{-0.03}$	$0.10213^{+4.6\times10^{-6}}_{-7.2\times10^{-6}}$	0.10213	$5.06^{+0.08}_{-0.08}$	5.13
1B	$7.30^{+0.33}_{-0.32}$	7.5	$0.29^{+0.03}_{-0.02}$	$0.09786^{+1.87\times10^{-5}}_{-2.7\times10^{-7}}$	0.09787	$5.15^{+0.04}_{-0.04}$	5.13
2R	$8.2^{+1.15}_{-1.16}$	7.5	$0.39^{+0.07}_{-0.12}$	$0.1021^{+1.74\times10^{-5}}_{-1.2\times10^{-4}}$	0.1020	$1.39^{+0.02}_{-0.01}$	1.42
2B	$6.66^{+0.96}_{-0.69}$	7.5	$0.27^{+0.07}_{-0.06}$	$0.979^{+5.8\times10^{-6}}_{-7.17\times10^{-6}}$	0.098	$1.45^{+0.02}_{-0.02}$	1.42
3R	$7.73^{+0.52}_{-0.83}$	7.5	$0.29^{+0.05}_{-0.05}$	$0.102005^{+4.6\times10^{-5}}_{-2.3\times10^{-5}}$	0.10201	$1.33^{+0.02}_{-0.02}$	1.32
3B	$7.49^{+0.61}_{-0.67}$	7.5	$0.29^{+0.04}_{-0.06}$	$0.09799^{+1.4\times10^{-5}}_{-7.8\times10^{-5}}$	0.09799	$1.35^{+0.02}_{-0.02}$	1.32
4R	$7.47^{+0.83}_{-1.02}$	7.5	$0.28^{+0.07}_{-0.08}$	$0.10184^{+5.2\times10^{-5}}_{-1.2\times10^{-4}}$	0.1018	$0.61^{+0.02}_{-0.01}$	0.63
4B	$7.65^{+0.95}_{-0.87}$	7.5	$0.33^{+0.08}_{-0.07}$	$0.09819^{+8.5\times10^{-5}}_{-4.4\times10^{-5}}$	0.0982	$0.62^{+0.02}_{-0.02}$	0.63
5R	$6.84^{+0.80}_{-0.80}$	7.5	$0.18^{+0.07}_{-0.05}$	$0.101642^{+3.2\times10^{-5}}_{-3.4\times10^{-5}}$	0.10179	$0.49^{+0.02}_{-0.01}$	0.47
5B	$7.56^{+1.32}_{-0.92}$	7.5	$0.31^{+0.10}_{-0.08}$	$0.098163^{+8.8\times10^{-5}}_{-1.0\times10^{-5}}$	0.09821	$0.45^{+0.01}_{-0.01}$	0.47

Table B.10: Table of the parameters of the model IPVP1 for `APEC`, same as B.1.

Region	T_{obs} keV	T_{Fit} keV	Z_{obs} $Z_{\odot}$	z_{obs}	z_{fit}	$N_{0,\,obs}$ $[10^{-4}]\,cm^{-5}$	$N_{0,\,fit}$ $[10^{-4}]\,cm^{-5}$
1R	$7.66^{+0.28}_{-0.28}$	7.5	$0.29^{+0.02}_{-0.02}$	$0.1019^{+5.4\times10^{-6}}_{-1.0\times10^{-5}}$	0.1019	$7.12^{+0.06}_{-0.05}$	7.18
1B	$7.56^{+0.27}_{-0.28}$	7.5	$0.30^{+0.02}_{-0.02}$	$0.098091^{+1.4\times10^{-5}}_{-9.6\times10^{-6}}$	0.0981	$7.14^{+0.09}_{-0.09}$	7.18
2R	$7.51^{+1.23}_{-0.79}$	7.5	$0.297^{+0.05}_{-0.10}$	$0.10121^{+7.1\times10^{-5}}_{-4.33\times10^{-5}}$	0.1012	$1.55^{+0.02}_{-0.01}$	1.54
2B	$8.5^{+0.86}_{-1.49}$	7.5	$0.29^{+0.09}_{-0.076}$	$0.09880^{+6.86\times10^{-5}}_{-5.36\times10^{-5}}$	0.0988	$1.48^{+0.02}_{-0.01}$	1.54
3R	$6.73^{+0.93}_{-0.42}$	7.5	$0.30^{+0.05}_{-0.05}$	$0.100942^{+2.7\times10^{-5}}_{-1.9\times10^{-5}}$	0.10095	$1.23^{+0.02}_{-0.02}$	1.28
3B	$7.20^{+0.70}_{-0.64}$	7.5	$0.27^{+0.05}_{-0.05}$	$0.09902^{+5.1\times10^{-5}}_{-1.3\times10^{-5}}$	0.09905	$1.19^{+0.02}_{-0.02}$	1.28
4R	$6.14^{+0.8}_{-0.7}$	7.5	$0.26^{+0.08}_{-0.67}$	$0.100605^{+1.3\times10^{-4}}_{-2.28\times10^{-5}}$	0.10069	$0.55^{+0.02}_{-0.01}$	0.54
4B	$6.84^{+1.17}_{-0.77}$	7.5	$0.25^{+0.08}_{-0.07}$	$0.09932^{+7.4\times10^{-5}}_{-2.24\times10^{-5}}$	0.09931	$0.51^{+0.03}_{-0.02}$	0.54
5R	$8.73^{+1.84}_{-1.04}$	7.5	$0.37^{+0.14}_{-0.10}$	$0.100637^{+3.8\times10^{-5}}_{-1.3\times10^{-4}}$	0.10055	$0.33^{+0.01}_{-0.01}$	0.33
5B	$7.44^{+1.7}_{-2.0}$	7.5	$0.28^{+0.12}_{-0.11}$	$0.09938^{+7.4\times10^{-5}}_{-1.4\times10^{-4}}$	0.09945	$0.33^{+0.02}_{-0.02}$	0.33

Table B.11: Table of the parameters of the model IPVP2A for `APEC` , same as B.1.

Region	T_{obs} keV	T_{Fit} keV	Z_{obs} $Z_{\odot}$	z_{obs}	z_{fit}	$N_{0,\,obs}$ $[10^{-4}]\,cm^{-5}$	$N_{0,\,fit}$ $[10^{-4}]\,cm^{-5}$
1R	$7.30^{+0.27}_{-0.27}$	7.5	$0.29^{+0.02}_{-0.02}$	$0.101794^{+1.9\times10^{-5}}_{-7.4\times10^{-6}}$	0.1018	$7.43^{+0.51}_{-0.53}$	7.42
1B	$7.29^{+0.30}_{-0.28}$	7.5	$0.31^{+0.02}_{-0.02}$	$0.098194^{+1.2\times10^{-5}}_{-2.4\times10^{-6}}$	0.0982	$7.44^{+0.10}_{-0.10}$	7.42
2R	$8.25^{+0.87}_{-1.2}$	7.5	$0.38^{+0.1}_{-0.089}$	$0.100857^{+3.3\times10^{-5}}_{-2.6\times10^{-5}}$	0.10085	$1.53^{+0.01}_{-0.03}$	1.55
2B	$7.14^{+0.53}_{-1.43}$	7.5	$0.28^{+0.058}_{-0.096}$	$0.09980^{+2.5\times10^{-5}}_{-9.4\times10^{-5}}$	0.09915	$1.52^{+0.01}_{-0.01}$	1.55
3R	$7.51^{+0.77}_{-0.63}$	7.5	$0.29^{+0.06}_{-0.05}$	$0.100905^{+1.4\times10^{-5}}_{-3.1\times10^{-5}}$	0.100904	$1.21^{+0.02}_{-0.03}$	1.27
3B	$6.91^{+0.51}_{-0.42}$	7.5	$0.30^{+0.05}_{-0.04}$	$0.099100^{+1.94\times10^{-5}}_{-2.3\times10^{-5}}$	0.099096	$1.30^{+0.02}_{-0.02}$	1.27
4R	$7.1^{+0.78}_{-1.12}$	7.5	$0.28^{+0.07}_{-0.09}$	$0.100599^{+2.16\times10^{-5}}_{-1.52\times10^{-5}}$	0.10049	$0.47^{+0.01}_{-0.01}$	0.46
4B	$8.9^{+1.27}_{-1.7}$	7.5	$0.27^{+0.08}_{-0.11}$	$0.09947^{+2.7\times10^{-5}}_{-1.0\times10^{-4}}$	0.09951	$0.44^{+0.01}_{-0.01}$	0.46
5R	$7.34^{+1.42}_{-0.99}$	7.5	$0.43^{+0.09}_{-0.16}$	$0.100590^{+3.0\times10^{-5}}_{-1.5\times10^{-4}}$	0.10052	$0.33^{+0.01}_{-0.01}$	0.33
5B	$7.48^{+1.06}_{-1.62}$	7.5	$0.29^{+0.09}_{-0.11}$	$0.099470^{+5.8\times10^{-5}}_{-1.1\times10^{-4}}$	0.09948	$0.32^{+0.01}_{-0.01}$	0.33

Table B.12: Table of the parameters of the model IPVP2B for `APEC`, same as B.1.

Region	T_{obs} keV	T_{Fit} keV	Z_{obs} $Z_\odot$	z_{obs}	z_{fit}	$N_{0,\,obs}$ $[10^{-4}]\,cm^{-5}$	$N_{0,\,fit}$ $[10^{-4}]\,cm^{-5}$
1R	$5.92^{+0.14}_{-0.14}$	6.11	$0.29^{+0.01}_{-0.01}$	$0.102213^{+3.1\times10^{-8}}_{-1.2\times10^{-5}}$	0.10221	$12.8^{+0.06}_{-0.07}$	12.7
1B	$6.19^{+0.15}_{-0.15}$	6.11	$0.29^{+0.01}_{-0.01}$	$0.09779^{+9.2\times10^{-6}}_{-4.7\times10^{-6}}$	0.09779	$12.5^{+0.08}_{-0.08}$	12.7
2R	$4.95^{+0.4}_{-0.37}$	5.13	$0.26^{+0.06}_{-0.05}$	$0.10216^{+3.12\times10^{-5}}_{-9.393.12\times10^{-5}}$	0.1021	$1.79^{+0.03}_{-0.03}$	1.7
2B	$5.12^{+0.31}_{-0.50}$	5.13	$0.29^{+0.035}_{-0.08}$	$0.0979^{+2.27\times10^{-6}}_{-4.65\times10^{-5}}$	0.0979	$1.68^{+0.03}_{-0.02}$	1.7
3R	$4.42^{+0.30}_{-0.24}$	4.72	$0.33^{+0.03}_{-0.05}$	$0.102117^{+2.1\times10^{-6}}_{-2.9\times10^{-5}}$	0.102107	$1.03^{+0.5}_{-0.45}$	1.03
3B	$5.09^{+0.30}_{-0.29}$	4.72	$0.34^{+0.04}_{-0.04}$	$0.097876^{+3.0\times10^{-5}}_{-3.0\times10^{-6}}$	0.097893	$0.99^{+0.02}_{-0.02}$	1.03
4R	$4.14^{+0.6}_{-0.32}$	4.14	$0.3^{+0.1}_{-0.06}$	$0.10190^{+2.92\times10^{-5}}_{-1\times10^{-4}}$	0.1019	$0.46^{+0.01}_{-0.01}$	0.46
4B	$4.49^{+0.57}_{-0.49}$	4.14	$0.28^{+0.09}_{-0.075}$	$0.0981^{+3.37\times10^{-5}}_{-2.72\times10^{-5}}$	0.0981	$0.44^{+0.02}_{-0.02}$	0.46
5R	$2.97^{+0.41}_{-0.43}$	3.76	$0.18^{+0.12}_{-0.07}$	$0.101826^{+1.3\times10^{-4}}_{-1.3\times10^{-4}}$	0.10185	$0.26^{+0.04}_{-0.02}$	0.21
5B	$3.90^{+0.71}_{-0.48}$	3.76	$0.25^{+0.15}_{-0.09}$	$0.098177^{+1.1\times10^{-4}}_{-9.1\times10^{-5}}$	0.09815	$0.21^{+0.02}_{-0.02}$	0.21

Table B.13: Table of the parameters of the model NIPVP1 for `APEC`, same as B.1.

Region	T_{obs} keV	T_{Fit} keV	Z_{obs} $Z_\odot$	z_{obs}	z_{fit}	$N_{0,\,obs}$ $[10^{-4}]\,cm^{-5}$	$N_{0,\,fit}$ $[10^{-4}]\,cm^{-5}$
1R	$6.31^{+0.12}_{-0.12}$	6.28	$0.30^{+0.01}_{-0.01}$	$0.101955^{+8.2\times10^{-6}}_{-5.7\times10^{-6}}$	0.10195	$18.9^{+0.09}_{-0.06}$	19.1
1B	$6.16^{+0.12}_{-0.12}$	6.28	$0.29^{+0.01}_{-0.01}$	$0.0980459^{+8.9\times10^{-6}}_{-3.8\times10^{-6}}$	0.09805	$19^{+0.12}_{-0.12}$	19.1
2R	$5.37^{+0.42}_{-0.37}$	5.19	$0.29^{+0.05}_{-0.04}$	$0.1011^{+7.84\times10^{-5}}_{-4.96\times10^{-5}}$	0.1012	$1.56^{+0.02}_{-0.02}$	1.6
2B	$5.05^{+0.45}_{-0.37}$	5.19	$0.26^{+0.05}_{-0.046}$	$0.09882^{+8.4\times10^{-5}}_{-1.89\times10^{-5}}$	0.0988	$1.62^{+0.03}_{-0.03}$	1.6
3R	$5.02^{+0.31}_{-0.29}$	4.71	$0.33^{+0.04}_{-0.04}$	$0.101033^{+2.9\times10^{-5}}_{-2.95\times10^{-5}}$	0.10102	$1.09^{+0.02}_{-0.02}$	1.1
3B	$4.59^{+0.28}_{-0.26}$	4.71	$0.28^{+0.04}_{-0.04}$	$0.0990142^{+2.5\times10^{-5}}_{-2.5\times10^{-5}}$	0.09898	$1.12^{+0.05}_{-0.05}$	1.1
4R	$3.97^{+0.61}_{-0.45}$	4.00	$0.29^{+0.11}_{-0.087}$	$0.10068^{+1.9\times10^{-5}}_{-1.01\times10^{-5}}$	0.1007	$0.3^{+0.03}_{-0.02}$	0.29
4B	$4.00^{+0.79}_{-0.41}$	4.00	$0.3^{+0.14}_{-0.08}$	$0.09929^{+1.9\times10^{-5}}_{-5.2\times10^{-5}}$	0.0993	$0.25^{+0.01}_{-0.01}$	0.29
5R	$3.28^{+0.86}_{-0.57}$	3.54	$0.20^{+0.17}_{-0.11}$	$0.100571^{+2.4\times10^{-4}}_{-1.9\times10^{-4}}$	0.10056	$0.10^{+0.01}_{-0.01}$	0.099
5B	$3.23^{+0.60}_{-0.53}$	3.54	$0.29^{+0.16}_{-0.13}$	$0.09944^{+3.1\times10^{-4}}_{-1.5\times10^{-4}}$	0.09944	$0.11^{+0.009}_{-0.008}$	0.099

Table B.14: Table of the parameters of the model NIPVP2A for `APEC`, same as B.1.

Region	T_{obs} keV	T_{Fit} keV	Z_{obs} $Z_\odot$	z_{obs}	z_{fit}	$N_{0,\,obs}$ $[10^{-4}]\,cm^{-5}$	$N_{0,\,fit}$ $[10^{-4}]\,cm^{-5}$
1R	$6.26^{+0.07}_{-0.19}$	6.27	$0.28^{+0.01}_{-0.009}$	$0.101939^{+1.3\times10^{-6}}_{-1.03\times10^{-6}}$	0.10194	$19.3^{+0.09}_{-0.09}$	19.3
1B	$6.26^{+0.12}_{-0.11}$	6.27	$0.31^{+0.01}_{-0.01}$	$0.098061^{+4.1\times10^{-7}}_{-6.3\times10^{-6}}$	0.09806	$19.1^{+0.10}_{-0.05}$	19.3
2R	$5.58^{+0.46}_{-0.33}$	5.18	$0.36^{+0.07}_{-0.04}$	$0.10124^{+5.6\times10^{-5}}_{-1.6\times10^{-5}}$	0.1012	$2.62^{+0.05}_{-0.04}$	2.61
2B	$5.33^{+0.35}_{-0.47}$	5.18	$0.32^{+0.04}_{-0.06}$	$0.0988^{+3.9\times10^{-5}}_{+3.9\times10^{-6}}$	0.0988	$2.56^{+0.05}_{-0.05}$	2.61
3R	$4.68^{+0.30}_{-0.28}$	4.70	$0.29^{+0.04}_{-0.04}$	$0.100994^{+5.4\times10^{-5}}_{-2.0\times10^{-5}}$	0.10102	$1.59^{+0.03}_{-0.02}$	1.6
3B	$4.95^{+0.33}_{-0.30}$	4.70	$0.30^{+0.04}_{-0.04}$	$0.0986^{+6.2\times10^{-5}}_{-5.2\times10^{-5}}$	0.09898	$1.58^{+0.03}_{-0.02}$	1.6
4R	$3.78^{+0.43}_{-0.53}$	4.00	$0.23^{+0.07}_{-0.09}$	$0.1007^{+1.1\times10^{-4}}_{-6.3\times10^{-5}}$	0.10072	$0.31^{+0.02}_{-0.01}$	0.29
4B	$4.27^{+0.49}_{-0.67}$	4.00	$0.31^{+0.09}_{-0.11}$	$0.09937^{+7.8\times10^{-5}}_{-6.5\times10^{-5}}$	0.09928	$0.3^{+0.02}_{-0.02}$	0.29
5R	$3.40^{+0.85}_{-0.61}$	3.53	$0.17^{+0.16}_{-0.10}$	$0.100418^{+2.3\times10^{-4}}_{-2.4\times10^{-4}}$	0.100558	$0.10^{+0.01}_{-0.01}$	0.09
5B	$3.24^{+0.82}_{-0.50}$	3.53	$0.37^{+0.22}_{-0.16}$	$0.099507^{+8.5\times10^{-5}}_{-1.1\times10^{-4}}$	0.099442	$0.099^{+0.01}_{-0.01}$	0.09

Table B.15: Table of the parameters of the model NIPVP2B for `APEC` , same as B.1.

Region	T_{obs} keV	T_{Fit} keV	Z_{obs} $Z_\odot$	z_{obs}	z_{fit}	$N_{0,\,obs}$ $[10^{-4}]\,cm^{-5}$	$N_{0,\,fit}$ $[10^{-4}]\,cm^{-5}$
1R	$5.44^{+0.10}_{-0.08}$	5.56	$0.29^{+0.01}_{-0.01}$	$0.102206^{+4.6\times10^{-6}}_{-3.1\times10^{-6}}$	0.10221	$21.3^{+0.15}_{-0.13}$	21.3
1B	$5.52^{+0.10}_{-0.11}$	5.56	$0.30^{+0.01}_{-0.01}$	$0.097795^{+1.5\times10^{-5}}_{-8.4\times10^{-6}}$	0.09779	$21.3^{+0.17}_{-0.16}$	21.3
2R	$4.58^{+0.48}_{-0.24}$	4.58	$0.35^{+0.036}_{-0.08}$	$0.10209^{+3.8\times10^{-5}}_{-5.9\times10^{-5}}$	0.10219	$2.45^{+5.5}_{-1.4}$	1.83
2B	$4.73^{+0.35}_{-0.33}$	4.58	$0.31^{+0.05}_{-0.05}$	$0.0977^{+2.2\times10^{-5}}_{-1.6\times10^{-5}}$	0.0978	$1.78^{+0.03}_{-0.03}$	1.83
3R	$3.61^{+2.33}_{-1.26}$	4.16	$0.22^{+0.25}_{-0.14}$	$0.102102^{+1.5\times10^{-4}}_{-1.2\times10^{-4}}$	0.10211	$1.18^{+0.02}_{-0.02}$	1.2
3B	$4.10^{+0.19}_{-0.18}$	4.16	$0.32^{+0.04}_{-0.04}$	$0.09781^{+5.1\times10^{-5}}_{-1.67\times10^{-5}}$	0.09789	$1.1^{+0.02}_{-0.05}$	1.2
4R	$3.61^{+0.43}_{-0.36}$	3.56	$0.22^{+0.09}_{-0.06}$	$0.1018^{+5.7\times10^{-5}}_{-1.2\times10^{-5}}$	0.1019	$0.37^{+0.02}_{-0.03}$	0.36
4B	$3.55^{+0.25}_{-0.54}$	3.56	$0.29^{+0.06}_{-0.11}$	$0.0981^{+1.7\times10^{-4}}_{-1.5\times10^{-4}}$	0.0981	$0.35^{+0.01}_{-0.01}$	0.36
5R	$3.42^{+0.53}_{-0.46}$	3.17	$0.46^{+0.23}_{-0.16}$	$0.101887^{+1.1\times10^{-4}}_{-1.0\times10^{-4}}$	0.10185	$0.1^{+0.01}_{-0.008}$	0.13
5B	$3.16^{+0.68}_{-0.31}$	3.17	$0.59^{+0.19}_{-0.23}$	$0.098164^{+2.3\times10^{-4}}_{-4.3\times10^{-5}}$	0.09815	$0.11^{+0.003}_{-0.007}$	0.13

Table B.16: Table of the parameters of the model CCPVP1 for `APEC` , same as B.1.

Region	T_{obs} keV	T_{Fit} keV	Z_{obs} $Z_{\odot}$	z_{obs}	z_{fit}	$N_{0,\,obs}$ $[10^{-4}]\,cm^{-5}$	$N_{0,\,fit}$ $[10^{-4}]\,cm^{-5}$
1R	$5.86^{+0.10}_{-0.1}$	5.91	$0.29^{+0.01}_{-0.01}$	$0.101973^{+4.5\times10^{-6}}_{-2.5\times10^{-6}}$	0.10197	$26.1^{+0.12}_{-0.11}$	26.9
1B	$5.97^{+0.10}_{-0.1}$	5.91	$0.29^{+0.01}_{-0.01}$	$0.098104^{+1.4\times10^{-6}}_{-8.1\times10^{-6}}$	0.0981	$26.9^{+0.11}_{-0.11}$	26.9
2R	$4.6^{+0.3}_{-0.3}$	4.82	$0.34^{+0.06}_{-0.04}$	$0.10119^{+3.5\times10^{-5}}_{-2.0\times10^{-5}}$	0.10128	$1.62^{+0.03}_{-0.03}$	1.64
2B	$4.82^{+0.31}_{-0.34}$	4.82	$0.29^{+0.04}_{-0.05}$	$0.0987^{+6.64\times10^{-5}}_{-1.13\times10^{-5}}$	0.0988	$1.63^{+0.02}_{-0.02}$	1.64
3R	$4.41^{+0.27}_{-0.22}$	4.34	$0.30^{+0.05}_{-0.03}$	$0.101023^{+1.3\times10^{-5}}_{-3.4\times10^{-5}}$	0.10104	$1.3^{+0.03}_{-0.03}$	1.3
3B	$4.33^{+0.15}_{-0.34}$	4.34	$0.30^{+0.05}_{-0.03}$	$0.098960^{+2.3\times10^{-6}}_{-4.3\times10^{-5}}$	0.09896	$1.28^{+0.02}_{-0.02}$	1.3
4R	$3.89^{+0.72}_{-0.55}$	3.62	$0.216^{+0.12}_{-0.08}$	$0.10069^{+3.9\times10^{-4}}_{-7.9\times10^{-5}}$	0.10073	$0.24^{+0.01}_{-0.01}$	0.2
4B	$3.61^{+0.37}_{-0.5}$	3.62	$0.29^{+0.10}_{-0.11}$	$0.09926^{+6.43\times10^{-5}}_{-3.08\times10^{-5}}$	0.09927	$0.24^{+0.02}_{-0.01}$	0.2
5R	$3.34^{+0.86}_{-0.71}$	3.15	$0.33^{+0.34}_{-0.13}$	$0.100841^{+9.3\times10^{-5}}_{-3.1\times10^{-4}}$	0.10056	$0.068^{+0.006}_{-0.006}$	0.065
5B	$3.88^{+1.18}_{-0.98}$	3.15	$0.29^{+0.17}_{-0.24}$	$0.099446^{+4.4\times10^{-4}}_{-3.7\times10^{-4}}$	0.09944	$0.060^{+0.011}_{-0.007}$	0.065

Table B.17: Table of the parameters of the model CCPVP2A for `APEC`, same as B.1.

Region	T_{obs} keV	T_{Fit} keV	Z_{obs} $Z_{\odot}$	z_{obs}	z_{fit}	$N_{0,\,obs}$ $[10^{-4}]\,cm^{-5}$	$N_{0,\,fit}$ $[10^{-4}]\,cm^{-5}$
1R	$5.62^{+0.08}_{-0.07}$	5.58	$0.31^{+0.009}_{-0.009}$	$0.101909^{+5.3\times10^{-6}}_{-6.4\times10^{-6}}$	0.10191	$39.2^{+0.16}_{-0.15}$	39.3
1B	$5.53^{+0.08}_{-0.08}$	5.58	$0.29^{+0.009}_{-0.009}$	$0.9808^{+5.4\times10^{-6}}_{-1.2\times10^{-6}}$	0.09809	$39.1^{+0.19}_{-0.26}$	39.3
2R	$4.23^{+0.21}_{-0.32}$	4.47	$0.29^{+0.04}_{-0.04}$	$0.1011^{+4.0\times10^{-6}}_{-2.6\times10^{-5}}$	0.1012	$3.28^{+0.03}_{-0.03}$	3.3
2B	$4.65^{+0.27}_{-0.33}$	4.47	$0.24^{+0.03}_{-0.04}$	$0.0988^{+2.1\times10^{-5}}_{-4.9\times10^{-5}}$	0.0988	$3.31^{+0.03}_{-0.02}$	3.3
3R	$3.95^{+0.21}_{-0.19}$	3.99	$0.28^{+0.04}_{-0.04}$	$0.10102^{+1.1\times10^{-5}}_{-3.4\times10^{-5}}$	0.10101	$1.55^{+0.04}_{-0.05}$	1.53
3B	$3.92^{+0.20}_{-0.18}$	3.99	$0.34^{+0.04}_{-0.04}$	$0.099^{+1.9\times10^{-6}}_{-4.1\times10^{-5}}$	0.09899	$1.49^{0.05}_{-0.03}$	1.53
4R	$3.00^{+0.54}_{-0.32}$	3.26	$0.23^{+0.08}_{-0.14}$	$0.1009^{+3.9\times10^{-4}}_{-4.2\times10^{-5}}$	0.1007	$0.18^{+0.02}_{-0.01}$	0.17
4B	$3.25^{+0.35}_{-0.57}$	3.26	$0.42^{+0.18}_{-0.11}$	$0.0992^{+6.8\times10^{-5}}_{-9.1\times10^{-5}}$	0.0993	$0.16^{+0.001}_{0.02}$	0.17
5R	$2.54^{+1.1}_{-0.57}$	2.76	$0.19^{+0.25}_{-0.14}$	$0.10028^{+5.2\times10^{-4}}_{-5.5\times10^{-4}}$	0.10054	$0.0046^{+0.006}_{-0.014}$	0.0036
5B	$2.74^{+0.55}_{-0.71}$	2.76	$0.29^{+0.23}_{-0.19}$	$0.09953^{+2.5\times10^{-4}}_{-2.5\times10^{-4}}$	0.09946	$0.0035^{+0.0005}_{-0.0004}$	0.0036

Table B.18: Table of the parameters of the model CCPVP2B for `APEC` , same as B.1.

Appendix C

Appendix

C.1 Bapec Fitting parameters

In this section we present the fitting value of the `bapec` models. We are interested in the centroid shift of the 6.7 keV line and the line broadening due to the dispersion of velocity in the line of sight. All errors are executed with a confidence range of 3σ. The main results are presented in section (5.4). We use the same convention of naming the regions as what it is done in the appendix (B.1). The metallicity is set to $0.3\,Z_{\odot}$ and it is not reported in table and the normalization parameter N is in $[10^{-4}]$ scale and it is not reported in table unlike what we did in appendix (B.1).

Region	T_{obs} keV	T_{Fit} keV	Z_{obs} $Z_\odot$	z_{obs}	z_{fit}	σ_{obs} km/s	σ_{fit} km/s	$N_{0,\,obs}$ cm^{-5}	$N_{0,\,fit}$ cm^{-5}
1R	$7.5^{+0.12}_{-0.12}$	7.5	$0.30^{+0.01}_{-0.01}$	$0.100602^{+2.13\times10^{-5}}_{-2.09\times10^{-5}}$	0.10061	104^{+16}_{-33}	84	$13^{+0.06}_{-0.05}$	13
1B	$7.5^{+0.12}_{-0.12}$	7.5	$0.29^{+0.01}_{-0.01}$	$0.099401^{+2.01\times10^{-5}}_{-2.05\times10^{-5}}$	0.09939	65^{+23}_{-16}	84	$13.1^{+0.05}_{-0.06}$	13
2R	$7.36^{+0.22}_{-0.42}$	7.5	$0.37^{+0.02}_{-0.04}$	$0.100587^{+1.3\times10^{-4}}_{-7.2\times10^{-5}}$	0.10059	$0.05^{+32}_{-0.005}$	78	$1.78^{+0.02}_{-0.03}$	1.88
2B	$8.36^{+0.59}_{-0.49}$	7.5	$0.27^{+0.04}_{-0.03}$	$0.09938^{+9\times10^{-5}}_{-1\times10^{-4}}$	0.0994	100^{+37}_{-41}	78	$1.78^{+0.03}_{-0.02}$	1.88
3R	$7.35^{+0.35}_{-0.33}$	7.5	$0.35^{+0.03}_{-0.03}$	$0.100625^{+7.59\times10^{-5}}_{-3.9\times10^{-5}}$	0.10057	62^{+26}_{-39}	73	$1.02^{+0.02}_{-0.02}$	1
3B	$8.12^{+0.36}_{-0.37}$	7.5	$0.25^{+0.03}_{-0.02}$	$0.09944^{+9.71\times10^{-5}}_{-6.7\times10^{-5}}$	0.09943	88^{+31}_{-31}	73	$0.99^{+0.02}_{-0.02}$	1
4R	$6.57^{+0.58}_{-0.36}$	7.5	$0.28^{+0.04}_{-0.04}$	$0.100598^{+6\times10^{-5}}_{-1\times10^{-4}}$	0.10054	$0.26^{+57}_{-0.26}$	41	$0.7^{+0.02}_{-0.02}$	0.68
4B	$7.5^{+0.46}_{-0.59}$	7.5	$0.3^{+0.03}_{-0.05}$	$0.09946^{+1\times10^{-4}}_{-1\times10^{-4}}$	0.09946	41^{+56}_{-41}	41	$0.69^{+0.01}_{-0.01}$	0.68
5R	$7.27^{+0.50}_{-0.54}$	7.5	$0.39^{+0.06}_{-0.05}$	$0.10053^{+7.67\times10^{-5}}_{-7.7\times10^{-5}}$	0.10051	$0.04^{+61}_{-0.04}$	7	$0.43^{+0.006}_{-0.004}$	0.43
5B	$7.06^{0.62}_{-0.61}$	7.5	$0.25^{+0.04}_{-0.04}$	$0.09955^{+6.8\times10^{-5}}_{-1.8\times10^{-4}}$	0.09949	66^{+42}_{-66}	7	$0.44^{+0.01}_{-0.01}$	0.43

Table C.1: Table of the parameters of the IOVP1 model for `bapec` with temperatures in keV, thermal broadening in km/s, density and redshift as the value obtained by the best fit model and the values that was set.

Region	T_{obs} keV	T_{Fit} keV	Z_{obs} $Z_\odot$	z_{obs}	z_{fit}	σ_{obs} km/s	σ_{fit} km/s	$N_{0,\,obs}$ cm^{-5}	$N_{0,\,fit}$ cm^{-5}
1R	$7.67^{+0.13}_{-0.13}$	7.5	$0.28^{+0.01}_{-0.01}$	$0.10065^{+7.6\times10^{-5}}_{-7.3\times10^{-5}}$	0.10058	320^{+19}_{-17}	310	$13^{+0.08}_{-0.08}$	13.4
1B	$7.39^{+0.13}_{-0.13}$	7.5	$0.30^{+0.01}_{-0.01}$	$0.09949^{+5.8\times10^{-5}}_{-7.3\times10^{-5}}$	0.09942	296^{+15}_{-16}	310	$12.9^{+0.08}_{-0.08}$	13.4
2R	$7.19^{+0.49}_{-0.50}$	7.5	$0.27^{+0.04}_{-0.03}$	$0.10034^{+1\times10^{-4}}_{-1\times10^{-4}}$	0.10036	175^{+50}_{-40}	188	$1.87^{+0.02}_{-0.02}$	1.88
2B	$7.62^{+0.47}_{-0.46}$	7.5	$0.30^{+0.04}_{-0.04}$	$0.09962^{+9\times10^{-5}}_{-1\times10^{-4}}$	0.09964	126^{+30}_{-29}	188	$1.89^{+0.03}_{-0.03}$	1.88
3R	$7.62^{+0.33}_{-0.32}$	7.5	$0.29^{+0.02}_{-0.02}$	$0.100220^{+9.7\times10^{-5}}_{-9.14\times10^{-5}}$	0.10029	144^{+29}_{-23}	143	$0.99^{+0.02}_{-0.02}$	1.0
3B	$7.92^{+0.34}_{-0.37}$	7.5	$0.27^{+0.03}_{-0.02}$	$0.099790^{+4.76\times10^{-5}}_{-1.2\times10^{-4}}$	0.09971	103^{+25}_{-31}	143	$1^{+0.02}_{-0.02}$	1.0
4R	$7.99^{+0.29}_{-0.57}$	7.5	$0.33^{+0.04}_{-0.04}$	$0.10021^{+9\times10^{-5}}_{-7\times10^{-5}}$	0.10020	$0.02^{+66}_{-0.03}$	61	$0.64^{+0.007}_{-0.009}$	0.67
4B	$7.15^{+0.54}_{-0.49}$	7.5	$0.25^{+0.04}_{-0.03}$	$0.09982^{+7\times10^{-5}}_{-1\times10^{-4}}$	0.0998	70^{+57}_{-42}	61	$0.68^{+0.01}_{-0.01}$	0.67
5R	$6.84^{+0.43}_{-0.35}$	7.5	$0.29^{+0.05}_{-0.04}$	$0.100276^{+1\times10^{-4}}_{-6.70\times10^{-5}}$	0.10016	$0.008^{-0.008}_{+32}$	9	$0.41^{+0.01}_{-0.009}$	0.42
5B	$7.16^{+0.58}_{-0.68}$	7.5	$0.31^{+0.05}_{-0.04}$	$0.099794^{+9.3\times10^{-5}}_{-9.1\times10^{-5}}$	0.09984	$0.003^{-0.003}_{+64}$	9	$0.43^{+0.007}_{-0.007}$	0.42

Table C.2: Table of the parameters of the IOVP2A model for `bapec`, same as C.1.

Region	T_{obs} keV	T_{Fit} keV	Z_{obs} $Z_{\odot}$	z_{obs}	z_{fit}	σ_{obs} km/s	σ_{fit} km/s	$N_{0,\,obs}$ cm^{-5}	$N_{0,\,fit}$ cm^{-5}
1R	$7.52^{+0.13}_{-0.13}$	7.5	$0.29^{+0.01}_{-0.01}$	$0.100604^{+1\times10^{-4}}_{-7.7\times10^{-5}}$	0.10068	385^{+26}_{-24}	400	$13^{+0.08}_{-0.08}$	13.2
1B	$7.49^{+0.13}_{-0.13}$	7.5	$0.29^{+0.01}_{-0.01}$	$0.099288^{+8.3\times10^{-5}}_{-1.1\times10^{-4}}$	0.09932	400^{+23}_{-24}	400	$13.2^{+0.08}_{-0.08}$	13.2
2R	$7.31^{+0.32}_{-0.31}$	7.5	$0.29^{+0.02}_{-0.02}$	$0.10052^{+2\times10^{-4}}_{-1.7\times10^{-4}}$	0.10041	367^{+54}_{-48}	317.858	$2.34^{+0.03}_{-0.03}$	2.37
2B	$7.53^{+0.31}_{-0.30}$	7.5	$0.32^{+0.03}_{-0.0}$	$0.099484^{+1.8\times10^{-4}}_{-1.1\times10^{-4}}$	0.09959	298^{+40}_{-37}	317	$2.31^{+0.03}_{-0.03}$	2.37
3R	$7.74^{+0.35}_{-0.34}$	7.5	$0.32^{+0.03}_{-0.03}$	$0.100330^{+1.2\times10^{-4}}_{-7.2\times10^{-5}}$	0.10034	167^{+28}_{-27}	170	$1.87^{+0.03}_{-0.03}$	1.89
3B	$7.10^{+0.33}_{-0.33}$	7.5	$0.25^{+0.02}_{-0.02}$	$0.099544^{+1.4\times10^{-4}}_{-8.6\times10^{-5}}$	0.09966	164^{+39}_{-20}	170	$1.91^{+0.01}_{-0.02}$	1.89
4R	$6.14^{+0.31}_{-0.34}$	7.5	$0.29^{+0.03}_{-0.03}$	$0.100274^{+7.6\times10^{-5}}_{-9.9\times10^{-5}}$	0.10024	93^{+27}_{-33}	72	$0.7^{+0.01}_{-0.01}$	0.67
4B	$7.79^{+0.49}_{-0.47}$	7.5	$0.27^{+,0.04}_{-0.03}$	$0.0997971^{+1.3\times10^{-4}}_{-1.2\times10^{-4}}$	0.09976	94^{+54}_{-47}	72	$0.67^{+0.01}_{-0.01}$	0.67
5R	$7.5^{+0.72}_{-0.47}$	7.5	$0.30^{+0.08}_{-0.03}$	$0.100193^{+7.8\times10^{-5}}_{-1.3\times10^{-4}}$	0.10019	$0.96^{+52}_{-0.59}$	10	$0.41^{+0.006}_{-0.007}$	0.42
5B	$7.49^{+0.43}_{-0.78}$	7.5	$0.29^{+0.05}_{-0.05}$	$0.099814^{+8.1\times10^{-5}}_{-1.4\times10^{-4}}$	0.09981	$0.65^{+74}_{-0.5}$	10	$0.42^{+0.01}_{-0.007}$	0.42

Table C.3: Table of the parameters of the IOVP2B model for `bapec`, same as C.1.

Region	T_{obs} keV	T_{Fit} keV	Z_{obs} $Z_{\odot}$	z_{obs}	z_{fit}	σ_{obs} km/s	σ_{fit} km/s	$N_{0,\,obs}$ cm^{-5}	$N_{0,\,fit}$ cm^{-5}
1R	$5.91^{+0.036}_{-0.03}$	5.91	$0.29^{+0.004}_{-0.004}$	$0.10061^{+1.02\times10^{-5}}_{-6.2\times10^{-6}}$	0.10061	78^{+7}_{-10}	90	$65.9^{+0.11}_{-0.10}$	66.6
1B	$5.90^{+0.03}_{-0.03}$	5.91	$0.30^{+0.004}_{-0.004}$	$0.099387^{+7.9\times10^{-6}}_{-8.9\times10^{-6}}$	0.09939	86^{+5}_{-6}	90	$66.5^{+0.20}_{-0.20}$	66.6
2R	$4.86^{+0.14}_{-0.13}$	4.73	$0.29^{+0.02}_{-0.02}$	$0.100607^{+4\times10^{-5}}_{-4\times10^{-5}}$	0.100607	75^{+19}_{-19}	81	$2.89^{+0.05}_{-0.05}$	2.89
2B	$4.74^{+0.19}_{-0.09}$	4.73	$0.29^{+0.01}_{-0.03}$	$0.09947^{+4\times10^{-5}}_{-6\times10^{-5}}$	0.09940	78^{+21}_{-15}	81	$2.83^{+0.02}_{-0.02}$	2.89
3R	$4.09^{+0.09}_{-0.09}$	4.23	$0.26^{+0.019}_{-0.01}$	$0.1006^{+4.3\times10^{-5}}_{-4.1\times10^{-5}}$	0.10059	106^{+24}_{-42}	80	$2.56^{+0.02}_{-0.02}$	2.6
3B	$4.16^{+0.09}_{-0.09}$	4.23	$0.29^{+0.02}_{-0.01}$	$0.099391^{+5.8\times10^{-5}}_{-5.9\times10^{-5}}$	0.09941	120^{+18}_{-17}	80	$2.62^{+0.02}_{-0.02}$	2.6
4R	$3.7^{+0.24}_{-0.24}$	3.47	$0.33^{+0.07}_{-0.05}$	$0.100654^{+9\times10^{-5}}_{-1\times10^{-4}}$	0.10054	87^{+38}_{-33}	50	$0.3^{+0.01}_{-0.01}$	0.32
4B	$3.5^{+0.21}_{-0.17}$	3.47	$0.18^{+0.03}_{-0.03}$	$0.09954^{+1\times10^{-4}}_{-1\times10^{-4}}$	0.09946	$0.007^{+0.007}_{-32}$	50	$0.32^{+0.009}_{-0.008}$	0.32
5R	$3.17^{+0.48}_{-0.35}$	2.95	$0.38^{+0.15}_{-0.11}$	$0.10093^{+5.5\times10^{-4}}_{-5.6\times10^{-4}}$	0.10051	158^{+133}_{-86}	8	$0.056^{+0.006}_{-0.006}$	0.06
5B	$2.54^{+0.42}_{-0.16}$	2.95	$0.29^{+0.076}_{-0.12}$	$0.099534^{+1.4\times10^{-4}}_{-1.9\times10^{-4}}$	0.09949	$0.12^{+63}_{-0.11}$	8	$0.071^{+0.004}_{-0.003}$	0.06

Table C.4: Table of the parameters of the NIOVP1 model for `bapec`, same as C.1.

Region	T_{obs}	T_{Fit}	Z_{obs}	z_{obs}	z_{fit}	σ_{obs}	σ_{fit}	$N_{0,\,obs}$	$N_{0,\,fit}$
	keV	keV	$Z_{\odot}$			km/s	km/s	cm^{-5}	cm^{-5}
1R	$5.99^{+0.04}_{-0.04}$	5.94	$0.30^{+0.004}_{-0.004}$	$0.10064^{+3.09\times10^{-5}}_{-3.7\times10^{-5}}$	0.1006	373^{+8}_{-8}	370	$66.9^{+0.20}_{-0.20}$	67.5
1B	$5.92^{+0.04}_{-0.03}$	5.94	$0.29^{+0.004}_{-0.004}$	$9.9418^{+3.21\times10^{-5}}_{-3.7\times10^{-5}}$	0.0994	379^{+8}_{-8}	370	$67.1^{+0.20}_{-0.20}$	67.5
2R	$4.91^{+0.14}_{-0.14}$	4.75	$0.31^{+0.02}_{-0.02}$	$0.100411^{+9\times10^{-5}}_{-1\times10^{-4}}$	0.10039	241^{+30}_{-27}	214	$2.84^{+0.05}_{-0.05}$	2.8
2B	$4.54^{+0.13}_{-0.13}$	4.75	$0.26^{+0.02}_{-0.01}$	$0.09954^{+7\times10^{-5}}_{-1\times10^{-4}}$	0.09961	183^{+26}_{-24}	214	$2.76^{+0.04}_{-0.04}$	2.8
3R	$4.21^{+0.10}_{-0.09}$	4.24	$0.25^{+0.01}_{-0.01}$	$0.10028^{+8\times10^{-5}}_{-5.4\times10^{-5}}$	0.10031	139^{+17}_{-17}	171	$2.54^{+0.04}_{-0.04}$	2.65
3B	$4.42^{+0.13}_{-0.12}$	4.24	$0.30^{+0.02}_{-0.02}$	$9.9798^{+7.9\times10^{-5}}_{-9.6\times10^{-5}}$	0.09969	200^{+26}_{-24}	171	$2.7^{+0.04}_{-0.04}$	2.65
4R	$3.43^{+0.18}_{-0.16}$	3.47	$0.26^{+0.05}_{-0.04}$	$0.10005^{+1\times10^{-4}}_{-3\times10^{-4}}$	0.10022	89^{+78}_{-89}	76	$0.33^{+0.01}_{-0.01}$	0.31
4B	$3.76^{+0.20}_{-0.19}$	3.47	$0.28^{+0.04}_{-0.03}$	$0.09988^{+1\times10^{-4}}_{-9\times10^{-5}}$	0.09978	89^{+39}_{-35}	76	$0.29^{+0.01}_{-0.01}$	0.31
5R	$3.15^{+0.44}_{-0.28}$	2.94	$0.38^{+0.13}_{-0.10}$	$0.10028^{+1.1\times10^{-4}}_{-1.8\times10^{-4}}$	0.10016	$0.0002^{+32}_{-0.0002}$	10.5	$0.06^{+0.003}_{-0.003}$	0.006
5B	$2.9^{+0.38}_{-0.32}$	2.94	$0.22^{+0.11}_{-0.07}$	$9.9978^{+4\times10^{-4}}_{-4\times10^{-4}}$	0.09984	79^{+120}_{-79}	10.5	$0.006^{+0.008}_{-0.007}$	0.006

Table C.5: Table of the parameters of the NIOVP2A model for `bapec` , same as C.1.

Region	T_{obs}	T_{Fit}	Z_{obs}	z_{obs}	z_{fit}	σ_{obs}	σ_{fit}	$N_{0,\,obs}$	$N_{0,\,fit}$
	keV	keV	$Z_{\odot}$			km/s	km/s	cm^{-5}	cm^{-5}
1R	$5.88^{+0.04}_{-0.04}$	5.96	$0.29^{+0.004}_{-0.004}$	$0.100657^{+4.9\times10^{-5}}_{-4.01\times10^{-5}}$	0.10071	472^{+12}_{-11}	470	$65.2^{+0.20}_{-0.20}$	64.7
1B	$5.98^{+0.04}_{-0.04}$	5.96	$0.29^{+0.005}_{-0.005}$	$0.099284^{+4.7\times10^{-5}}_{-4.5\times10^{-5}}$	0.09929	486^{+12}_{-12}	470	$63.9^{+0.20}_{-0.20}5$	64.7
2R	$4.66^{+0.09}_{-0.09}$	4.71	$0.30^{+0.01}_{-0.01}$	$0.100578^{+1.6\times10^{-4}}_{-1.7\times10^{-4}}$	0.100449	358^{+28}_{-26}	365	$5.72^{+0.06}_{-0.06}$	5.72
2B	$4.53^{+0.09}_{-0.09}$	4.71	$0.26^{+0.01}_{-0.01}$	$0.099565^{+2.1\times10^{-4}}_{-1.8\times10^{-4}}$	0.099551	353^{+32}_{-29}	365	$5.88^{+0.07}_{-0.07}$	5.72
3R	$4.37^{+0.12}_{-0.10}$	4.28	$0.30^{+0.02}_{-0.02}$	$0.10044^{+6.2\times10^{-5}}_{-9.5\times10^{-5}}$	0.10037	187^{+17}_{-22}	202	$2.73^{+0.04}_{-0.04}$	2.83
3B	$4.27^{+0.09}_{-0.10}$	4.28	$0.29^{+0.02}_{-0.01}$	$0.0998^{+1.7\times10^{-5}}_{-1.5\times10^{-4}}$	0.09963	196^{+22}_{-20}	202	$2.80^{+0.05}_{-0.04}$	2.83
4R	$3.55^{+0.21}_{-0.20}$	3.51	$0.32^{+0.05}_{-0.04}$	$0.100301^{+1.8\times10^{-4}}_{-8.7\times10^{-5}}$	0.10026	99^{+38}_{-39}	90	$0.31^{+0.01}_{-0.01}$	0.32
4B	$3.76^{+0.23}_{-0.20}$	3.51	$0.23^{+0.04}_{-0.03}$	$0.099777^{+1.1\times10^{-4}}_{-7.3\times10^{-5}}$	0.09974	$1.42^{+61}_{-1.42}$	90	$0.32^{+0.01}_{-0.007}$	0.32
5R	$3.94^{+0.65}_{-0.49}$	2.98	$0.46^{+0.17}_{-0.13}$	$0.10026^{+1.1\times10^{-4}}_{-2.5\times10^{-4}}$	0.1002	48^{+72}_{-48}	12	$0.05^{+0.006}_{-0.005}$	0.06
5B	$3.40^{+0.45}_{-0.29}$	2.98	$0.51^{+0.17}_{-0.14}$	$0.099520^{+4.4\times10^{-4}}_{-4.3\times10^{-4}}$	0.0998	125^{+263}_{-88}	12	$0.05^{+0.005}_{-0.005}$	0.06

Table C.6: Table of the parameters of the NIOVP2B model for `bapec` , same as C.1.

Region	T_{obs} keV	T_{Fit} keV	Z_{obs} $Z_{\odot}$	z_{obs}	z_{fit}	σ_{obs} km/s	σ_{fit} km/s	$N_{0,\,obs}$ cm^{-5}	$N_{0,\,fit}$ cm^{-5}
1R	$5.37^{+0.02}_{-0.02}$	5.36	$0.29^{+0.003}_{-0.003}$	$0.10061^{+6.6\times10^{-6}}_{-5.1\times10^{-6}}$	0.100612	91^{+4}_{-4}	87	$19.1^{+0.31}_{-0.31}$	12.1
1B	$5.35^{+0.02}_{-0.02}$	5.36	$0.30^{+0.003}_{-0.003}$	$0.099380^{+3.3\times10^{-6}}_{-1\times10^{-5}}$	0.09938	78^{+4}_{-5}	87	$19.1^{+0.32}_{-0.34}$	12.1
2R	$4.2^{+0.09}_{-0.09}$	4.18	$0.30^{+0.02}_{-0.01}$	$0.10064^{+6\times10^{-5}}_{-3\times10^{-5}}$	0.10061	107^{+17}_{-14}	83	$3.06^{+0.05}_{-0.05}$	3.1
2B	$4.18^{+0.09}_{-0.09}$	4.18	$0.31^{+0.02}_{-0.01}$	$0.0994^{+3\times10^{-5}}_{-7\times10^{-5}}$	0.0994	104^{+18}_{-20}	83	$3.06^{+0.05}_{-0.05}$	3.1
3R	$3.52^{+0.08}_{-0.08}$	3.68	$0.28^{+0.02}_{-0.01}$	$0.10056^{+7\times10^{-5}}_{-8\times10^{-5}}$	0.10059	62^{+16}_{-17}	80	$2.67^{+0.005}_{-0.05}$	2.69
3B	$3.59^{+0.08}_{-0.08}$	3.68	$0.31^{+0.02}_{-0.02}$	$0.099442^{+6.07\times10^{-5}}_{-4\times10^{-5}}$	0.099408	75^{+17}_{-15}	80	$2.62^{+0.002}_{-0.02}$	2.69
4R	$3.0^{+0.14}_{-0.32}$	2.91	$0.40^{+0.13}_{-0.06}$	$0.10051^{+1\times10^{-4}}_{-1\times10^{-4}}$	0.10055	$0.08^{+74}_{-0.09}$	53	$0.16^{+0.01}_{-0.007}$	0.18
4B	$3.25^{+0.25}_{-0.24}$	2.91	$0.51^{+0.12}_{-0.09}$	$0.09957^{+1\times10^{-4}}_{-2\times10^{-4}}$	0.0995	93^{+43}_{-63}	53	$0.14^{+0.01}_{-0.01}$	0.18
5R	$2.18^{+0.40}_{-0.23}$	2.36	$0.52^{+0.22}_{-0.21}$	$0.10065^{+2\times10^{-4}}_{-2.7\times10^{-4}}$	0.100516	$0.22^{+88}_{-0.22}$	9	$0.021^{+0.002}_{-0.003}$	0.02
5B	$1.99^{+0.43}_{-0.31}$	2.36	$0.23^{+0.20}_{-0.10}$	$0.09958^{+4.1\times10^{-4}}_{-1.4\times10^{-4}}$	0.099484	12^{+334}_{-12}	9	$0.025^{+0.008}_{-0.006}$	0.02

Table C.7: Table of the parameters of the CCOVP1 model for `bapec`, same as C.1.

Region	T_{obs} keV	T_{Fit} keV	Z_{obs} $Z_{\odot}$	z_{obs}	z_{fit}	σ_{obs} km/s	σ_{fit} km/s	$N_{0,\,obs}$ cm^{-5}	$N_{0,\,fit}$ cm^{-5}
1R	$5.58^{+0.03}_{-0.03}$	5.57	$0.29^{+0.003}_{-0.003}$	$0.10061^{+2.9\times10^{-5}}_{-2.9\times10^{-5}}$	0.1006	398^{+7}_{-7}	390	$9.9^{+0.25}_{-0.25}$	10
1B	$5.54^{+0.03}_{-0.03}$	5.57	$0.29^{+0.003}_{-0.003}$	$0.099403^{+2.3\times10^{-5}}_{-3.5\times10^{-5}}$	0.0994	385^{+6}_{-7}	390	$10^{+0.25}_{-0.25}$	10
2R	$4.76^{+0.13}_{-0.13}$	4.38	$0.32^{+0.02}_{-0.02}$	$0.10032^{+5\times10^{-5}}_{-1\times10^{-4}}$	0.10039	192^{+21}_{-21}	218	$2.8^{+0.04}_{-0.04}$	3.0
2B	$4.20^{+0.09}_{-0.09}$	4.38	$0.30^{+0.02}_{-0.01}$	$0.09958^{+1.5\times10^{-4}}_{-1.4\times10^{-4}}$	0.09961	178^{+23}_{-21}	218	$3.04^{+0.05}_{-0.05}$	3.0
3R	$3.88^{+0.09}_{-0.09}$	3.88	$0.31^{+0.02}_{-0.02}$	$0.10026^{+6.2\times10^{-5}}_{-1.1\times10^{-4}}$	0.10031	206^{+23}_{-23}	176	$2.75^{+0.05}_{-0.04}$	2.75
3B	$3.77^{+0.09}_{-0.09}$	3.88	$0.27^{+0.02}_{-0.01}$	$0.09968^{+1.6\times10^{-4}}_{-1.1\times10^{-4}}$	0.09969	176^{+42}_{-37}	176	$2.76^{+0.05}_{-0.05}$	2.75
4R	$3.12^{+0.22}_{-0.22}$	3.10	$0.32^{+0.09}_{-0.06}$	$0.1002^{+1\times10^{-4}}_{-1\times10^{-4}}$	0.10022	32^{+61}_{-32}	79	$0.2^{+0.01}_{-0.01}$	0.21
4B	$3.22^{+0.26}_{-0.26}$	3.10	$0.41^{+0.12}_{-0.10}$	$0.0994^{+5\times10^{-4}}_{-5\times10^{-4}}$	0.09978	297^{+161}_{-170}	79	$0.19^{+0.01}_{-0.01}$	0.21
5R	$2.57^{+0.38}_{-0.26}$	2.55	$0.62^{+0.26}_{-0.19}$	$0.100258^{+2\times10^{-4}}_{-2.2\times10^{-4}}$	0.10017	87^{+91}_{-87}	11	$0.02^{+0.004}_{-0.003}$	0.003
5B	$2.72^{+0.42}_{-0.37}$	2.55	$0.32^{+0.18}_{-0.13}$	$0.099785^{+8\times10^{-4}}_{-1.0\times10^{-3}}$	0.09983	$0.001^{+128}_{-0.001}$	11	$0.02^{+0.002}_{-0.003}$	0.003

Table C.8: Table of the parameters of the CCOVP2A model for `bapec`, same as C.1.

Region	T_{obs} keV	T_{Fit} keV	Z_{obs} $Z_\odot$	z_{obs}	z_{fit}	σ_{obs} km/s	σ_{fit} km/s	$N_{0,\,obs}$ cm^{-5}	$N_{0,\,fit}$ cm^{-5}
1R	$5.30^{+0.02}_{-0.02}$	5.30	$0.30^{+0.003}_{-0.003}$	$0.10069^{+2.5\times10^{-5}}_{-2.1\times10^{-5}}$	0.10072	378^{+6}_{-5}	383	$12.9^{+0.33}_{-0.33}$	13.1
1B	$5.28^{+0.02}_{-0.02}$	5.30	$0.29^{+0.003}_{-0.003}$	$0.0992462^{+3.4\times10^{-5}}_{-1.6\times10^{-5}}$	0.09928	383^{+6}_{-5}	383	$13.1^{+0.32}_{-0.34}$	13.1
2R	$4.09^{+0.06}_{-0.06}$	4.06	$0.30^{+0.014}_{-0.01}$	$0.10046^{+9.6\times10^{-5}}_{-1.1\times10^{-4}}$	0.100459	401^{+27}_{-26}	381	$6.86^{+0.08}_{-0.08}$	6.93
2B	$4.00^{+0.06}_{-0.06}$	4.06	$0.29^{+0.014}_{-0.01}$	$0.099411^{+1.2\times10^{-4}}_{-8.8\times10^{-5}}$	0.099541	393^{+27}_{-24}	381	$6.95^{+0.08}_{-0.08}$	6.93
3R	$3.55^{+0.09}_{-0.08}$	3.62	$0.28^{+0.02}_{-0.02}$	$0.10045^{+6.6\times10^{-5}}_{-1\times10^{-4}3}$	0.100382	226^{+20}_{-30}	213	$2.64^{+0.05}_{-0.04}$	2.65
3B	$3.53^{+0.09}_{-0.08}$	3.62	$0.28^{+0.02}_{-0.02}$	$0.099607^{+1\times10^{-4}}_{-7.3\times10^{-5}}$	0.099618	200^{+30}_{-27}	213	$2.65^{+0.05}_{-0.05}$	2.65
4R	$2.66^{+0.20}_{-0.20}$	2.84	$0.16^{+0.05}_{-0.04}$	$0.10027^{+2.8\times10^{-4}}_{-1.8\times10^{-4}}$	0.100268	$1.9^{+115}_{-1.9}$	97	$0.18^{+0.01}_{-0.01}$	0.16
4B	$2.77^{+0.22}_{-0.15}$	2.84	$0.35^{+0.08}_{-0.06}$	$0.099544^{+2.4\times10^{-4}}_{-1\times10^{-4}5}$	0.099732	148^{+51}_{-42}	97	$0.15^{+0.01}_{-0.01}$	0.16
5R	$2.28^{+0.50}_{-0.24}$	2.28	$0.30^{+0.27}_{-0.10}$	$0.10031^{+2.7\times10^{-4}}_{-1.3\times10^{-4}}$	0.100202	$0.29^{+87}_{-0.07}$	13	$0.0019^{+0.002}_{-0.002}$	0.001
5B	$2.21^{+0.40}_{-0.32}$	2.28	$0.47^{+0.38}_{-0.15}$	$0.0999491^{+1.3\times10^{-4}}_{-2.2\times10^{-4}}$	0.099798	$0.0006^{+32}_{-0.0006}$	13	$0.0015^{+0.001}_{-0.001}$	0.001

Table C.9: Table of the parameters of the CCOVP2B model for `bapec`, same as C.1.

Region	T_{obs} keV	T_{Fit} keV	Z_{obs} $Z_\odot$	z_{obs}	z_{fit}	σ_{obs} km/s	σ_{fit} km/s	$N_{0,\,obs}$ cm^{-5}	$N_{0,\,fit}$ cm^{-5}
1R	$7.12^{+0.21}_{-0.20}$	7.5	$0.28^{+0.01}_{-0.01}$	$0.10203^{+6.5\times10^{-5}}_{-3.2\times10^{-5}}$	0.10213	291^{+14}_{-14}	303	$5.2^{+0.05}_{-0.05}$	5.13
1B	$7.62^{+0.21}_{-0.21}$	7.5	$0.30^{+0.01}_{-0.01}$	$0.097859^{+3.1\times10^{-5}}_{-6.7\times10^{-5}}$	0.09787	297^{+15}_{-16}	303	$5.13^{+0.05}_{-0.05}$	5.31
2R	$6.7^{+0.63}_{-0.42}$	7.5	$0.32^{+0.06}_{-0.05}$	$0.102476^{+5\times10^{-4}}_{-5\times10^{-4}}$	0.1020	582^{+221}_{-205}	243	$1.41^{+0.02}_{-0.02}$	1.4
2B	$7.34^{+0.63}_{-0.53}$	7.5	$0.35^{+0.06}_{-0.05}$	$0.0977^{+2\times10^{-4}}_{-1\times10^{-4}}$	0.098	250^{+57}_{-48}	243	$1.39^{+0.02}_{-0.02}$	1.4
3R	$8.01^{+0.43}_{-0.42}$	7.5	$0.29^{+0.04}_{-0.03}$	$0.1022^{+1.9\times10^{-4}}_{-1.6\times10^{-4}}$	0.10201	255^{+50}_{-43}	240	$1.30^{+0.02}_{-0.02}$	1.32
3B	$7.75^{+0.42}_{-0.40}$	7.5	$0.31^{+0.04}_{-0.03}$	$0.09816^{+1.5\times10^{-4}}_{-1\times10^{-4}}$	0.09799	259^{+44}_{-40}	240	$1.33^{+0.02}_{-0.04}$	1.32
4R	$8.44^{+0.6}_{-0.59}$	7.5	$0.29^{+0.05}_{-0.05}$	$0.1018^{+8\times10^{-5}}_{-2\times10^{-4}}$	0.1018	127^{+42}_{-52}	135	$0.63^{+0.02}_{-0.01}$	0.59
4B	$7.42^{+0.23}_{-0.23}$	7.5	$0.23^{+0.02}_{-0.02}$	$0.0981^{+2\times10^{-4}}_{-1\times10^{-4}}$	0.0982	212^{+55}_{-59}	135	$0.64^{+0.005}_{-0.004}$	0.59
5R	$7.24^{+0.55}_{-0.50}$	7.5	$0.28^{+0.04}_{-0.04}$	$0.1017^{+8.9\times10^{-5}}_{-7.5\times10^{-5}}$	0.10179	$1.02^{+64}_{-0.03}$	23	$0.47^{+0.01}_{-0.01}$	0.47
5B	$6.98^{+0.53}_{-0.40}$	7.5	$0.32^{+0.05}_{-0.04}$	$0.098205^{+8.7\times10^{-5}}_{-8.5\times10^{-5}}$	0.09821	66^{+38}_{-66}	23	$0.49^{+0.01}_{-0.01}$	0.47

Table C.10: Table of the parameters of the IPVP1 model for `bapec`, same as C.1.

Region	T_{obs} keV	T_{Fit} keV	Z_{obs} $Z_\odot$	z_{obs}	z_{fit}	σ_{obs} km/s	σ_{fit} km/s	$N_{0,\,obs}$ cm^{-5}	$N_{0,\,fit}$ cm^{-5}
1R	$7.20^{+0.18}_{-0.18}$	7.5	$0.29^{+0.01}_{-0.01}$	$0.10225^{+3.1\times10^{-4}}_{-2.6\times10^{-4}}$	0.1019	931^{+83}_{-89}	977	$7.2^{+0.06}_{-0.06}$	7.18
1B	$7.39^{+0.18}_{-0.18}$	7.5	$0.30^{+0.01}_{-0.01}$	$9.8158^{+2.5\times10^{-4}}_{-3.5\times10^{-4}}$	0.0981	843^{+72}_{-72}	977	$7.18^{+0.06}_{-0.06}$	7.18
2R	$8.52^{+1.28}_{-0.62}$	7.5	$0.29^{+0.07}_{-0.05}$	$0.10202^{+6.7\times10^{-4}}_{-7.4\times10^{-4}}$	0.1012	546^{+157}_{-126}	613	$1.47^{+0.02}_{-0.01}$	1.54
2B	$6.65^{+0.55}_{-0.42}$	7.5	$0.24^{+0.04}_{-0.04}$	$0.0982^{+3\times10^{-4}}_{-3\times10^{-4}}$	0.0988	404^{+96}_{-74}	613	$1.53^{+0.02}_{-0.01}$	1.54
3R	$7.02^{+0.44}_{-0.39}$	7.5	$0.33^{+0.05}_{-0.04}$	$0.10110^{+6.4\times10^{-4}}_{-7\times10^{-4}}$	0.100959	790^{+322}_{-189}	468	$1.19^{+0.02}_{-0.06}$	1.28
3B	$8.34^{+0.79}_{-0.42}$	7.5	$0.38^{+0.04}_{-0.04}$	$9.8937^{+2.8\times10^{-4}}_{-3\times10^{-4}}$	0.099041	405^{+71}_{-63}	468	$1.24^{+0.02}_{-0.02}$	1.28
4R	$8.14^{+0.83}_{-0.61}$	7.5	$0.35^{+0.06}_{-0.05}$	$0.1007^{+1\times10^{-4}}_{-1\times10^{-4}}$	0.1006	173^{+46}_{-47}	199	$0.58^{+0.02}_{-0.01}$	0.6
4B	$6.55^{+0.5}_{-0.44}$	7.5	$0.21^{+0.04}_{-0.03}$	$0.0992^{+2\times10^{-4}}_{-2\times10^{-4}}$	0.0994	190^{+73}_{-65}	199	$0.64^{+0.02}_{-0.02}$	0.6
5R	$7.5^{+0.74}_{-0.56}$	7.5	$0.30^{+0.08}_{-0.03}$	$0.10055^{+1.8\times10^{-4}}_{-7.8\times10^{-5}}$	0.100554	28^{+67}_{-28}	28.198	$0.34^{+0.008}_{-0.01}$	0.33
5B	$6.69^{+0.71}_{-0.47}$	7.5	$0.28^{+0.06}_{-0.04}$	$9.9587^{+7.3\times10^{-5}}_{-1.5\times10^{-4}}$	0.099446	$0.007^{+64}_{-0.007}$	28.198	$0.33^{+0.006}_{-0.006}$	0.33

Table C.11: Table of the parameters of the IPVP2A model for `bapec`, same as C.1.

Region	T_{obs} keV	T_{Fit} keV	Z_{obs} $Z_\odot$	z_{obs}	z_{fit}	σ_{obs} km/s	σ_{fit} km/s	$N_{0,\,obs}$ cm^{-5}	$N_{0,\,fit}$ cm^{-5}
1R	$7.63^{+0.18}_{-0.17}$	7.5	$0.31^{+0.01}_{-0.01}$	$0.10207^{+3.9\times10^{-4}}_{-2.7\times10^{-4}}$	0.1018	1073^{+83}_{-90}	1027	$7.41^{+0.06}_{-0.06}$	7.42
1B	$7.58^{+0.18}_{-0.18}$	7.5	$0.30^{+0.02}_{-0.01}$	$0.097948^{+3\times10^{-4}}_{-2.4\times10^{-4}}$	0.0982	1173^{+131}_{-115}	1027	$7.34^{+0.06}_{-0.06}$	7.42
2R	$6.81^{+0.40}_{-0.29}$	7.5	$0.28^{+0.03}_{-0.03}$	$0.101209^{+1.0\times10^{-3}}_{-9.3\times10^{-4}}$	0.1011	763^{+534}_{-248}	827	$1.56^{+0.03}_{-0.03}$	1.53
2B	$8.06^{+0.40}_{-0.40}$	7.5	$0.31^{+0.04}_{-0.03}$	$0.09886^{+1.2\times10^{-4}}_{-1.1\times10^{-4}}$	0.0989	942^{+344}_{-286}	827	$1.47^{+0.02}_{-0.02}$	1.53
3R	$7.77^{+0.44}_{-0.42}$	7.5	$0.33^{+0.04}_{-0.04}$	$0.101249^{+2.6\times10^{-4}}_{-2.4\times10^{-4}}$	0.1009	363^{+78}_{-62}	442	$1.24^{+0.02}_{-0.02}$	1.27
3B	$7.85^{+0.43}_{-0.43}$	7.5	$0.33^{+0.04}_{-0.04}$	$0.0988516^{+3.4\times10^{-4}}_{-4.1\times10^{-4}}$	0.0991	511^{+106}_{-110}	442	$1.24^{+0.02}_{-0.02}$	1.27
4R	$7.29^{+0.62}_{-0.70}$	7.5	$0.27^{+0.05}_{-0.04}$	$0.10053^{+1\times10^{-4}}_{-1.4\times10^{-4}}$	0.10065	145^{+43}_{-42}	187	$0.50^{+0.01}_{-0.01}$	0.49
4B	$8.40^{+0.87}_{-0.64}$	7.5	$0.27^{+0.05}_{-0.05}$	$0.0991800^{+1.7\times10^{-4}}_{-2\times10^{-4}}$	0.09935	172^{+56}_{-49}	187	$0.47^{+0.01}_{-0.01}$	0.49
5R	$7.80^{+0.74}_{-0.73}$	7.5	$0.21^{+0.06}_{-0.05}$	$0.10040^{+1.6\times10^{-4}}_{-1.4\times10^{-4}}$	0.10052	$1.01^{+457}_{-1.01}$	26	$0.32^{+0.01}_{-0.01}$	0.33
5B	$6.89^{+0.53}_{-0.28}$	7.5	$0.43^{+0.07}_{-0.06}$	$0.0994417^{+9.2\times10^{-5}}_{-1.1\times10^{-4}}$	0.09948	69^{+50}_{-63}	26	$0.33^{+0.006}_{-0.006}$	0.33

Table C.12: Table of the parameters of the IPVP2B model for `bapec`, same as C.1.

Region	T_{obs} keV	T_{Fit} keV	Z_{obs} $Z_{\odot}$	z_{obs}	z_{fit}	σ_{obs} km/s	σ_{fit} km/s	$N_{0,\,obs}$ cm^{-5}	$N_{0,\,fit}$ cm^{-5}
1R	$6.07^{+0.09}_{-0.09}$	6.11	$0.28^{+0.01}_{-0.009}$	$0.10227^{+4.4\times10^{-5}}_{-3.7\times10^{-5}}$	0.10221	319^{+10}_{-11}	325	$12.1^{+0.08}_{-0.09}$	12.7
1B	$6.11^{+0.09}_{-0.09}$	6.11	$0.30^{+0.01}_{-0.01}$	$0.097794^{+4.1\times10^{-5}}_{-4.1\times10^{-5}}$	0.09778	302^{+11}_{-10}	325	$12.6^{+0.08}_{-0.08}$	12.7
2R	$4.78^{+0.22}_{-0.22}$	5.13	$0.32^{+0.03}_{-0.03}$	$0.1024^{+1\times10^{-4}}_{-1\times10^{-4}}$	0.1021	245^{+37}_{-33}	275	$1.71^{+0.03}_{-0.03}$	1.73
2B	$5.65^{+0.32}_{-0.30}$	5.13	$0.26^{+0.03}_{-0.03}$	$0.0975^{+2\times10^{-4}}_{-2\times10^{-4}}$	0.0979	260^{+92}_{-59}	275	$1.7^{+0.03}_{-0.03}$	1.73
3R	$4.57^{+0.17}_{-0.16}$	4.72	$0.35^{+0.03}_{-0.02}$	$0.10219^{+1.4\times10^{-4}}_{-1.7\times10^{-4}}$	0.1021	335^{+41}_{-38}	280	$1.03^{+0.02}_{-0.02}$	1.03
3B	$4.62^{+0.17}_{-0.16}$	4.72	$0.26^{+0.02}_{-0.02}$	$0.097609^{+1.8\times10^{-4}}_{-1.6\times10^{-4}}$	0.0979	298^{+50}_{-42}	280	$0.98^{+0.02}_{-0.02}$	1.03
4R	$3.86^{+0.23}_{-0.19}$	4.14	$0.32^{+0.05}_{-0.04}$	$0.1018^{+7\times10^{-5}}_{-2\times10^{-4}}$	0.1019	126^{+34}_{-37}	160	$0.48^{+0.02}_{-0.02}$	0.46
4B	$4.31^{+0.21}_{-0.23}$	4.14	$0.33^{0.05}_{-0.05}$	$0.098^{+1\times10^{-4}}_{1\times10^{-4}}$	0.0981	161^{+64}_{-47}	160	$0.44^{+0.02}_{-0.01}$	0.46
5R	$3.40^{+0.29}_{-0.22}$	3.76	$0.27^{+0.06}_{-0.05}$	$0.101905^{+1.3\times10^{-4}}_{-1.1\times10^{-4}}$	0.10185	56^{+42}_{-56}	27	$0.22^{+0.01}_{-0.01}$	0.21
5B	$3.66^{+0.22}_{-0.31}$	3.76	$0.27^{+0.05}_{-0.06}$	$0.098068^{+1.1\times10^{-4}}_{-1.1\times10^{-4}}$	0.09815	10^{+68}_{-10}	27	$0.22^{+0.01}_{-0.01}$	0.21

Table C.13: Table of the parameters of the NIPVP1 model for `bapec`, same as C.1.

Region	T_{obs} keV	T_{Fit} keV	Z_{obs} $Z_{\odot}$	z_{obs}	z_{fit}	σ_{obs} km/s	σ_{fit} km/s	$N_{0,\,obs}$ cm^{-5}	$N_{0,\,fit}$ cm^{-5}
1R	$6.27^{+0.08}_{-0.08}$	6.28	$0.29^{+0.01}_{-0.01}$	$0.101811^{+1.4\times10^{-4}}_{-1.9\times10^{-4}}$	0.10195	1060^{+56}_{-57}	1120	$19^{+0.11}_{-0.11}$	19.1
1B	$6.18^{+0.07}_{-0.07}$	6.28	$0.30^{+0.01}_{-0.01}$	$0.0981678^{+1.8\times10^{-4}}_{-2.\times10^{-4}}$	0.09805	1062^{+55}_{-51}	1120	$19.1^{+0.11}_{-0.11}$	19.1
2R	$6.42^{+0.34}_{-0.29}$	5.19	$0.32^{+0.04}_{-0.03}$	$0.1016^{+4\times10^{-4}}_{-3\times10^{-4}}$	0.1012	558^{+100}_{-84}	628	$1.64^{+0.03}_{-0.03}$	1.61
2B	$4.95^{+0.24}_{-0.21}$	5.19	$0.30^{+0.03}_{-0.03}$	$0.09801^{+4.1\times10^{-4}}_{-5.5\times10^{-4}}$	0.0987	690^{+128}_{-109}	628	$1.66^{+0.04}_{-0.03}$	1.61
3R	$4.62^{+0.18}_{-0.18}$	4.71	$0.24^{*0.02}_{-0.02}$	$0.101108^{+2.9\times10^{-4}}_{-2.6\times10^{-4}}$	0.10102	580^{+171}_{-132}	541	$1.13^{+0.02}_{-0.02}$	1.18
3B	$4.18^{+0.13}_{-0.13}$	4.71	$0.31^{+0.03}_{-0.02}$	$0.099099^{+2.4\times10^{-4}}_{-2.1\times10^{-4}}$	0.09898	438^{+63}_{-52}	541	$1.19^{+0.03}_{-0.03}$	1.18
4R	$4.09^{+0.21}_{-0.23}$	4.00	$0.39^{+0.05}_{-0.04}$	$0.10087^{+4.1\times10^{-4}}_{-3.8\times10^{-4}}$	0.1007	205^{+44}_{-58}	235	$0.2^{+0.003}_{-0.003}$	0.30
4B	$3.78^{+0.27}_{-0.27}$	4.00	$0.21^{+0.06}_{-0.04}$	$0.09925^{+3\times10^{-4}}_{-4\times10^{-4}}$	0.0993	242^{+104}_{-85}	235	$0.31^{+0.02}_{-0.01}$	0.30
5R	$3.78^{*0.41}_{-0.34}$	3.54	$0.34^{+0.10}_{-0.07}$	$0.100734^{+1\times10^{-4}}_{-1.4\times10^{-4}}$	0.10056	$0.02^{+63}_{-0.0001}$	31	$0.009^{+0.007}_{-0.007}$	0.0099
5B	$3.75^{+0.36}_{-0.33}$	3.54	$0.41^{0.11}_{-0.09}$	$0.099478^{+1.3\times10^{-4}}_{-1.2\times10^{-4}}$	0.09944	$0.008^{-64}_{-0.008}$	31	$0.009^{+0.007}_{-0.007}$	0.0099

Table C.14: Table of the parameters of the NIPVP2A model for `bapec`, same as C.1.

Region	T_{obs}	T_{Fit}	Z_{obs}	z_{obs}	z_{fit}	σ_{obs}	σ_{fit}	$N_{0,\,obs}$	$N_{0,\,fit}$
	keV	keV	$Z_{\odot}$			km/s	km/s	cm^{-5}	cm^{-5}
1R	$6.36^{+0.07}_{-0.08}$	6.27	$0.29^{+0.01}_{-0.01}$	$0.10201^{+1.7\times10^{-4}}_{-1.9\times10^{-4}}$	0.10194	1066^{+48}_{-53}	1100	$19.2^{+0.11}_{-0.11}$	19.3
1B	$6.12^{+0.13}_{-0.13}$	6.27	$0.29^{+0.01}_{-0.01}$	$0.09805^{+2.8\times10^{-4}}_{-3.3\times10^{-4}}$	0.09806	1122^{+102}_{-98}	1100	$19.5^{+0.20}_{-0.19}$	19.3
2R	$5.10^{+0.27}_{-0.26}$	5.12	$0.29^{+0.04}_{-0.04}$	$0.10097^{+4.8\times10^{-4}}_{-5.4\times10^{-4}}$	0.10123	655^{+167}_{-130}	976	$2.65^{+0.08}_{-0.08}$	2.6
2B	$5.23^{+0.28}_{-0.27}$	5.12	$0.30^{+0.046}_{-0.04}$	$0.09866^{+8.1\times10^{-4}}_{-7.5\times10^{-4}}$	0.09877	928^{+235}_{-220}	976	$2.58^{+0.08}_{-0.07}$	2.6
3R	$4.76^{+0.18}_{-0.18}$	4.70	$0.34^{+0.03}_{-0.03}$	$0.10098^{+2.9\times10^{-4}}_{-2.8\times10^{-4}}$	0.10102	579^{+106}_{-89}	539	$1.59^{+0.03}_{-0.03}$	1.6
3B	$4.71^{+0.18}_{-0.18}$	4.70	$0.28^{+0.030}_{-0.02}$	$0.09916^{+3.9\times10^{-4}}_{-3.4\times10^{-4}}$	0.09898	582^{+87}_{-66}	539	$1.6^{+0.03}_{-0.03}$	1.6
4R	$3.80^{+0.25}_{-0.24}$	3.99	$0.28^{+0.06}_{-0.05}$	$0.10105^{+3.9\times10^{-4}}_{-3.5\times10^{-4}}$	0.10072	320^{+95}_{-83}	235	$0.29^{+0.01}_{-0.01}$	0.29
4B	$4.10^{+0.30}_{-0.23}$	3.99	$0.35^{+0.06}_{-0.05}$	$0.09891^{+2.9\times10^{-4}}_{-2.3\times10^{-4}}$	0.09928	264^{+55}_{-55}	235	$0.29^{+0.01}_{-0.01}$	0.29
5R	$3.20^{+0.27}_{-0.25}$	3.53	$0.30^{+0.082}_{-0.06}$	$0.10069^{+1\times10^{-4}}_{-1.1\times10^{-4}}$	0.100558	$0.01^{+32}_{-0.001}$	32	$0.1^{+0.004}_{-0.004}$	0.009
5B	$3.09^{+0.26}_{-0.23}$	3.53	$0.38^{+0.094}_{-0.07}$	$0.09944^{+8.09\times10^{-5}}_{-1.7\times10^{-4}}$	0.099442	$0.004^{+53}_{-0.0004}$	32	$0.1^{+0.005}_{-0.008}$	0.009

Table C.15: Table of the parameters of the NIPVP2B model for `bapec`, same as C.1.

Region	T_{obs}	T_{Fit}	Z_{obs}	z_{obs}	z_{fit}	σ_{obs}	σ_{fit}	$N_{0,\,obs}$	$N_{0,\,fit}$
	keV	keV	$Z_{\odot}$			km/s	km/s	cm^{-5}	cm^{-5}
1R	$5.43^{+0.06}_{-0.06}$	5.56	$0.29^{+0.008}_{-0.007}$	$0.10216^{+3.04\times10^{-5}}_{-3.1\times10^{-5}}$	0.10221	325^{+8}_{-8}	329	$21.5^{+0.14}_{-0.12}$	21.3
1B	$5.63^{+0.07}_{-0.06}$	5.56	$0.30^{+0.008}_{-0.007}$	$0.09780^{+3.1\times10^{-5}}_{-2.8\times10^{-5}}$	0.09779	320^{+8}_{-7}	329	$21.1^{+0.10}_{-0.12}$	21.3
2R	$4.58^{+0.21}_{-0.18}$	4.58	$0.27^{+0.03}_{-0.02}$	$0.1021^{+1\times10^{-4}}_{-4\times10^{-4}}$	0.1021	309^{+62}_{-51}	284	$1.82^{+0.04}_{-0.04}$	1.83
2B	$4.76^{0.22}_{-0.21}$	4.58	$0.27^{+0.03}_{-0.03}$	$0.0976^{+1\times10^{-4}}_{-1\times10^{-4}}$	0.0979	261^{+45}_{-38}	284	$1.79^{+0.04}_{-0.04}$	1.83
3R	$4.20^{+0.13}_{-0.12}$	4.16	$0.28^{+0.02}_{-0.02}$	$0.1021^{+1.6\times10^{-4}}_{-1\times10^{-4}}$	0.10211	256^{+44}_{-35}	291	$1.27^{+0.03}_{-0.03}$	1.29
3B	$4.16^{+0.13}_{-0.12}$	4.16	$0.28^{+0.02}_{-0.02}$	$0.098076^{+1.7\times10^{-4}}_{-1.4\times10^{-4}}$	0.09789	306^{+43}_{-36}	291	$1.19^{+0.03}_{-0.03}$	1.29
4R	$3.88^{+0.27}_{-0.24}$	3.56	$0.32^{+0.06}_{-0.05}$	$0.1018^{+1\times10^{-4}}_{-2\times10^{-4}}$	0.1019	149^{+44}_{-44}	168	$0.34^{+0.01}_{-0.01}$	0.36
4B	$4.17^{+0.34}_{-0.28}$	3.56	$0.35^{+0.06}_{-0.05}$	$0.098^{+1\times10^{-4}}_{-2\times10^{-4}}$	0.0981	119^{+44}_{-42}	168	$0.32^{+0.01}_{-0.01}$	0.36
5R	$2.87^{+0.31}_{-0.23}$	3.17	$0.21^{+0.07}_{-0.05}$	$0.1022^{+2.3\times10^{-4}}_{-4.8\times10^{-4}}$	0.10185	154^{+79}_{-68}	28	$0.14^{+0.01}_{-0.01}$	0.13
5B	$3.35^{+0.33}_{-0.26}$	3.17	$0.28^{+0.09}_{-0.07}$	$0.097965^{+1.6\times10^{-4}}_{-2.5\times10^{-4}}$	0.09815	46^{+70}_{-46}	28	$0.12^{+0.01}_{-0.009}$	0.13

Table C.16: Table of the parameters of the CCPVP1 model for `bapec`, same as C.1.

Region	T_{obs} keV	T_{Fit} keV	Z_{obs} $Z_\odot$	z_{obs}	z_{fit}	σ_{obs} km/s	σ_{fit} km/s	$N_{0,\,obs}$ cm^{-5}	$N_{0,\,fit}$ cm^{-5}
1R	$5.90^{+0.06}_{-0.06}$	5.91	$0.29^{+0.008}_{-0.008}$	$0.102115^{+2\times10^{-4}}_{-1.5\times10^{-4}}$	0.10197	1235^{+47}_{-54}	1187	$26.8^{+0.10}_{-0.10}$	26.9
1B	$5.79^{+0.06}_{-0.06}$	5.91	$0.26^{+0.008}_{-0.008}$	$0.098379^{+1.6\times10^{-4}}_{-1.5\times10^{-4}}$	0.09803	1071^{+49}_{-46}	1187	$27.2^{+0.13}_{-0.13}$	26.9
2R	$5.03^{+0.22}_{-0.21}$	4.82	$0.29^{+0.03}_{-0.03}$	$0.1013^{+5\times10^{-4}}_{-5\times10^{-4}}$	0.1012	698^{+149}_{-160}	699	$1.67^{+0.04}_{0.03}$	1.64
2B	$4.63^{+0.20}_{-0.19}$	4.82	$0.35^{+0.03}_{-0.03}$	$0.0987^{+4\times10^{-4}}_{-4\times10^{-4}}$	0.0988	664^{104}_{-100}	699	$1.63^{+0.03}_{-0.03}$	1.64
3R	$4.26^{+0.16}_{-0.13}$	4.34	$0.28^{+0.02}_{-0.02}$	$0.10132^{+2.5\times10^{-4}}_{-4.3\times10^{-4}}$	0.10104	613^{+87}_{-88}	557	$1.26^{+0.03}_{-0.03}$	1.3
3B	$4.51^{+0.18}_{-0.17}$	4.34	$0.25^{+0.02}_{-0.02}$	$0.099088^{+4.3\times10^{-4}}_{-4.1\times10^{-4}}$	0.09896	611^{+91}_{-84}	557	$1.29^{+0.03}_{-0.03}$	1.3
4R	$3.52^{+0.29}_{-0.34}$	3.62	$0.29^{+0.08}_{-0.06}$	$0.1013^{+3\times10^{-4}}_{-3\times10^{-4}}$	0.1007	248^{+87}_{-66}	244	$0.24^{+0.02}_{-0.01}$	0.23
4B	$3.93^{+0.36}_{-0.32}$	3.62	$0.23^{+0.10}_{-0.06}$	$0.0991^{+1\times10^{-3}}_{-3\times10^{-4}}$	0.0993	225^{+319}_{-95}	244	$0.22^{+0.01}_{-0.01}$	0.23
5R	$3.26^{+0.61}_{-0.34}$	3.15	$0.38^{+0.16}_{-0.11}$	$0.100095^{+3.5\times10^{-4}}_{-2.1\times10^{-4}}$	0.100562	144^{+78}_{-67}	33	$0.05^{+0.007}_{-0.007}$	0.06
5B	$3.79^{+0.61}_{-0.51}$	3.15	$0.51^{+0.16}_{-0.12}$	$0.099368^{+1.2\times10^{-4}}_{-1.4\times10^{-4}}$	0.099438	$0.52^{+69}_{-0.063}$	33	$0.06^{+0.003}_{-0.002}$	0.06

Table C.17: Table of the parameters of the CCPVP2A model for `bapec`, same as C.1.

Region	T_{obs} keV	T_{Fit} keV	Z_{obs} $Z_\odot$	z_{obs}	z_{fit}	σ_{obs} km/s	σ_{fit} km/s	$N_{0,\,obs}$ cm^{-5}	$N_{0,\,fit}$ cm^{-5}
1R	$5.53^{+0.05}_{-0.05}$	5.58	$0.29^{+0.006}_{-0.006}$	$0.10179^{+9.3\times10^{-5}}_{-1.6\times10^{-4}}$	0.10191	1073^{+37}_{-39}	1092	$39.3^{+0.15}_{-0.15}$	39.3
1B	$5.60^{+0.05}_{-0.05}$	5.58	$0.29^{+0.006}_{-0.006}$	$0.09797^{+1.2\times10^{-4}}_{-1.3\times10^{-4}}$	0.09809	1078^{+38}_{-38}	1092	$39.2^{+0.16}_{-0.16}$	39.3
2R	$4.52^{+0.12}_{-0.12}$	4.41	$0.30^{+0.02}_{-0.02}$	$0.10104^{+3.5\times10^{-4}}_{-3.6\times10^{-4}}$	0.10121	1048^{+120}_{-105}	992	$3.29^{+0.05}_{-0.05}$	3.34
2B	$4.53^{+0.12}_{-0.12}$	4.41	$0.30^{+0.02}_{-0.02}$	$0.09877^{+3.2\times10^{-4}}_{-4.2\times10^{-4}}$	0.09879	944^{+90}_{-99}	992	$3.30^{+0.05}_{-0.05}$	3.34
3R	$3.97^{+0.13}_{-0.13}$	3.99	$0.28^{+0.03}_{-0.03}$	$0.10074^{+6\times10^{-4}}_{-5.6\times10^{-4}}$	0.10101	588^{+117}_{-92}	550	$1.57^{+0.03}_{-0.03}$	1.6
3B	$3.87^{+0.12}_{-0.12}$	3.99	$0.32^{+0.03}_{-0.02}$	$0.099001^{+2.2\times10^{-4}}_{-2.1\times10^{-4}}$	0.09899	381^{+71}_{-58}	550	$1.62^{+0.04}_{-0.03}$	1.6
4R	$3.14^{+0.26}_{-0.23}$	3.26	$0.33^{+0.08}_{-0.07}$	$0.10102^{+3.2\times10^{-4}}_{-3.1\times10^{-4}}$	0.1007	247^{+88}_{-68}	244	$0.16^{+0.01}_{-0.01}$	0.17
4B	$2.89^{+0.20}_{-0.21}$	3.26	$0.15^{+0.05}_{-0.03}$	$0.098334^{+3.1\times10^{-4}}_{-2.3\times10^{-4}}$	0.0993	94^{+86}_{-44}	244	$0.21^{+0.01}_{-0.007}$	0.17
5R	$1.79^{+0.16}_{-0.19}$	2.76	$0.52^{+0.23}_{-0.17}$	$0.10052^{+3\times10^{-4}}_{-3.4\times10^{-4}}$	0.100542	241^{+109}_{-172}	32	$0.04^{+0.01}_{-0.007}$	0.003
5B	$2.7^{+0.24}_{-0.35}$	2.76	$0.45^{+0.13}_{-0.17}$	$0.099602^{+2.6\times10^{-4}}_{-1.3\times10^{-4}}$	0.099458	$0.0005^{+64}_{-0.0005}$	32	$0.03^{+0.006}_{-0.002}$	0.003

Table C.18: Table of the parameters of the CCPVP2B model for `bapec`, same as C.1.

Bibliography

ESA Science ATHENA
. `http://www.the-athena-x-ray-observatory.eu/`.

ESA Science, Cosmic Vision Project-Athena
. `http://sci.esa.int/cosmic-vision/54517-athena/`.

ESA Science, Euclid Space Telescope
. `http://sci.esa.int/euclid/`.

NASA, James Webb Telescope
. `https://jwst.nasa.gov/`.

ESA Science, XMM-Newton
. `http://sci.esa.int/xmm-newton/`.

G. O. Abell, Jr. H. G. Corwin, and R. P. Olowin. A catalog of rich clusters of galaxies. *Astrophysical Journal Supplement Series*, 70:1–138, May 1989. doi: 10.1086/191333.

S. Amodeo, S. Mei, S. A. Stanford, J. G. Bartlett, J.-B. Melin, C. R. Lawrence, R.-R. Chary, H. Shim, F. Marleau, and D. Stern. Calibrating the Planck Cluster Mass Scale with Cluster Velocity Dispersions. *ArXiv e-prints*, April 2017.

K. A. Arnaud. XSPEC: The First Ten Years. In G. H. Jacoby and J. Barnes, editors, *Astronomical Data Analysis Software and Systems V*, volume 101 of *Astronomical Society of the Pacific Conference Series*, page 17, 1996.

M. Arnaud, E. Pointecouteau, and G. W. Pratt. The structural and scaling properties of nearby galaxy clusters. II. The M-T relation. *Astronomy and Astrophysics*, 441:893–903, October 2005. doi: 10.1051/0004-6361:20052856.

H. W. Babcock. The rotation of the Andromeda Nebula. *Lick Observatory Bulletin*, 19:41–51, 1939. doi: 10.5479/ADS/bib/1939LicOB.19.41B.

N. A. Bahcall. Clusters and superclusters of galaxies. *ArXiv Astrophysics e-prints*, November 1996.

A. S. Baldi, M. De Petris, F. Sembolini, G. Yepes, L. Lamagna, and E. Rasia. On the coherent rotation of diffuse matter in numerical simulations of clusters of galaxies. *Monthly Notices of the Royal Astronomical Society*, 465:2584–2594, March 2017. doi: 10.1093/mnras/stw2858.

J. M. Bardeen, P. J. Steinhardt, and M. S. Turner. Spontaneous creation of almost scale-free density perturbations in an inflationary universe. *Physical Review D*, 28:679–693, August 1983. doi: 10.1103/PhysRevD.28.679.

M. Bianconi, S. Ettori, and C. Nipoti. Gas rotation in galaxy clusters: signatures and detectability in X-rays. *Monthly Notices of the Royal Astronomical Society*, 434:1565–1575, September 2013. doi: 10.1093/mnras/stt1112.

V. Biffi, K. Dolag, and H. Böhringer. Investigating the velocity structure and X-ray observable properties of simulated galaxy clusters with PHOX. *Monthly Notices of the RAS*, 428:1395–1409, January 2013a. doi: 10.1093/mnras/sts120.

V. Biffi, K. Dolag, and H. Böhringer. Observing simulated galaxy clusters: The prospects of ICM velocity diagnostics. *Astronomische Nachrichten*, 334:317, April 2013b. doi: 10.1002/asna.201211848.

V. Biffi, S. Borgani, G. Murante, E. Rasia, S. Planelles, G. L. Granato, C. Ragone-Figueroa, A. M. Beck, M. Gaspari, and K. Dolag. On the Nature of Hydrostatic Equilibrium in Galaxy Clusters. *Astrophysical Journal*, 827:112, August 2016. doi: 10.3847/0004-637X/827/2/112.

J. Binney and O. Strimpel. Predicting the X-ray brightness distributions of cluster sources - 1. Estimating the potentials. *Monthly Notices of the RAS*, 185: 473–484, November 1978. doi: 10.1093/mnras/185.3.473.

J. Binney and S. Tremaine. *Galactic Dynamics: Second Edition*. Princeton University Press, 2008.

H. Böhringer and N. Werner. X-ray spectroscopy of galaxy clusters: studying astrophysical processes in the largest celestial laboratories. *Astronomy and Astrophysics Reviews*, 18:127–196, February 2010. doi: 10.1007/s00159-009-0023-3.

G. Brunetti and T. W. Jones. Cosmic Rays in Galaxy Clusters and Their Non-thermal Emission. *International Journal of Modern Physics D*, 23:1430007-98, March 2014. doi: 10.1142/S0218271814300079.

S. E. Bryan, S. T. Kay, A. R. Duffy, J. Schaye, C. Dalla Vecchia, and C. M. Booth. The impact of baryons on the spins and shapes of dark matter haloes. *Monthly Notices of the RAS*, 429:3316–3329, March 2013. doi: 10.1093/mnras/sts587.

D. A. Buote and C. R. Canizares. X-Ray Constraints on the Intrinsic Shapes and Baryon Fractions of Five Abell Clusters. *Astrophysical Journal*, 457:565, February 1996. doi: 10.1086/176753.

D. A. Buote and J. C. Tsai. The reliability of X-ray constraints of intrinsic cluster shapes. *Astrophysical Journal*, 439:29–41, January 1995. doi: 10.1086/175148.

A. Burkert. The Structure of Dark Matter Halos in Dwarf Galaxies. *Astrophysical Journal Letters*, 447:L25–L28, July 1995. doi: 10.1086/309560.

A. M. Bykov, E. M. Churazov, C. Ferrari, W. R. Forman, J. S. Kaastra, U. Klein, M. Markevitch, and J. de Plaa. Structures and Components in Galaxy Clusters: Observations and Models. *Space Science Reviews*, 188(1): 141–185, 2015. ISSN 1572-9672. doi: 10.1007/s11214-014-0129-4. URL `http://dx.doi.org/10.1007/s11214-014-0129-4`.

W. Cash. Parameter estimation in astronomy through application of the likelihood ratio. *Astrophysical Journal*, 228:939–947, March 1979. doi: 10.1086/156922.

S. Chandrasekhar. *Ellipsoidal figures of equilibrium*. 1969.

L. Ciotti and G. Bertin. A simple method to construct exact density-potential pairs from a homeoidal expansion. *Astronomy & Astrophysics*, 437:419–427, July 2005. doi: 10.1051/0004-6361:20042123.

P. Coles and F. Lucchin. *Cosmology: The Origin and Evolution of Cosmic Structure, Second Edition*. July 2002.

L. L. Cowie and J. Binney. Radiative regulation of gas flow within clusters of galaxies - A model for cluster X-ray sources. *Astrophysical Journal*, 215: 723–732, August 1977. doi: 10.1086/155406.

S. De Grandi and S. Molendi. Metallicity Gradients in X-Ray Clusters of Galaxies. *The Astrophysical Journal*, 551:153–159, April 2001. doi: 10.1086/320098.

I. De Martino and F. Atrio-Barandela. SZ/X-ray scaling relations using X-ray data and Planck Nominal maps. *Monthly Notices of the RAS*, 461:3222–3232, September 2016. doi: 10.1093/mnras/stw1493.

G. Despali, C. Giocoli, M. Bonamigo, M. Limousin, and G. Tormen. A look into the inside of haloes: a characterization of the halo shape as a function of overdensity in the Planck cosmology. *Monthly Notices of the Royal Astronomical Society*, 466:181–193, April 2017. doi: 10.1093/mnras/stw3129.

K. Dolag, M. Bartelmann, L. Moscardini, F. Perrotta, C. Baccigalupi, M. Meneghetti, and G. Tormen. Properties of Galaxy Clusters in Cosmologies with Dark Energy. *Modern Physics Letters A*, 19:1079–1082, 2004. doi: 10.1142/S0217732304014392.

J. Dubinski and R. G. Carlberg. The structure of cold dark matter halos. *Astrophysical Journal*, 378:496–503, September 1991. doi: 10.1086/170451.

D. Eckert, S. Molendi, F. Gastaldello, and M. Rossetti. X-ray observations of PKS 0745-191 at the virial radius: are we there yet? *Astronomy and Astrophysics*, 529:A133, May 2011. doi: 10.1051/0004-6361/201116575.

S. Ettori. The Astrophysics of galaxy groups and clusters with Athena. In *40th COSPAR Scientific Assembly*, volume 40 of *COSPAR Meeting*, 2014.

S. Ettori, F. Gastaldello, A. Leccardi, S. Molendi, M. Rossetti, D. Buote, and M. Meneghetti. Mass profiles and c-M_{DM} relation in X-ray luminous galaxy clusters. *Astronomy & Astrophysics*, 524:A68, December 2010. doi: 10.1051/0004-6361/201015271.

S. Ettori, A. Donnarumma, E. Pointecouteau, T. H. Reiprich, S. Giodini, L. Lovisari, and R. W. Schmidt. Mass Profiles of Galaxy Clusters from X-ray Analysis. *Space Science Reviews*, 177:119–154, August 2013. doi: 10.1007/s11214-013-9976-7.

A. C. Fabian and P. E. J. Nulsen. Subsonic accretion of cooling gas in clusters of galaxies. *Monthly Notices of the RAS*, 180:479–484, August 1977. doi: 10.1093/mnras/180.3.479.

D. Fabricant, G. Rybicki, and P. Gorenstein. X-ray measurements of the nonspherical mass distribution in the cluster of galaxies A2256. *Astrophysical Journal*, 286:186–195, November 1984. doi: 10.1086/162586.

T. Fang, P. Humphrey, and D. Buote. Rotation and Turbulence of the Hot Intracluster Medium in Galaxy Clusters. *Astrophysical Journal*, 691:1648–1659, February 2009. doi: 10.1088/0004-637X/691/2/1648.

C. S. Frenk, S. D. M. White, G. Efstathiou, and M. Davis. Cold dark matter, the structure of galactic haloes and the origin of the Hubble sequence. *Nature*, 317:595–597, October 1985. doi: 10.1038/317595a0.

S. Ghigna, B. Moore, F. Governato, G. Lake, T. Quinn, and J. Stadel. Dark matter haloes within clusters. *Monthly Notices of the RAS*, 300:146–162, October 1998. doi: 10.1046/j.1365-8711.1998.01918.x.

S. Giodini, L. Lovisari, E. Pointecouteau, S. Ettori, T. H. Reiprich, and H. Hoekstra. Scaling Relations for Galaxy Clusters: Properties and Evolution. *Space Science Reviews*, 177:247–282, August 2013. doi: 10.1007/s11214-013-9994-5.

K. Grainge, S. Borgani, S. Colafrancesco, C. Ferrari, A. Scaife, P. Marchegiani, S. Emritte, and J. Weller. The SKA and Galaxy Cluster Science with the Sunyaev-Zel'dovich Effect. *Advancing Astrophysics with the Square Kilometre Array (AASKA14)*, art. 170, April 2015.

A. H. Guth and S.-Y. Pi. Fluctuations in the new inflationary universe. *Physical Review Letters*, 49:1110–1113, October 1982. doi: 10.1103/PhysRevLett.49.1110.

J. W. Henning, B. Gantner, J. O. Burns, and E. J. Hallman. On the Origin of Cool Core Galaxy Clusters: Comparing X-ray Observations with Numerical Simulations. *Astrophysical Journal*, 697:1597–1620, June 2009. doi: 10.1088/0004-637X/697/2/1597.

H. Hoekstra, M. Bartelmann, H. Dahle, H. Israel, M. Limousin, and M. Meneghetti. Masses of Galaxy Clusters from Gravitational Lensing. *Space Science Reviews*, 177:75–118, August 2013. doi: 10.1007/s11214-013-9978-5.

D. S. Hudson, R. Mittal, T. H. Reiprich, P. E. J. Nulsen, H. Andernach, and C. L. Sarazin. What is a cool-core cluster? a detailed analysis of the cores of the X-ray flux-limited HIFLUGCS cluster sample. *Astronomy and Astrophysics*, 513:A37, April 2010. doi: 10.1051/0004-6361/200912377.

N. A. Inogamov and R. A. Sunyaev. Turbulence in Clusters of Galaxies and X-ray Line Profiles. *Astronomy Letters*, 29:791–824, December 2003. doi: 10.1134/1.1631412.

Y. P. Jing and Y. Suto. The Density Profiles of the Dark Matter Halo Are Not Universal. *Astrophysical Journal, Letter*, 529:L69–L72, February 2000. doi: 10.1086/312463.

S. Kazantzidis, A. V. Kravtsov, A. R. Zentner, B. Allgood, D. Nagai, and B. Moore. The Effect of Gas Cooling on the Shapes of Dark Matter Halos. *Astrophysical Journal, Letter*, 611:L73–L76, August 2004. doi: 10.1086/423992.

A. Klypin, H. Zhao, and R. S. Somerville. ΛCDM-based Models for the Milky Way and M31. I. Dynamical Models. *Astrophysical Journal*, 573:597–613, July 2002. doi: 10.1086/340656.

A. V. Kravtsov, A. Vikhlinin, and D. Nagai. A New Robust Low-Scatter X-Ray Mass Indicator for Clusters of Galaxies. *Astrophysical Journal*, 650:128–136, October 2006. doi: 10.1086/506319.

L. D. Landau and E. M. Lifshitz. *Mechanics*. 1969.

E. T. Lau, D. Nagai, A. V. Kravtsov, A. Vikhlinin, and A. R. Zentner. Constraining Cluster Physics with the Shape of X-Ray Clusters: Comparison of Local X-Ray Clusters Versus ΛCDM Clusters. *Astrophysical Journal*, 755:116, August 2012. doi: 10.1088/0004-637X/755/2/116.

J. Lee, V. Springel, U.-L. Pen, and G. Lemson. Quantifying the cosmic web - I. The large-scale halo ellipticity-ellipticity and ellipticity-direction correlations. *Monthly Notices of the RAS*, 389:1266–1274, September 2008. doi: 10.1111/j.1365-2966.2008.13624.x.

A. Liu, H. Yu, P. Tozzi, and Z.-H. Zhu. A Method to Search for Bulk Motions in the ICM with Chandra CCD Spectra: Application to the Bullet Cluster. *Astrophysical Journal*, 809:27, August 2015. doi: 10.1088/0004-637X/809/1/27.

A. Liu, H. Yu, P. Tozzi, and Z.-H. Zhu. Searching for Bulk Motions in the Intracluster Medium of Massive, Merging Clusters with Chandra CCD Data. *Astrophysical Journal*, 821:29, April 2016. doi: 10.3847/0004-637X/821/1/29.

D. Martizzi and H. Agrusa. Mass modeling of galaxy clusters: quantifying hydrostatic bias and contribution from non-thermal pressure. *ArXiv e-prints*, August 2016.

B. J. Maughan, L. R. Jones, M. Pierre, S. Andreon, M. Birkinshaw, M. N. Bremer, F. Pacaud, T. J. Ponman, I. Valtchanov, and J. Willis. Testing the galaxy cluster mass-observable relations at $z = 1$ with XMM-Newton and Chandra observations of XLSSJ022403.9-041328. *Monthly Notices of the RAS*, 387:998–1006, July 2008. doi: 10.1111/j.1365-2966.2008.13313.x.

M. Meneghetti, E. Rasia, J. Merten, F. Bellagamba, S. Ettori, P. Mazzotta, K. Dolag, and S. Marri. Weighing simulated galaxy clusters using lensing and X-ray. *Astronomy & Astrophysics*, 514:A93, May 2010. doi: 10.1051/0004-6361/200913222.

J. F. Navarro. The Inner Density Cusp of Cold Dark Matter Halos. In S. Ryder, D. Pisano, M. Walker, and K. Freeman, editors, *Dark Matter in Galaxies*, volume 220 of *IAU Symposium*, page 61, July 2004.

J. F. Navarro, C. S. Frenk, and S. D. M. White. The Structure of Cold Dark Matter Halos. *Astrophysical Journal*, 462:563, May 1996. doi: 10.1086/177173.

C. Nipoti, L. Posti, S. Ettori, and M. Bianconi. Magnetorotational instability in galaxy clusters: looking forward to ATHENA. In M. Ehle, editor, *Exploring the Hot and Energetic Universe: The first scientific conference dedicated to the Athena X-ray observatory*, page 42, September 2015.

N. Okabe and G. P. Smith. LoCuSS: weak-lensing mass calibration of galaxy clusters. *Monthly Notices of the RAS*, 461:3794–3821, October 2016. doi: 10.1093/mnras/stw1539.

N. Okabe, M. Takada, K. Umetsu, T. Futamase, and G. P. Smith. LoCuSS: Subaru Weak Lensing Study of 30 Galaxy Clusters. *Publications of the Astronomical Society of Japan*, 62:811–870, June 2010. doi: 10.1093/pasj/62.3.811.

J. H. Oort. Some Problems Concerning the Structure and Dynamics of the Galactic System and the Elliptical Nebulae NGC 3115 and 4494. *The Astrophysical Journal*, 91:273, April 1940. doi: 10.1086/144167.

T. Padmanabhan. Cosmological constant-the weight of the vacuum. *Physics Reports*, 380:235–320, July 2003. doi: 10.1016/S0370-1573(03)00120-0.

G. Panou and D. Delikaraoglou. Expansion of the gravitational potential in triaxial ellipsoidal harmonics. In A. Abbasi and N. Giesen, editors, *EGU General Assembly Conference Abstracts*, volume 14 of *EGU General Assembly Conference Abstracts*, page 1083, April 2012.

P. J. E. Peebles. Large-scale background temperature and mass fluctuations due to scale-invariant primeval perturbations. *Astrophysical Journal, Letter*, 263:L1–L5, December 1982. doi: 10.1086/183911.

J. R. Peterson and A. C. Fabian. X-ray spectroscopy of cooling clusters. *Physics Reports*, 427:1–39, April 2006. doi: 10.1016/j.physrep.2005.12.007.

R. Piffaretti and R. Valdarnini. Total mass biases in X-ray galaxy clusters. *Astronomy and Astrophysics*, 491:71–87, November 2008. doi: 10.1051/0004-6361:200809739.

Planck Collaboration, P. A. R. Ade, N. Aghanim, M. Arnaud, M. Ashdown, J. Aumont, C. Baccigalupi, A. J. Banday, R. B. Barreiro, J. G. Bartlett, and et al. Planck 2015 results. XIII. Cosmological parameters. *Astronomy & Astrophysics*, 594:A13, September 2016. doi: 10.1051/0004-6361/201525830.

W. H. Press and P. Schechter. Formation of Galaxies and Clusters of Galaxies by Self-Similar Gravitational Condensation. *Astrophysical Journal*, 187:425–438, February 1974. doi: 10.1086/152650.

E. Rasia, M. Meneghetti, R. Martino, S. Borgani, A. Bonafede, K. Dolag, S. Ettori, D. Fabjan, C. Giocoli, P. Mazzotta, J. Merten, M. Radovich, and L. Tornatore. Lensing and x-ray mass estimates of clusters (simulations). *New Journal of Physics*, 14(5):055018, May 2012. doi: 10.1088/1367-2630/14/5/055018.

E. Rasia, E. T. Lau, S. Borgani, D. Nagai, K. Dolag, C. Avestruz, G. L. Granato, P. Mazzotta, G. Murante, K. Nelson, and C. Ragone-Figueroa. Temperature Structure of the Intracluster Medium from Smoothed-particle Hydrodynamics and Adaptive-mesh Refinement Simulations. *Astrophysical Journal*, 791: 96, August 2014. doi: 10.1088/0004-637X/791/2/96.

A. Rojas-Niño, J. I. Read, L. Aguilar, and M. Delorme. An efficient positive potential-density pair expansion for modelling galaxies. *Monthly Notices of the Royal Astronomical Society*, 459:3349–3355, July 2016. doi: 10.1093/mnras/stw846.

R. Sadat. Clusters of Galaxies and Mass Estimates. In D. Valls-Gabaud, M. A. Hendry, P. Molaro, and K. Chamcham, editors, *From Quantum Fluctuations to Cosmological Structures*, volume 126 of *Astronomical Society of the Pacific Conference Series*, page 349, September 1997.

B. R. Saliwanchik, T. E. Montroy, K. A. Aird, M. Bayliss, B. A. Benson, L. E. Bleem, S. Bocquet, M. Brodwin, J. E. Carlstrom, C. L. Chang, H. M. Cho, A. Clocchiatti, T. M. Crawford, A. T. Crites, T. de Haan, S. Desai, M. A. Dobbs, J. P. Dudley, R. J. Foley, W. R. Forman, E. M. George, M. D. Gladders, A. H. Gonzalez, N. W. Halverson, J. Hlavacek-Larrondo, G. P. Holder, W. L. Holzapfel, J. D. Hrubes, C. Jones, R. Keisler, L. Knox, A. T. Lee, E. M. Leitch, J. Liu, M. Lueker, D. Luong-Van, A. Mantz, D. P. Marrone, M. McDonald, J. J. McMahon, J. Mehl, S. S. Meyer, L. Mocanu, J. J. Mohr, S. S. Murray, D. Nurgaliev, S. Padin, A. Patej, C. Pryke, C. L. Reichardt, A. Rest, J. Ruel, J. E. Ruhl, A. Saro, J. T. Sayre, K. K. Schaffer, E. Shirokoff, H. G. Spieler, B. Stalder, S. A. Stanford, Z. Staniszewski, A. A. Stark, K. Story, C. W. Stubbs, K. Vanderlinde, J. D. Vieira, A. Vikhlinin, R. Williamson, O. Zahn, and A. Zenteno. Measurement of Galaxy Cluster Integrated Comptonization and Mass Scaling Relations with the South Pole Telescope. *Astrophysical Journal*, 799:137, February 2015. doi: 10.1088/0004-637X/799/2/137.

E. Salvador-Solé, J. Viñas, A. Manrique, and S. Serra. Theoretical dark matter halo density profile. *Monthly Notices of the RAS*, 423:2190–2202, July 2012. doi: 10.1111/j.1365-2966.2012.21066.x.

C. L. Sarazin. *X-ray emission from clusters of galaxies*. 1988.

A. Saro, J. J. Mohr, G. Bazin, and K. Dolag. Toward Unbiased Galaxy Cluster Masses from Line-of-sight Velocity Dispersions. *Astrophysical Journal*, 772:47, July 2013. doi: 10.1088/0004-637X/772/1/47.

M. Schneider, C. S. Frenk, and S. Cole. The Shapes and Alignments of Dark Matter Halos. In *American Astronomical Society Meeting Abstracts #219*, volume 219 of *American Astronomical Society Meeting Abstracts*, page 248.09, January 2012.

M. Sereno and S. Ettori. Comparing masses in literature (CoMaLit) - I. Bias and scatter in weak lensing and X-ray mass estimates of clusters. *Monthly Notices of the RAS*, 450:3633–3648, July 2015. doi: 10.1093/mnras/stv810.

S. Smith. The Mass of the Virgo Cluster. *Astrophysical Journal*, 83:23, January 1936. doi: 10.1086/143697.

J. M. Solanes, A. Manrique, and E. Salvador-Sole. The Structure of Dark Matter Halos. In *American Astronomical Society Meeting Abstracts*, volume 29 of *Bulletin of the American Astronomical Society*, page 1352, December 1997.

R. Stanek, A. E. Evrard, H. Böhringer, P. Schuecker, and B. Nord. The X-Ray Luminosity-Mass Relation for Local Clusters of Galaxies. *Astrophysical Journal*, 648:956–968, September 2006. doi: 10.1086/506248.

R. S. Sutherland and M. A. Dopita. Cooling functions for low-density astrophysical plasmas. *Astrophysical Journal Supplement*, 88:253–327, September 1993. doi: 10.1086/191823.

J.-L. Tassoul. *Stellar Rotation*. July 2007.

P. Tozzi, C. Scharf, and C. Norman. Detection of the Entropy of the Intergalactic Medium: Accretion Shocks in Clusters, Adiabatic Cores in Groups. *Astrophysical Journal*, 542:106–119, October 2000. doi: 10.1086/309500.

R. B. Tully, H. Courtois, Y. Hoffman, and D. Pomarède. The Laniakea supercluster of galaxies. *Nature*, 513:71–73, September 2014. doi: 10.1038/nature13674.

K. Umetsu, T. Broadhurst, A. Zitrin, E. Medezinski, D. Coe, and M. Postman. A Precise Cluster Mass Profile Averaged from the Highest-quality Lensing Data. *Astrophysical Journal*, 738:41, September 2011. doi: 10.1088/0004-637X/738/1/41.

F. Vazza, E. Roediger, and M. Brüggen. Turbulence in the ICM from mergers, cool-core sloshing, and jets: results from a new multi-scale filtering approach. *Astronomy and Astrophysics*, 544:A103, August 2012. doi: 10.1051/0004-6361/201118688.

A. Vikhlinin, A. V. Kravtsov, R. A. Burenin, H. Ebeling, W. R. Forman, A. Hornstrup, C. Jones, S. S. Murray, D. Nagai, H. Quintana, and A. Voevodkin. Chandra Cluster Cosmology Project III: Cosmological Parameter Constraints. *Astrophysical Journal*, 692:1060–1074, February 2009. doi: 10.1088/0004-637X/692/2/1060.

Y.-Y. Zhang, N. Okabe, A. Finoguenov, G. P. Smith, R. Piffaretti, R. Valdarnini, A. Babul, A. E. Evrard, P. Mazzotta, A. J. R. Sanderson, and D. P. Marrone. LoCuSS: A Comparison of Cluster Mass Measurements from XMM-Newton and Subaru-Testing Deviation from Hydrostatic Equilibrium and Non-thermal Pressure Support. *Astrophysical Journal*, 711:1033–1043, March 2010. doi: 10.1088/0004-637X/711/2/1033.

Y.-Y. Zhang, H. Andernach, C. A. Caretta, T. H. Reiprich, H. Böhringer, E. Puchwein, D. Sijacki, and M. Girardi. HIFLUGCS: Galaxy cluster scaling relations between X-ray luminosity, gas mass, cluster radius, and velocity dispersion. *Astronomy and Astrophysics*, 526:A105, February 2011. doi: 10.1051/0004-6361/201015830.

F. Zwicky. On the Masses of Nebulae and of Clusters of Nebulae. *The Astrophysical Journal*, 86:217, October 1937. doi: 10.1086/143864.